Enabling Operational Flexibility of Power Generation Systems: Optimising and Controlling Turbine Casing Thermal Fields



Chukwuemeka Godwin Nwangele

Keble College

University of Oxford

A thesis submitted for the degree of

Doctor of Philosophy

Trinity 2025

Acknowledgements

Words cannot express my gratitude to Professor Budimir Rosic and the BR-Group and MHI for the support through my PhD. I am grateful to the Rhodes Trust for funding my studies at Oxford and providing me with the opportunity to grow and learn. Lastly, I would like to express my special gratitude to my family and loved ones for their unwavering support throughout this journey. I dedicate this work to my parents, Engr. Elias Nwangele and Mrs. Patricia Nwangele. They have paid forward immeasurable value and deserve every praise from me.

Abstract

A new design methodology is presented that transforms turbine components from static mechanical into active control system components to minimise thermal gradients and enable plant operational flexibility. Flexible power generation is crucial with the accelerated penetration of renewables. However, the associated rapid start-up, shut-down, and high ramp rates amplify thermal stresses and impact plant cyclic life. To control these stresses and preserve plant life, novel optimisation and plant control methods are required. However, turbine thermal and flow field complexities make this required optimisation computationally demanding and challenging to validate for industrial applications. This thesis proposes a new and realistic design philosophy for the multi-objective function of turbine cases to optimise and control thermal gradients and stresses. It demonstrates Reynolds-averaged Navier-Stokes conjugate heat transfer (RANS-CHT), thermal gradient models as objective functions, with controlled heat flux as variables, and utilising discrete turbine casing blocks to reduce thermal gradients by up to 70%. A hybrid control methodology comprising active control and thermal bridge passive components, to decrease the overall turbine thermal gradient by 80% is presented. Thermal gradient reduction smoothens turbine thermal profiles and minimises thermal stresses, allowing for more flexible operations. To validate these new solvers and optimisation methods, a novel turbine casing design facility is presented. The Oxford Turbine Casing Rig (OTCR) performs steady-state (part and full-load) and transient (cold/warm start-up and shut-down) regimes. It is also used to validate the novel active control methodology and numerical analysis, with an absolute difference of less than 5% between the measured and analytical values. Automated data transfer and reconstruction of fields with autoencoders for pre-computed optimisation and thermal field tuning are presented. Integrating novel optimisation methods, utilising turbine components as control systems, fast solvers, and validation tools, will advance turbine technologies and enable flexible operations. These advances are required to ultimately accelerate the penetration of clean energy and help achieve global decarbonisation targets, while ensuring energy security.

Contents

List of Figures **ix**

List of Tables **xvii**

Nomenclature **xix**

1 Introduction **1**
- 1.1 Background . . . 1
- 1.2 Contribution . . . 8
- 1.3 Thesis scope . . . 9
- 1.4 Thesis Outline . . . 10

2 Scientific Background and Methods **13**
- 2.1 Introduction . . . 13
- 2.2 Review of Flexible Operating Methodologies . . . 13
- 2.3 Computational Challenges of Flexible Operation . . . 17
- 2.4 New Methods and Limitations . . . 23
- 2.5 Validation Challenges . . . 25
- 2.6 Applied Flexibility Methods . . . 26
- 2.7 Requirements for Flexible Operations . . . 27
- 2.8 Summary . . . 29

3 Turbine Facility Design and Experimental Campaigns **31**
- 3.1 Introduction . . . 31
- 3.2 The OTCR . . . 33
- 3.3 OTCR Instrumentation . . . 42
  - 3.3.1 Fluid field measurements . . . 43
  - 3.3.2 Boundary condition setting . . . 46
- 3.4 Experimental campaign . . . 48
  - 3.4.1 Transient shutdown . . . 52
- 3.5 Uncertainties . . . 54
- 3.6 Summary . . . 55

4 Hybrid Steady-State and Transient Numerical Analysis and Physical Measurements 57
4.1 High-fidelity Numerical Analysis . . . 58
4.2 High-fidelity CHT results . . . 62
4.2.1 Fluid domain contours . . . 62
4.2.2 Solid domain temperature field . . . 64
4.2.3 Result Validation . . . 65
4.2.4 Fluid cavity temperature validation . . . 67
4.2.5 Post shut-down natural cooling . . . 70
4.3 Novel Numerical Tools for Thermal Field Analysis and Optimisation 75
4.3.1 TNM setup . . . 75
4.4 Steady-State Results . . . 82
4.5 Summary . . . 89

5 Active and Passive Thermal Gradient Optimisation 91
5.1 Thermal Gradients Overview . . . 91
5.1.1 Active Control Methods . . . 94
5.1.2 Optimisation Problem . . . 98
5.1.3 Optimisation Results . . . 103
5.1.4 Experimental Validation of Active Control Optimisation Methods . . . 110
5.1.5 Validation Experimental Campaign . . . 112
5.1.6 Active Control Experiment Results . . . 115
5.1.7 Hybrid Active and Passive Methodology . . . 116
5.1.8 Hybrid Optimisation Results . . . 120
5.1.9 Operationalising Optimisation and Control Strategies . . . 122
5.2 Summary . . . 128

6 Conclusion and Outlook 129
6.1 Outlook . . . 132
6.2 Publications . . . 135

References 137

List of Figures

1.1 Evolution of the global electricity generation mix from renewables, from 1985 (top) to 2024 (bottom), showing the rising share of intermittent sources relative to fossil fuels. The colour scale indicates the percentage of clean energy penetration in each country [1]. . . . 2
1.2 Projected global share of solar and wind energy in the electricity mix up to 2050 under current trajectory and net-zero scenarios [5]. . . . 3
1.3 Schematic of grid supply-demand balance for (a) a non-flexible system with fixed baseload and intermittent renewables showing curtailment and shortfall, and (b) a flexible system capable of compensating renewable intermittency. . . . 4
1.4 Steam turbine cross-section showing (a) critical structural components, including the HP, IP, and LP turbines, with components such as the casing, steam inlet, and generator coupling. (b) The steady-state characteristic temperature field distribution on the turbine casing during operation, highlighting non-uniform thermal distribution and regions of high thermal gradient [11]. . . . 5
1.5 The required shift in operational philosophy of power generation turbines from conventional operation to demanding flexible operations. 6
1.6 The evolution of the internal cavity flow regime through turbine operational states, from forced convection dominant during full-load, transitioning to mixed and natural convection during shutdown, driving complex thermal fields. . . . 7
1.7 Schematic of casing deformation modes, including (a) transverse deformation caused by differential expansion between thick flanges and thin barrel sections, and (b) upward bowing (cat's back effect) caused by higher temperatures at the top of the casing. . . . 8

2.1 Turbine operating envelope showing temperature and speed conditions for cold, warm, and hot start regimes relative to the design efficiency point, based on industrial data [12]. . . . 14
2.2 Conjugate heat transfer (CHT) computational domain for an intermediate pressure steam turbine, with refined mesh at seal and geometric hotspot regions [11]. . . . 18

2.3 Steady-state conjugate thermal fields showing solid and fluid domain temperature distribution and heat transfer for an intermediate-pressure steam turbine casing [11]. 19
2.4 2D finite element discretisation of the turbine inner casing into nodal grid elements used for transient thermal field prediction [32]. 20
2.5 Effect of timestep size on transient natural cooling temperature prediction from a loosely coupled CHT model, demonstrating the trade-off between computational cost and temporal accuracy [29]. . 23
2.6 Sparse thermocouple instrumentation on the outer casing of an industrial steam turbine, illustrating the limitations of current physical validation data for conjugate thermal models [11]. 26
2.7 Electric Trace Heating System (THS) applied to a Siemens Energy steam turbine casing for hot standby mode: (A) THS elements on outer casing; (B) THS cement application; (C) casing insulation [61]. 27
2.8 Proposed framework for real-time thermal optimisation and control of power-generating turbines, integrating live plant measurements, high-fidelity numerical analysis, active and passive control, and field reconstruction tools. 28

3.1 A photograph of the Oxford Turbine Casing Rig installed at the Oxford Thermofluids Institute, showing the outer casing, inlet ducting, and instrumentation connections. 32
3.2 The design layout and picture of the OTCR indicating the industrial fan, heater, turbine casing test section, inlet and outlet flow paths, and traverse instrumentation. 35
3.3 OTCR design and comparison with an industrial steam turbine. . . 36
3.4 Normalised steady-state temperature fields on the OTCR casing for inlet temperatures ranging from 300 K to 900 K, demonstrating qualitative similarity across the range that validates the use of scaled experimental temperatures for comparison with industrial conditions. 38
3.5 Annular cavity geometry of the OTCR showing the key dimensions used to compute the Grashof (Gr), Reynolds (Re), and Richardson (Ri) numbers. 40
3.6 OTCR operating envelope in Re-Ri space, showing the range of cavity flow regimes comprising natural, mixed, and forced convection, typical turbine operating range (light red) and MHI target operating range (dark red). 41
3.7 Thermocouple distribution on the OTCR outer casing (51 Type-K sensors, planes A-I) and inner casing (33 sensors, planes Ai-Ei), positioned to capture thermal field gradients at design-critical locations. 44

3.8 Schematic of the automated traverse assembly, showing the stepper motor, driver, needle guide, and thermocouple/hot-wire sensor tip, capable of radial cavity measurements. 45
3.9 Axial and circumferential placement of the four fluid measurement traverses (Tr1-Tr4) within the OTCR cavity. Coordinates are detailed in Table 3.7. 46
3.10 Normalised radial velocity profiles (u/u_c) across the OTCR shaft inlet for three mass flow rates ($\dot{m} = 0.19$, 0.23, 0.26 kg/s), showing uniform inlet conditions across the operating range. Radial resolution is 1 mm near the wall, 5 mm in the intermediate region, and 10 mm at the centreline. 47
3.11 Differential pressure versus mass flow rate calibration curve for the OTCR shaft inlet, enabling interpolation of $\dot{m}$ across the full operating range. 48
3.12 Experimental boundary conditions for the steady-state full-load campaign with counter-crossflow inlet at $\dot{m} = 0.2$ kg/s and $T = 453$ K, ambient outer wall condition ($T = 298$ K, $h = 10$ W m^{-2} K^{-1}). . . . 50
3.13 Three-hour temperature histories for representative outer and inner casing thermocouples during start-up and approach to steady state ($\dot{m} = 0.2$ kg/s, $T = 453$ K). 51
3.14 Normalised temperature comparison between instrumented and mirror-position thermocouples on the outer casing, illustrating equivalent thermal measurements. 51
3.15 Shutdown experimental setup conditions indicating the boundary conditions and experimental configuration for the transient natural shutdown regime. 53
3.16 Three-hour temperature decay histories for representative outer and inner casing thermocouples during transient natural cooling post-shutdown, initiated from steady-state full-load conditions. 54

4.1 Symmetry-plane view of the multi-domain CHT mesh comprising solid domains (outer casing, inner casing, shaft) and fluid domains (hot and cold), with inflation layers at solid-fluid interfaces. 59
4.2 Boundary conditions applied to the CHT numerical model, comprising the hot and cold inlets and ambient conditions for the OTCR. . 61
4.3 Steady-state fluid velocity contours with three axial cross-sections of the OTCR cavity, revealing forced convection in the main flow path and recirculating mixed-convection flows in the annular cavity that drive non-uniform casing heat transfer. 62

4.4 Steady-state fluid temperature contours at three axial cross-sections, showing the influence of cavity recirculation on the local fluid temperature field and its coupling to the casing solid domain. 63
4.5 Steady-state temperature contours of the OTCR outer casing at full-load conditions ($\dot{m}$ = 0.2 kg/s, T_{in} = 453 K, T_{∞} = 298 K), highlighting high thermal gradient regions at the inlet interface and thick-walled flange sections. 65
4.6 Steady-state temperature contours of the OTCR inner casing under full-load conditions ($\dot{m} = 0.2$ kg/s, $T_{in} = 453$ K, $T_{\infty} = 298$ K). The casing shows a higher temperature gradient along the inlet region and a near-uniform temperature distribution in the thin-walled barrel region due to the absence of a bladed path. 66
4.7 Polar plots of normalised outer casing temperature $T^* = T/T_{\max}$ at planes A–D, comparing CHT predictions with thermocouple measurements at steady-state full-load conditions ($\dot{m}$ = 0.2 kg/s, $T_{in} = 453$ K, $T_{\infty} = 298$ K) 68
4.8 Polar plots of normalised outer casing temperature $T^* = T/T_{\max}$ at planes E–I, comparing CHT predictions with thermocouple measurements at steady-state full-load conditions ($\dot{m} = 0.2$ kg/s, $T_{in} = 453$ K, $T_{\infty} = 298$ K). 69
4.9 Polar plots of normalised inner casing temperature $T^* = T/T_{\max}$ at planes A_i–E_i, comparing CHT predictions with thermocouple measurements at steady-state full-load conditions ($\dot{m}$ = 0.2 kg/s, $T_{in} = 453$ K, $T_{\infty} = 298$ K). 72
4.10 Normalised traverse fluid temperature profiles $T^* = T/T_{\max}$ at four cavity locations (Tr1–Tr4), comparing CHT predictions with thermocouple measurements at steady-state full-load conditions ($\dot{m}$ = 0.2 kg/s, T_{in} = 453 K, T_{∞} = 298 K, revealing the near-wall thermal boundary layer structure and mixed-convection cavity behaviour. 73
4.11 Post-shutdown natural cooling showing transient temperature decay at thermocouples T3, T16, and T29, comparing CHT predictions with physical measurements. Initial condition: steady-state full-load ($\dot{m} = 0.2$ kg/s, $T_{in} = 453$ K). Shutdown condition: zero mass flow ($\dot{m}$ = 0 kg/s), T_{∞} = 298 K, Temperature field contours shown at t = 20, 40, and 60 min. 74
4.12 Thermal Network Model (TNM) electrical analogy showing the 1D equivalent circuit with conductive (Rc), convective (Rv), and advective (Ra) resistances and nodal capacitances. It further demonstrates the lump-mass blocking strategy, reducing the number of mesh cells to analysis blocks for multi-zone analysis. 76

4.13 Comparison of high-fidelity CHT mesh (2.6×10^6 elements, with inflation layers) and low-fidelity TNM mesh (1.5×10^6 elements, no inflation layers), illustrating the 75% reduction in node density that enables rapid thermal field resolution. 77
4.14 Boundary condition setting for the TNM equivalent to the CHT, alongside spatially varying heat transfer coefficient derived directly from the converged CHT solution. The heat transfer coefficient reaches up to $h_{\max} = 40\ \mathrm{W\,m^{-2}\,K^{-1}}$ and is shown normalised as $h^* = h/h_{\max}$ to illustrate the spatial variation across the casing surface. 79
4.15 The process flowchart for the hybrid fidelity transient shutdown simulation comprises CHT fields, which initialises the TNM at each 10-minute timestep, and the TNM resolves the thermal field for that interval. The output becomes the initial condition for the next step, and this continues for the full shutdown duration. 81
4.16 The steady-state outer casing temperature field predicted by the TNM numerical model exhibits higher thermal gradients at the inlet flange and in the thick-walled regions. 82
4.17 Polar plots of normalised outer casing temperature $T^* = T/T_{\max}$ at planes A–D, comparing CHT, TNM, and experimental measurements at full load steady-state conditions ($\dot{m} = 0.2$ kg/s, $T_{in} = 453$ K, $T_\infty = 298$ K.) 85
4.18 Polar plots of normalised outer casing temperature $T^* = T/T_{\max}$ at planes E–I, comparing CHT, TNM, and experimental measurements at steady-state full-load conditions ($\dot{m} = 0.2$ kg/s, $T_{in} = 453$ K, $T_\infty = 298$ K.) 86
4.19 Polar plots of normalised inner casing temperature $T^* = T/T_{\max}$ at planes $\mathrm{A_i}$–$\mathrm{E_i}$, comparing CHT, TNM, and experimental measurements at steady-state full-load conditions ($\dot{m} = 0.2\,\mathrm{kg/s}$, $T_{in} = 453$ K, $T_\infty = 298$ K.) 87
4.20 Post-shutdown transient natural cooling at thermocouples T4, T16, and T29, comparing CHT, TNM predictions, and physical measurements. Steady-state full-load- ($\dot{m} = 0.2$ kg/s, $T_{in} = 453$ K). Shutdown condition- ($\dot{m} = 0$ kg/s), $T_\infty = 298$ K. 88

5.1 Steady-state thermal gradients on the OTCR casing, indicating corresponding thermal gradient distribution [$\mathrm{K\,m^{-1}}$] and potential regions of higher thermal stress, especially in geometrically non-uniform and complex flow regions. 93

5.2 Discretisation of the OTCR casing into 27 independent thermal blocks, with heater pad locations identified for active boundary condition control. Red patches indicate the zones selected for active heat flux optimisation (zones 6, 7, 11, 15, 19, 20, 21, 23, and 24), corresponding to regions of highest thermal gradient identified from the preliminary CHT analysis. 96
5.3 The spatio-temporal active control optimisation framework, which comprises the steady-state optimal heat flux, initialises the transient loop. At each 10-minute timestep, the optimiser determines the flux distribution to minimise the thermal gradient across all blocks, and the output field seeds the next timestep. 97
5.4 The block-wise Bayesian optimisation prioritises zones with a critical thermal gradient. A parametric heat flux is varied in steps via PyFluent automation, and the global optimum flux distribution is selected and applied. 99
5.5 Time evolving temperatures for optimised and unoptimised cases showing a warmer casing through the entire cooling history of the optimised case, compared to the unoptimised case. 104
5.6 Transient thermal gradients for optimised and unoptimised cases showing the impact of actively controlled heat fluxes on the solid metal body. 105
5.7 Surface projection of steady-state thermal gradient on the OTCR casing showing the unoptimised baseline comprising high thermal gradients at inlet, outlet, and end plate regions. The actively optimised case shows redistribution and reduction of peak thermal gradients in optimised zones. 107
5.8 Graphs of the optimised transient thermal active thermal gradient in the optimised OTCR field plotted on the same axes as the steady-state unoptimised field. 108
5.9 Localised increase in thermal gradient in response to external heat flux in specific zones, including zones 21 and 23. These zones illustrate the need for enhanced treatment of thermal gradients in some localised zones. 109
5.10 A photograph of the OTCR modified for active control validation, showing flexible silicone resistive heater pads installed on zones 6, 7, 11, 15, 19, 20, 21, 23, and 24, conforming to casing geometry, including flanges and fillets. 111
5.11 Validation experiment for transient shutdown thermal gradient optimisation framework showing the control of heat flux per the analytical optimisation solution. 113

5.12 Polar plots of normalised casing temperature at planes C, D, and G comparing physical measurements and numerical predictions for the unoptimised and actively optimised cases. 116
5.13 Thermal resistance network for the passive copper bridge methodology, with an electrical circuit analogy showing the reduced effective resistance of the steel-copper composite at end plate regions, where copper reduces the thermal gradient relative to steel alone. 117
5.14 Hybrid active–passive control configuration showing the heater pad zones (red patches) and the copper thermal bridge placement (brown regions) on the end plate regions of the OTCR casing. Copper bridges are added exclusively at the end plate locations shown, and no copper is applied elsewhere on the casing. 8 mm copper shell thickness is used, determined from the passive optimisation. 118
5.15 Thermal gradient magnitude $|\nabla T|$ of the OTCR end-plates as a function of copper shell thickness t_c, showing diminishing returns with increasing thickness. 120
5.16 Optimal temperature field resulting from hybrid active and passive control methodologies 121
5.17 Optimal thermal gradient resulting from hybrid active and passive control methodologies reflecting a reduction in thermal gradient in most casing regions for the hybrid control method. 124
5.18 Zone-wise thermal gradient reduction achieved by the hybrid active-passive optimisation relative to the unoptimised baseline and active-only case. Hybrid optimisation achieves an overall reduction of up to 80%. 125
5.19 The proposed real-time plant thermal optimisation and control framework, integrating pre-computed high-fidelity CHT solutions, live sensor measurements, TNM fast solver, field reconstruction via autoencoder, and active/passive control outputs for thermal gradient and stress management. 126
5.20 Sensor placement strategy for thermal field reconstruction from 51 thermocouple locations on the OTCR outer casing mapped into the latent space of the autoencoder for full-field temperature reconstruction and real-time input to the turbine field optimisation and control. 127
5.21 A comparison of the autoencoder-reconstructed temperature field from 51 thermocouple sensor inputs and the high-fidelity CHT reference field, demonstrating the applicability of the data-driven field reconstruction method for real-time control applications. . . . 127

List of Tables

1.1 A review of investigated renewable intermittency mitigation strategies. 3
1.2 Comparison of operational philosophy between conventional and flexible power generation systems. 6

3.1 Dimensional Parameters of the OTCR Turbine Casing 34
3.2 Casing material Properties 37
3.3 OTCR operating range 39
3.4 OTCR Experimental Capabilities 41
3.5 Planar distribution of thermocouples on the OTCR outer casing . . 43
3.6 Planar distribution of thermocouples on the OTCR inner casing . . 43
3.7 Traverse fluid temperature measurements locations 46
3.8 Experimental Test Conditions 50
3.9 Experimental Test Conditions 52
3.10 Experimental Uncertainties 55

4.1 Numerical analysis solid material Properties 61
4.2 Numerical analysis fluid Properties [66] 61
4.3 Overview of Outer Case Temperature Measurements: Percentage Difference Between CHT Simulation and Experimental Results is calculated as [CHT − Experiment] [%], averaged across all circumferential thermocouple positions within each plane. 66
4.4 Overview of Inner Case Temperature Measurements: Percentage Difference Between CHT Simulation and Experimental Results is calculated as [CHT − Experiment] [%], averaged across all circumferential thermocouple positions within each plane. 67
4.5 Traverse fluid temperature measurements: percentage difference between CHT predictions and experimental traverse thermocouple measurements, calculated as [CHT − Experiment] [%] [84]. 70
4.6 Average percentage difference between numerical predictions (CHT and TNM) and experimental thermocouple measurements for each axial plane of the outer casing, calculated as [Numerical−Experiment] [%] and averaged across all circumferential thermocouple positions within each plane [84]. 83

4.7 Average percentage difference between numerical predictions (CHT and TNM) and experimental thermocouple measurements for each axial plane of the inner casing, calculated as [Numerical−Experiment] [%] and averaged across all circumferential thermocouple positions within each plane [84]. 84

5.1 Optimised heat flux requirements [$\mathrm{W\,m^{-2}}$] for active thermal gradient control of the OTCR at each timestep during transient shutdown ($\dot{m} = 0$ kg/s, $T_\infty = 298$ K, $\Delta t = 10$ min, initial condition: steady-state full-load at $\dot{m} = 0.2$ kg/s, $T_{in} = 453$ K). 102

5.2 Heater pad power input for all heating zones during the active control validation test campaign 114

Nomenclature

A	Face area [m^2]
α	Thermal diffusivity [$\mathrm{m}^2\,\mathrm{s}^{-1}$]
β	Thermal expansion coefficient [K^{-1}]
Bi	Biot number [–]
C	Capacitance matrix [$\mathrm{J}\,\mathrm{K}^{-1}$]
C_f	Skin friction coefficient [–]
C_p	Specific heat capacity [$\mathrm{J}\,\mathrm{kg}^{-1}\,\mathrm{K}^{-1}$]
d	Distance between node centres [m]
D_h	Hydraulic diameter [m]
D_2	Hydraulic diameter of fluid domain [m]
ΔT	Temperature difference [K]
Δt	Time step [s]
Δy	First layer height [m]
$\mathrm{erfc}(\cdot)$	Complementary error function [–]
E	Total energy [$\mathrm{J}\,\mathrm{kg}^{-1}$]
Fo	Fourier number [–]
g	Gravitational acceleration [$\mathrm{m}\,\mathrm{s}^{-2}$]
Gr	Grashof number [–]
h	Specific enthalpy [$\mathrm{J}\,\mathrm{kg}^{-1}$]
h_1	Heat transfer coefficient [$\mathrm{W}\,\mathrm{m}^{-2}\,\mathrm{K}^{-1}$]
h_2	Heat transfer coefficient of fluid domain [$\mathrm{W}\,\mathrm{m}^{-2}\,\mathrm{K}^{-1}$]
h_{2t}	Time-dependent heat transfer coefficient [$\mathrm{W}\,\mathrm{m}^{-2}\,\mathrm{K}^{-1}$]
$\vec{J}$	Diffusion flux vector [$\mathrm{kg}\,\mathrm{m}^{-2}\,\mathrm{s}^{-1}$]
J	Objective function (mean thermal gradient magnitude) [$\mathrm{K}\,\mathrm{m}^{-1}$]
k	Thermal conductivity [$\mathrm{W}\,\mathrm{m}^{-1}\,\mathrm{K}^{-1}$]
k_{air}	Thermal conductivity of air [$\mathrm{W}\,\mathrm{m}^{-1}\,\mathrm{K}^{-1}$]
$K(T)$	Over-conductivity correction factor, $K(T) > 1$ [–]
L	Length / characteristic length [m]
L_g	Gap width [m]
$\dot{m}$	Mass flow rate [$\mathrm{kg}\,\mathrm{s}^{-1}$]
μ	Dynamic viscosity [$\mathrm{kg}\,\mathrm{m}^{-1}\,\mathrm{s}^{-1}$]
Nu	Nusselt number [–]
ν	Kinematic viscosity [$\mathrm{m}^2\,\mathrm{s}^{-1}$]
p	Pressure [Pa]
Pr	Prandtl number [–]
Pr_2	Prandtl number in fluid domain [–]
q	Heat flux [$\mathrm{W}\,\mathrm{m}^{-2}$]

$\dot{q}_{OC}$	Overall heat flux at outer casing [$\mathrm{W\,m^{-2}}$]
$\dot{q}_{rad}$	Radiative heat flux [$\mathrm{W\,m^{-2}}$]
$\dot{q}_{nat.conv}$	Natural convection heat flux [$\mathrm{W\,m^{-2}}$]
$\dot{q}_{forc.conv}$	Forced convection heat flux [$\mathrm{W\,m^{-2}}$]
q_0	Constant surface heat flux [$\mathrm{W\,m^{-2}}$]
r	Radial coordinate [m]
r_0	Radial coordinate origin [m]
R_a	Advective resistance [$\mathrm{K\,W^{-1}}$]
R_c	Conductive resistance [$\mathrm{K\,W^{-1}}$]
R_v	Convective resistance [$\mathrm{K\,W^{-1}}$]
Re	Reynolds number [–]
Re_2	Reynolds number in fluid domain [–]
Ri	Richardson number [–]
ρ	Density [$\mathrm{kg\,m^{-3}}$]
S	Contact surface area between adjoining nodes [$\mathrm{m^2}$]
σ	Thermal stress [Pa]
T	Temperature [K]
$T_{i,j}$	Temperature at node (i, j) [K]
$T'_{i,j}$	Updated temperature at node (i, j) [K]
T_i	Initial or inner casing temperature [K]
T_o	Outer casing temperature [K]
T^*	Normalised temperature, $T^* = T/T_{\max}$ ($T_{\max} = 453\,\mathrm{K}$) [–]
T_2	Fluid domain bulk temperature [K]
T_{2t}	Time-dependent bulk temperature [K]
τ_w	Wall shear stress [$\mathrm{N\,m^{-2}}$]
$\bar{\bar{\tau}}_{eff}$	Effective stress tensor [$\mathrm{N\,m^{-2}}$]
t	Copper thickness (design variable) [m]
t	Time [s]
t_c	Copper thickness (design variable) [m]
$t_{c,i}$	Copper thickness for zone i [m]
u	Local velocity [$\mathrm{m\,s^{-1}}$]
$V_{i,j}$	Control volume associated with node (i, j) [$\mathrm{m^3}$]
$V_{\max}$	Maximum velocity, $35\,\mathrm{m\,s^{-1}}$ [$\mathrm{m\,s^{-1}}$]
$\vec{v}$	Velocity vector [$\mathrm{m\,s^{-1}}$]
v^*	Normalised velocity, $v^* = v/V_{\max}$ [–]
v_∞	Free-stream velocity [$\mathrm{m\,s^{-1}}$]
v_τ	Friction velocity [$\mathrm{m\,s^{-1}}$]
ξ	Depth coordinate normal to heated surface [m]
ξ_s	Position vector at boundary surface [m]
y	Wall distance [m]
y^+	Dimensionless wall distance [–]
$\lvert\nabla T\rvert$	Temperature gradient magnitude [$\mathrm{K\,m^{-1}}$]
∇^2	Laplacian operator [$\mathrm{m^{-2}}$]

1 Introduction

1.1 Background

This thesis develops methodologies for transforming the design and operational philosophy of power-generating turbines to enable operational flexibility in an intermittent renewables-dominant and complex global energy system. Figure 1.1 indicates the rapid evolution of power systems over the past four decades from a fossil-dominant system to a new energy landscape comprising numerous low-carbon sources, such as solar, wind, wave, and tidal energy [1]. Between 2020 and 2050, global commitments to mitigate climate change are driving further rapid adoption of intermittent renewable energy sources. Between 2025 and 2027, global electricity demand was projected to surge by up to 4% annually, met in part by intermittent solar energy [2]. To amplify the concern, the recent drive to develop artificial intelligence (AI) and the demand from data centres with specialised graphical processing units (GPUs) as well as cooling consume over 415 TWh/annum (1.5% of global electricity consumption) and are projected to grow 15% year-on-year to 2030 [3]. Intermittent renewables are projected to meet 50% of these additional electricity demand requirements [3]. Up to 67% and 97% of energy and electricity supply must be renewable, with solar and wind accounting for almost 80% of the

electricity mix for a 2050 net-zero target to limit global warming to sub-1.5^{0}C [4, 5] as shown in Figure 1.2.

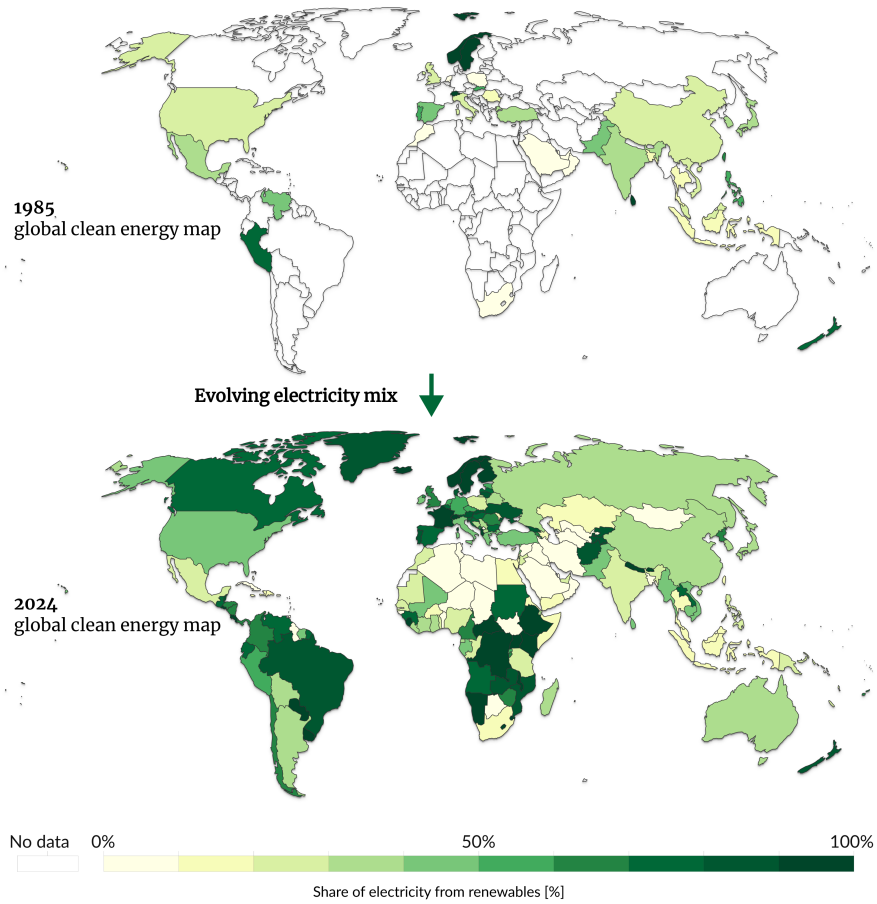
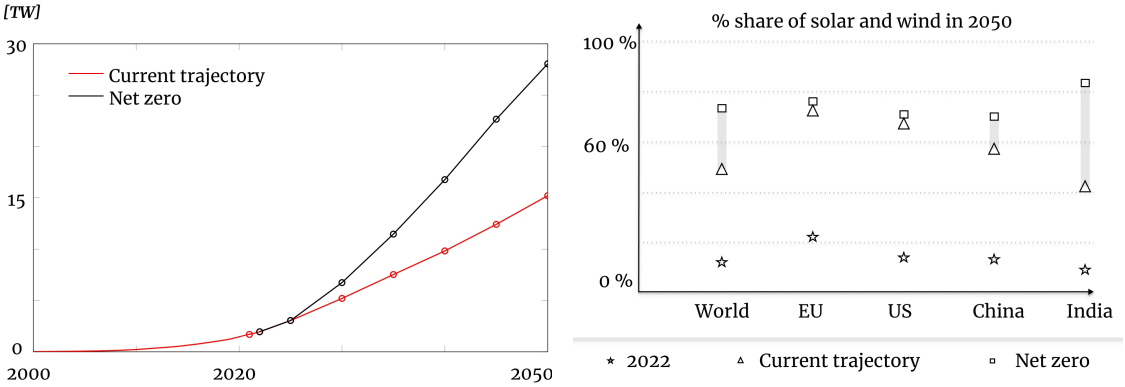


Figure 1.1: Evolution of the global electricity generation mix from renewables, from 1985 (top) to 2024 (bottom), showing the rising share of intermittent sources relative to fossil fuels. The colour scale indicates the percentage of clean energy penetration in each country [1].

Renewable energy sources are characterised by intermittency, including fluctuations with diurnal cycles, cloud cover, and seasonal variations associated with solar photovoltaic (PV) systems and wind speed-driven variations of wind turbines, leading to variability in output [6]. As illustrated in Figure 1.3 A, coupling intermittent sources with fluctuating demand causes net power imbalances, unsuitable for stable frequency grid networks. With a constant baseload generation, excess intermittent renewable potential is curtailed [7]. Conversely, demand could be unmet in adverse weather conditions, given the inherent weather variability of these sources.



(a) The global projected rapid growth trajectory of solar and wind energy up to 2050.

(b) The global and country specific projected share of wind and solar in the global electricity mix by 2050.

Figure 1.2: Projected global share of solar and wind energy in the electricity mix up to 2050 under current trajectory and net-zero scenarios [5].

Table 1.1: A review of investigated renewable intermittency mitigation strategies.

Description	Advantage	Disadvantage
Use battery energy storage	Fast response dispatchable power	Expensive, technical limits, scarcity of rare earth materials
Pumped hydroelectric storage	Mature technology, large-scale dispatchable power	Geographically constrained by topography and water availability
Hydrogen and ammonia energy vectors	High energy density, long-duration storage	High cost, low round-trip efficiency
Complementary renewable energy systems	Complementarity of solar and wind.	Adverse weather events cause extreme risks
Demand response management	Balances supply and demand	Difficulty to control stochastic demand/supply
Dispatchable generators	Fast supply response	Extreme operational conditions
Flexible conventional power generation	Existing infrastructure, reliable dispatchable power	Thermal stress limits ramp rates and start-up frequency

Table 1.1 shows some previously proposed approaches to mitigate the challenges of renewable intermittency and guarantee energy security [8]. While batteries can provide dispatchable power, they are costly and pose geopolitical challenges due to the scarcity of the materials necessary for their production. By definition, dispatchable power systems can handle the variability and uncertainty in intermittent renewable energy generation, regardless of prevailing weather conditions, across all relevant sources of variability (supply and demand) and timescales. Alternative energy storage and dispatchable renewables, such as pumped hydroelectric storage,

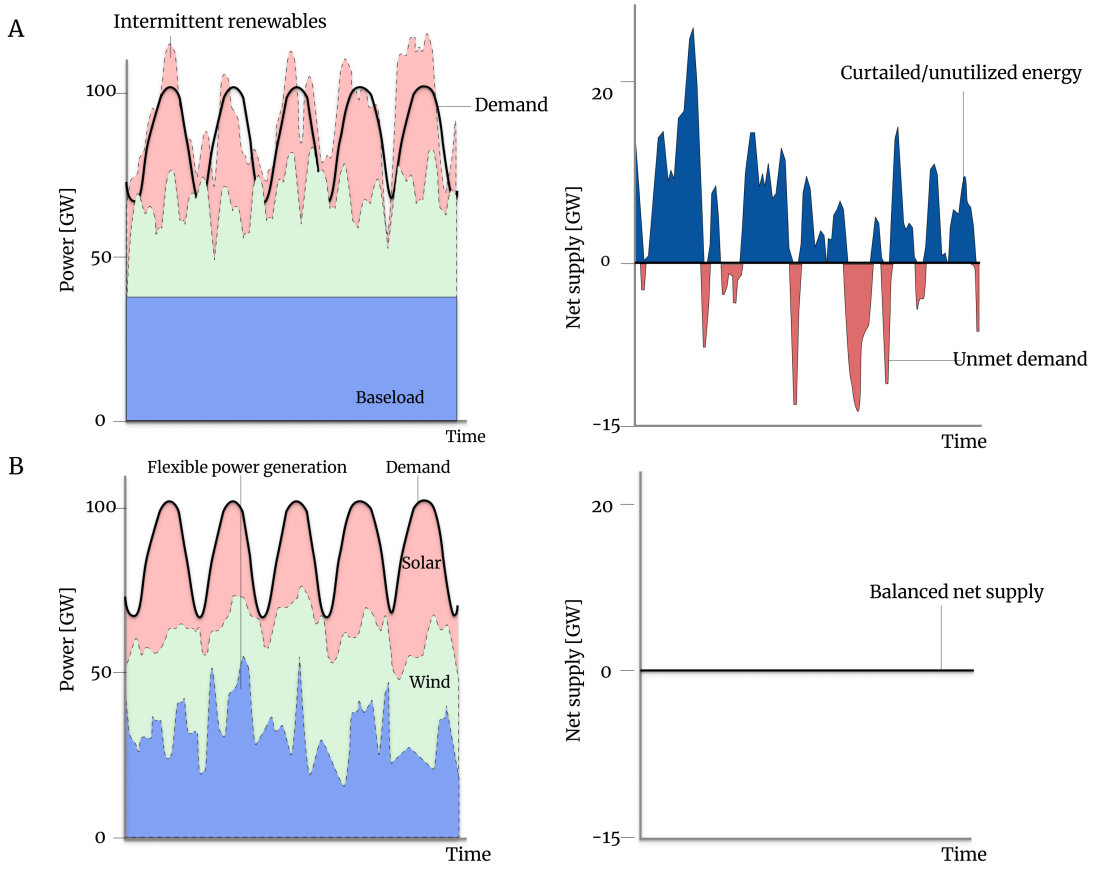


Figure 1.3: Schematic of grid supply-demand balance for (a) a non-flexible system with fixed baseload and intermittent renewables showing curtailment and shortfall, and (b) a flexible system capable of compensating renewable intermittency.

which uses gravitational potential energy for on-demand power, and chemical energy vectors such as green hydrogen and ammonia, which store surplus renewable energy in chemical form for later combustion, have also been proposed [9, 10]. However, pumped storage is limited by suitable topography and water resources. Ammonia-to-power technology is at an early stage and is only projected to be cost-competitive by 2040, contingent on reduced electrolyser costs [9]. Other mitigating strategies, such as complementary renewable energy sources, are stochastic and vulnerable to adverse environmental incidents. Demand-side response is limited in conditions of extreme supply shortages, as earlier highlighted. It also depends on social and political will, which is more challenging to predict. Consequently, the intermittent characteristics of renewables necessitate fast, flexible grid balancing systems to effectively manage energy supply and demand fluctuations.

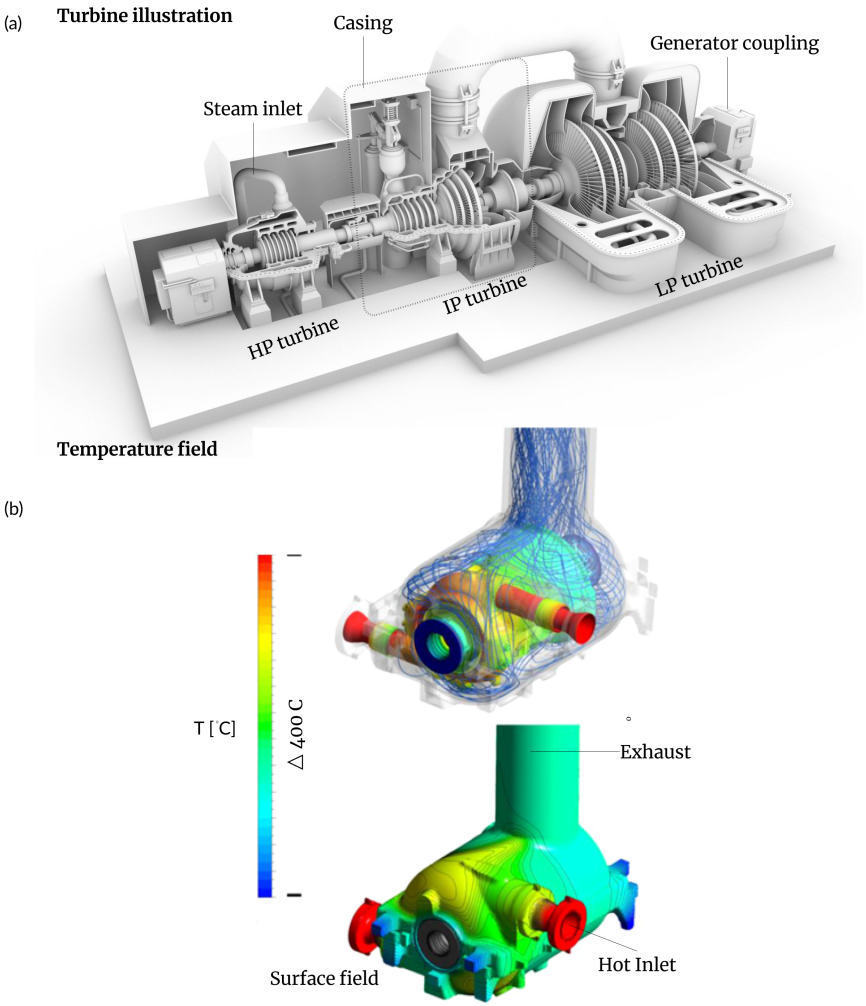


Figure 1.4: Steam turbine cross-section showing (a) critical structural components, including the HP, IP, and LP turbines, with components such as the casing, steam inlet, and generator coupling. (b) The steady-state characteristic temperature field distribution on the turbine casing during operation, highlighting non-uniform thermal distribution and regions of high thermal gradient [11].

In contrast, an alternative source of dispatchable power for flexible operations is conventional power generation systems, such as steam and gas turbines, illustrated in Figure 1.4, which account for 65% of the electricity generation in 2024 [1] and are well understood. These plants are designed to operate under steady-state conditions with high temperatures and pressures to achieve high operational efficiency [12]. These design objectives require the use of thick casings [up to 150 mm] with complex geometric solid- and fluid-flow regimes[13, 14]. Figure 1.4 also shows the resulting temperature field contours of these typical turbines during their operations, with

Table 1.2: Comparison of operational philosophy between conventional and flexible power generation systems.

	Conventional power generation	Flexible power generation
1	Dominated by fuels and baseload plants	Intermittent renewable dominant
2	Gradual load cycle	Rapid load cycle
3	Narrow operating window	Wide operating window
4	Steady-state operations	Rapid transients
5	Peak efficiency	Broad efficiency

defined thermal field gradients [11]. A high thermal gradient is a constraint on the adoption of steam and gas turbines for flexible operations.

Neglecting the thermal gradient constraint and making these plants flexible for dispatchable power to balance the stochastic supply of renewable energy requires a change in operational requirements, as shown in Figure 1.5 and detailed in Table 1.2 [15]. This new operating mode, characterised by severe events (rapid load ramps, cold startups, and trips), generates high cyclic thermal fields and intensifies the thermal stresses on turbine components to unacceptable levels, thereby impacting plant design life [16].

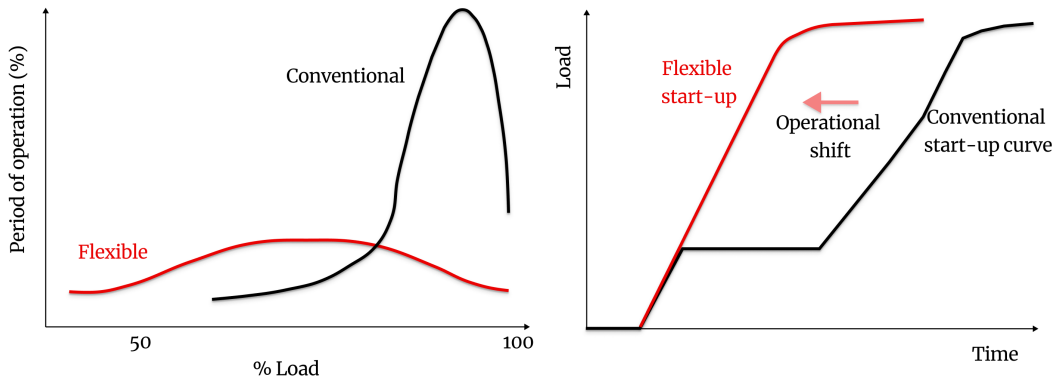


Figure 1.5: The required shift in operational philosophy of power generation turbines from conventional operation to demanding flexible operations.

Aside from the extreme operating conditions, the power-generating turbines' characteristic intricate and complex fluid domain physics, especially in the cavity regions, as shown in Figure 1.6, significantly influence turbine thermal fields [17, 18]. The complexity of the flow fields ranges from steady-state, full- and part-load with

forced convection-dominant flows to mixed cavity flows from transient shutdown operations due to vacuum steam injection through the gland seals. Flow regimes transition to natural convection-dominant when the vacuum is broken. This complex heating from steam, combined with the steam-metal temperature differential in various operating regimes, causes deformations in different turbine planes, resulting in high stresses in areas of geometric variances [19].

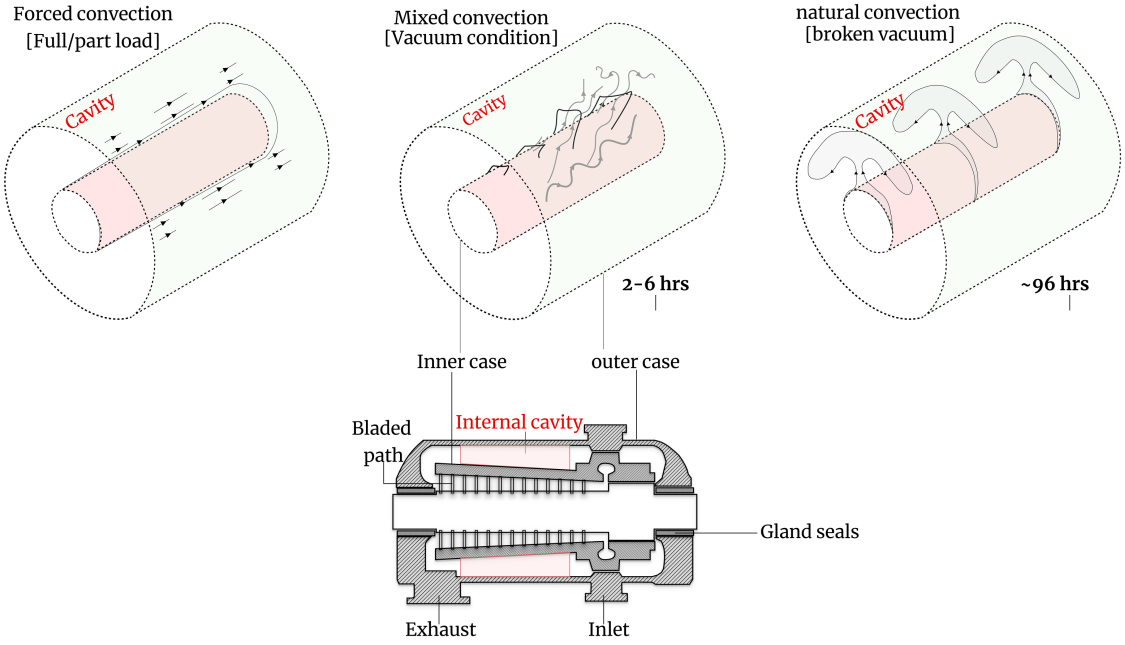


Figure 1.6: The evolution of the internal cavity flow regime through turbine operational states, from forced convection dominant during full-load, transitioning to mixed and natural convection during shutdown, driving complex thermal fields.

The differential expansion between thinner casing surfaces and thicker flanges causes transverse deformations, whereas the condensation effect and fluid flow result in higher temperatures at the top of the casing, causing an upward bowing known as the cat's back effect. These transverse deformations and the cat's back effect illustrated in Figure 1.7, driven by fluid-solid interactions, reduce rotor-casing clearances, impacting turbine efficiency and reliability, inhibiting their ability to operate flexibly. High thermal gradients in the turbine casing cause mechanical stress through differential and constrained expansion between hotter regions and cooler zones. Expansion is constrained by the casing's continuous

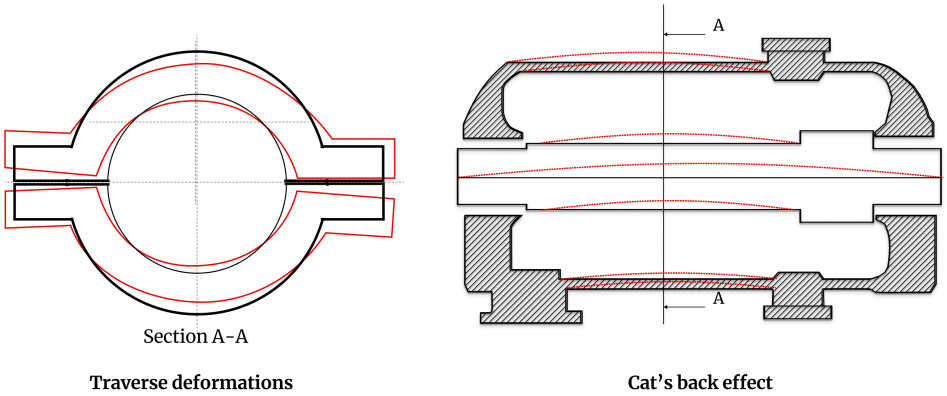


Figure 1.7: Schematic of casing deformation modes, including (a) transverse deformation caused by differential expansion between thick flanges and thin barrel sections, and (b) upward bowing (cat's back effect) caused by higher temperatures at the top of the casing.

structure, especially at thick flanges and split faces, resulting in internal compressive and tensile stresses that scale with the temperature difference. These stresses intensify during rapid transients. With these complex and evolving fluid fields and the impact of cyclic operations on the solid domain, the philosophy of designing a turbine components should be changed beyond treating the solid domain as a mere structural component that can withstand high temperature and pressure. The solid and fluid cavity domains should instead become active components for optimisation and control, enabling flexible operation. However, the fluid regime in these cavity regions suffer from unvalidated black-box fluid physics, causing significant numerical analysis challenges. The limited understanding of these challenging flow fields must be addressed for flexible operation to become a reality. Understanding and resolving these limitations unlocks the potential for flexible power generation and the unhindered penetration of clean energy, achieving the twin goals of mitigating global warming and ensuring energy security.

1.2 Contribution

This thesis explores methods to transform the design and operational philosophy of solid domain components from mere structural features to active optimisation and control enablers for flexible operation of power-generating systems. It develops novel optimisation and control methodologies to enhance the operational flexibility

of power-generating systems, enabling operation in an energy system dominated by intermittent renewable sources. It presents methodologies and validation techniques to understand complex fluid physics and solid domain thermal fields. New numerical analysis tools and fast solvers are utilised. Active and passive control methodologies for optimising turbine thermal fields are introduced. A facility for validating new tools is introduced as a platform to enable and accelerate turbine thermal field research. Additionally, a framework for the adoption of novel and thermally optimal plant operation techniques in real steam and gas turbines is presented. The results and tools from this work already enable further study in the Oxford Thermofluids Institute and Mitsubishi Heavy Industries (MHI).

1.3 Thesis scope

The design and philosophical shift in the operation of power generation systems is anchored in the abundance of clean energy sources and the need to redefine energy efficiency from short-term plant efficiency to overall system efficiency. With 173,000 TW of solar power incident on Earth, this world's renewable energy source is already 10,000 times the world's total energy consumption [20], highlighting the need for increased utilisation of clean energy sources. Utilising them improves the overall system efficiency of global energy systems and shifts the design principle of power generation. The global requirement to decarbonise energy and mitigate climate change further enhances the effort to transition energy sources, but the associated challenges of thermal stresses must be addressed.

This work proposes foundational methods underlying the operational philosophy changes of turbine parts by transforming the solid domain from a structural component to an active control system, enabling turbine operational flexibility. It develops and illustrates methodologies for optimising the thermal gradients, focusing on turbine casing, providing a detailed understanding of the complex physics of conjugate solid and fluid processes. The scope of this thesis comprises:

1. To understand conjugate thermal and flow physics of power-generating systems.

2. To propose novel fast solver methods that could enhance thermal analysis of turbines and enable novel methods for optimisation and control of turbine fields.

3. To design novel methods for optimising and controlling plant thermal fields in real-time for steady-state and complex transient processes.

4. To design and present a novel validation platform facility to validate new solvers and analysis tools to enhance further turbine research.

1.4 Thesis Outline

Chapter 1 details the background of the energy challenge and highlights the contribution of this work towards developing methodologies to transform the operational philosophy of turbine casing components and enable operational flexibility.

Chapter 2 reviews the literature on flexible power generation and turbine thermal analysis, optimisation, and control. It highlights the challenges of complex numerical analysis and provides a review of novel methods and fast solver techniques.

Chapter 3 introduces the design of the platform facility, the Oxford Turbine Casing Rig (OTCR), used to validate the new proposed framework for operating turbines flexibly, alongside the complex high-fidelity numerical analysis for the turbine thermal field. The thermal and flow analyses are used to match the operating conditions of the turbine casing with real turbines. Further considerations for the facility, like the mass, operational regimes, temperature rating, and design assumptions, are also presented.

In **Chapter 4**, hybrid numerical analysis with Fluent Conjugate Heat Transfer (CHT) and Thermal Network Models (TNM) are presented for steady-state and transient operations, identifying the key drivers and bottlenecks for turbine analysis and operations. They are further enhanced and validated through seamless data

transfer and validation with physical experiments in the solid and fluid cavity domains. Novel plant analysis methods to enhance operational shifts are introduced for the rapid resolution of turbine fields in both steady and transient states, utilising a hybrid analysis and physical methods approach.

Chapter 5 presents novel active and passive methods for optimising turbine casing thermal fields, demonstrating the changing design of these formerly structural parts to active control systems. The active case involves optimising the thermal boundary heat flux for minimal gradient, while the passive methodology utilises optimised thermal bridges for optimal thermal field distribution on turbine casings. Active and passive methods are presented as complementary methodologies to provide the optimum thermal field that enables the flexible operation of conventional power-generating systems.

It further presents the illustration of the new operational methodology with physical validation tests. Experiments are conducted under controlled conditions equivalent to the optimisation values to evaluate the validity of the methods. New field reconstruction tools, such as autoencoders, are presented for fast visualisation and data transfer, serving as the basis for real-time optimisation in real turbines during their operating regimes. Thermal gradients are measured and analysed, and the optimisation methods are visualised and validated, emphasizing the impact of the transformed design methods for operational flexibility.

Chapter 6 concludes this thesis by summarising the critical contributions and results. It then provides an outlook on global electricity systems and further research required to advance the work in this thesis and to address the overarching challenges of flexible power generation for sustained energy security while accelerating intermittent renewable energy penetration to mitigate global warming.

2

Scientific Background and Methods

2.1 Introduction

This chapter reviews existing research in related areas of operational flexibility in power-generating turbines. It provides an overview of turbine operations and the limitations of flexible operations. It reviews various methodologies for improving flexible regimes, including multiple optimisation and control techniques, as well as machine learning protocols. Bottlenecks for implementing these novel methods are identified, including the complexity and computational cost of accurate analysis as well as the lack of adequate validation methods for real turbine applications. New hybrid approaches are also reviewed, and their limitations and gaps are identified.

2.2 Review of Flexible Operating Methodologies

Turbines are designed to operate under extreme temperature and pressure conditions to achieve high energy efficiency, as illustrated in Figure 2.1 [12]. During turbine operation, the rotor speed is determined by the grid frequency and the number of generator pole pairs. For a two-pole generator, the synchronous speed is 3000 rpm at 50 Hz (as in the UK and Europe) or 3600 rpm at 60 Hz (as in North America). Four-pole generators operate at 1500 rpm (50 Hz) or 1800 rpm (60 Hz) for larger machines where lower rotational speeds are mechanically preferable [12]. At

these operating speeds, thermal expansion and centrifugal stress have multiple mechanical implications, including vibrational and thermal stresses. These turbines are characterised by multiple operational regimes, including:

- cold-start, which occurs when the High Pressure (HP) and Intermediate Pressure (IP) Inner casing is $< 170^0$C,
- warm-start occurs when 170^0C $<$ casing temperature $< 430^0$C, and
- hot-start happens when the inner casing temperature is $> 430^0$C.

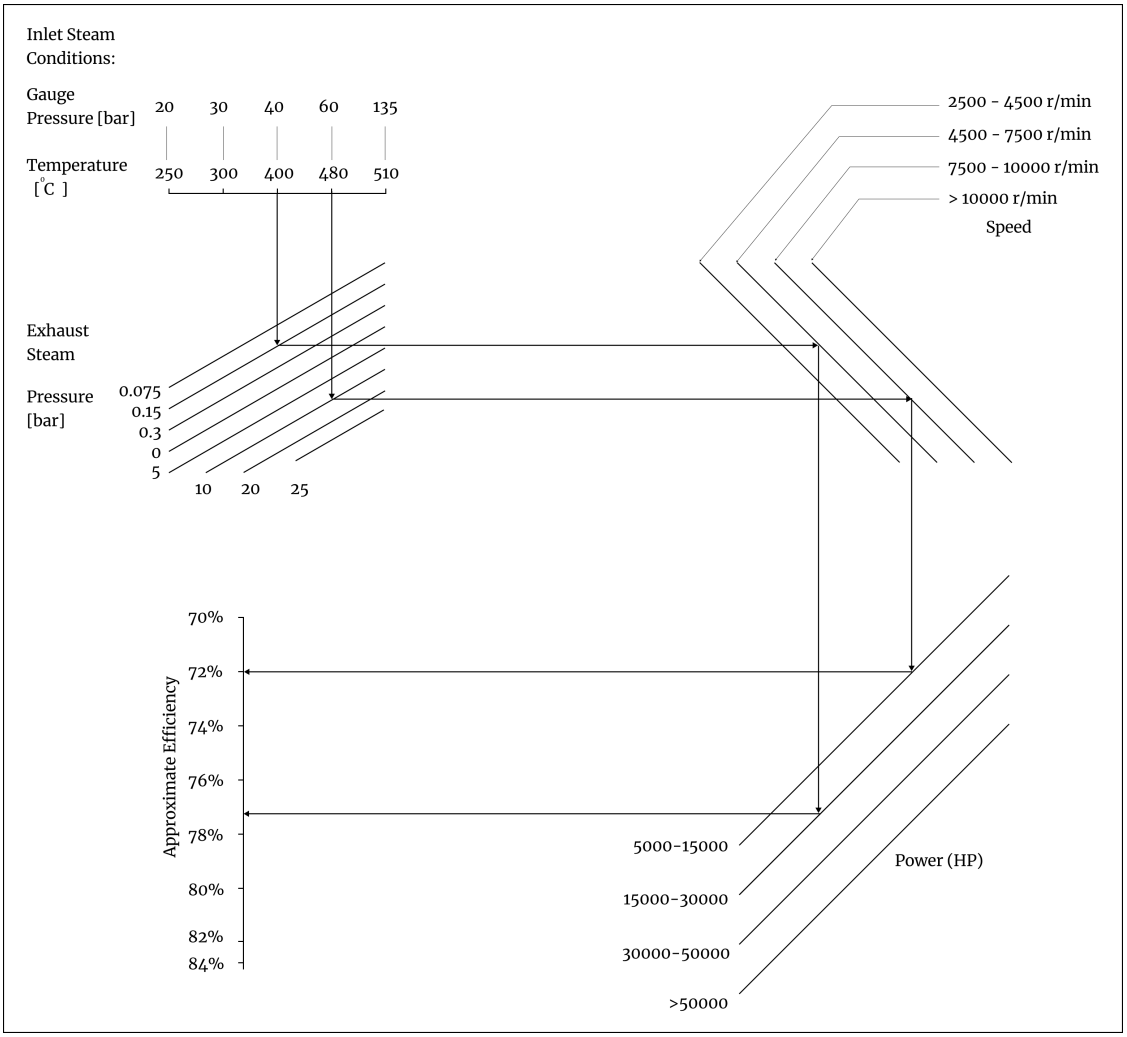


Figure 2.1: Turbine operating envelope showing temperature and speed conditions for cold, warm, and hot start regimes relative to the design efficiency point, based on industrial data [12].

High operating temperatures, pressures, and speeds necessitate turbines with thick casing components and unequal geometry parts, which in turn result in thermal field variations, thermal gradients, and stresses that must be maintained within the allowable material limits based on the material used for turbine casing parts, which is typically a low-alloy or carbon steel. For convective-cooled turbine blades, temperature differences across the thin metal skin through the thermal barrier coating are as high as 540 K, resulting in thermal stresses of up to 500 MPa, equivalent to the yield strength of these materials, which should not be exceeded based on turbine designs. [16, 21]. In addition to the previously stated effects of distortions and the cat's back effect, as discussed in **Chapter 1**, turbine components exhibit creep, the time-dependent thermal deformation of turbine components under thermal stresses, which is exacerbated by thermal gradients [16, 22]. A $\pm 15^0$C in blade metal temperature can halve or double its creep life, while a $\pm 30^0$C change could halve or double its low cycle fatigue life [23]. Controlling these stresses requires a slow and careful start, with preheating, vacuuming, and other processes, to manage thermal stresses within the material's allowable limits and avoid failure.

Before a cold start-up of a steam turbine, a vacuuming process is performed in which the turbine cavity is evacuated to sub-atmospheric pressure with gland steam sealing. Gland steam is low-pressure steam injected into the labyrinth seals at the rotor ends to prevent air ingestion into the turbine cavity and to maintain the vacuum required for efficient low-pressure steam expansion. The injected gland steam interacts with the residual air and condensate within the cavity, producing a mixed-flow thermal environment that influences the initial temperature distribution of the casing and rotor before the main steam flow is admitted [19]. This vacuuming phase, typically during a cold start, is a critical factor in the turbine's initial thermal state. To operate turbines within the limits of allowable stress, start conditions are categorised based on the prior thermal state of the turbine as follows [19]:

1. Turbine cold start - Under such conditions, the turbine undergoes prolonged heating up while the rotor operates at varying rotational speeds until thermal

stability is attained. Typically, this process takes > 72 hours for preparation to start and 3 hours to start up.

2. Turbine warm start - Is required if the duration of the turbine idle time is 8-60 hours, requiring up to 2 hours of turbine restarting time.

3. Turbine loading from a hot state - Under this condition, the thermal field must be closely monitored and controlled to ensure that a temperature change does not exceed 2-3^{0}C on the casing. The restart time for ramping up load under a hot start condition is typically 10 minutes.

Note the safe operating times in hours and day scales. However, new adaptations are required for these start-up, shut-down, and ramp rate timescales to change to minutes, compatible with the intermittency cycle of renewables. The thermomechanical implications of this operational shift are the cyclic heating and cooling with constraints to expansion (compressive) and contraction (tensile) stresses [16, 19].

The requirement of cyclically changing the load conditions through rapid ramps, startups, and shutdowns further amplifies thermal stresses [24]. These operations significantly increase the impact of low and high cycle fatigue associated with the restrained thermal expansion and the temperature gradients, resulting in compressive and tensile forces and creep that could shorten the design life of turbine components from the 100,000 expected operating hours [25]. Calculations based on material properties place a theoretical limit on this ramp-up time. For instance, the warm start scenario from 170^{0}C - 430^{0}C at a safe temperature change rate of 3^{0}C/minute constraints the restart time to 1.5 hours [16, 19]. Changing the scale to minutes, without solving for the compressive and tensile stress constraints, would lead to failure. In addition to the high-temperature gradients, the complex cavity flow regimes that transition from forced convection to mixed and natural convection flow, as illustrated in Figure 1.6, result in complex heating patterns [19]. The differential expansion between thinner casing surfaces and thicker flanges causes transverse deformations. The condensation effect and fluid flow result in higher temperatures at the top of the casing, causing an upward bowing known as the

cat's back effect [26]. These transverse deformations and the cat's back effect, driven by fluid-solid interactions, reduce rotor-casing clearances impacting turbine efficiency and reliability [27].

To prevent the damage that could result from creep, high-cycle fatigue, cat's-back effect, and transverse deformation, the complex conjugate thermal fields in turbines must be understood. Similarly, clearances between the bladed path and the casing must be rapidly and accurately predicted through fast thermal analysis for optimal thermal operations and control.

2.3 Computational Challenges of Flexible Operation

Numerical analysis methods have been proposed to resolve turbine thermal fields. For large and intermediate pressure turbines, a full 3D model is set up using the conjugate heat transfer (CHT) model using the commercial tool *ANSYS CFX* [11, 28]. Figure 2.2 shows the computational domain used for the steady-state and 100 h natural cooling transient numerical analysis with bidirectional coupling of computational fluid dynamics (CFD) and finite element analysis. Note the fine mesh near geometrical hotspots, such as the seals, to capture thermal effects.

The total heat flux at the outer casing, $\dot{q}_{\mathrm{OC}}$, has radiative, natural convection, and forced convection components, as shown in Equation 2.1:

$$\dot{q}_{\mathrm{OC}} = \dot{q}_{\mathrm{rad}} + \dot{q}_{\mathrm{nat.conv}} + \dot{q}_{\mathrm{forc.conv}} \tag{2.1}$$

where $\dot{q}_{\mathrm{rad}}$, $\dot{q}_{\mathrm{nat.conv}}$, and $\dot{q}_{\mathrm{forc.conv}}$ are the radiative, natural convection, and forced convection heat flux components [$\mathrm{W\,m^{-2}}$] respectively.

Direct resolution of the convective terms in Equation 2.1, particularly $\dot{q}_{\mathrm{nat.conv}}$ during long transient cooling processes, requires explicit modelling of buoyancy-driven cavity flows over durations exceeding 100 h, which is computationally prohibitive [29, 30]. To address this, an *over-conductivity* approach is adopted [31], in which the convective heat transport is replaced by an artificially enhanced

fluid thermal conductivity: $k(T) = K(T)\,k_{\text{air}}(T)$, where $k_{\text{air}}(T)$ is the standard thermal conductivity of air and $K(T) > 1$ is a temperature-dependent correction factor calibrated against experimental measurements [31]. *Over-conductivity* refers to a fluid conductivity that exceeds its true molecular value, with the excess capturing the convective heat transport of Equation 2.1 without requiring explicit resolution of the flow field.

The results in Figure 2.3 are validated against solid domain temperature data, with deviations reported within acceptable tolerances [11]. However, the results focus on the solid domain. They are used for the redesign of labyrinth seals but cannot predict the complex fluid domains that could be responsible for the measurement errors and without which robust designs will be challenging. These domains are computationally demanding due to the large number of cells, making them prohibitive for fast optimisation methods.

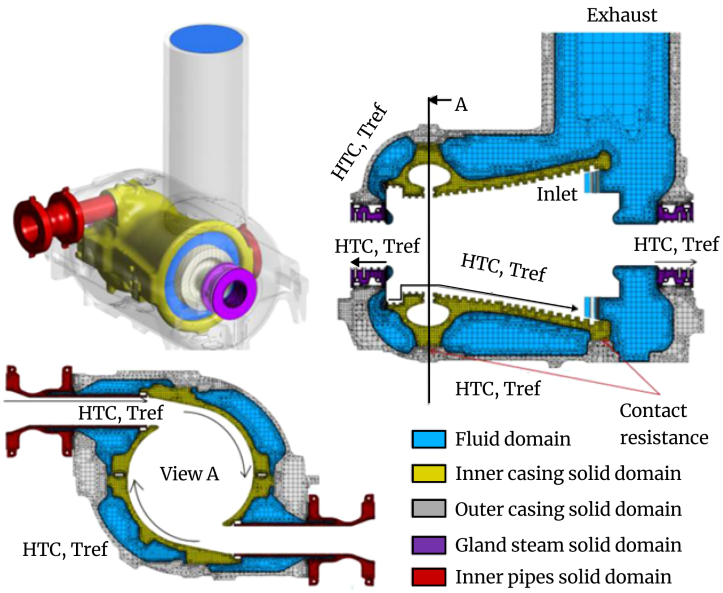


Figure 2.2: Conjugate heat transfer (CHT) computational domain for an intermediate pressure steam turbine, with refined mesh at seal and geometric hotspot regions [11].

Finite element analysis (FEA), using a one-dimensional simplified analytical model (fluid domain) and a two-dimensional planar FEM (solid domain) method are used to predict steady-state and transient thermal fields of the inner casing detailed

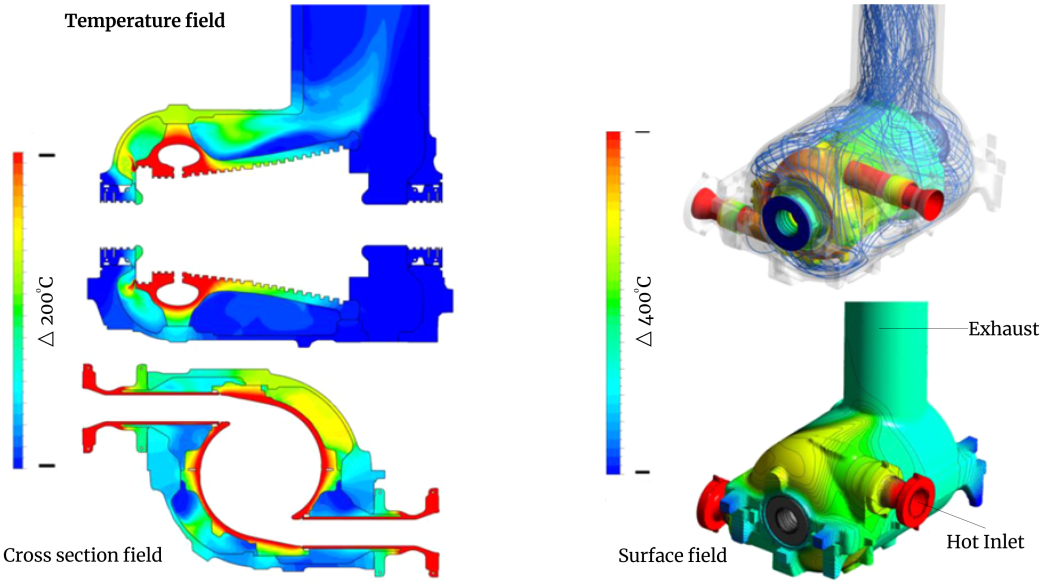


Figure 2.3: Steady-state conjugate thermal fields showing solid and fluid domain temperature distribution and heat transfer for an intermediate-pressure steam turbine casing [11].

by Wang et al. [32]. The model makes several simplifying assumptions, including constant boundary temperatures, non-condensing steam, and the assumption of radiative heat transfer. It also assumes a linear fluid-solid boundary heat transfer coefficient (HTC). The author discretised the solid field into 775 grid elements and solved for the temperatures of adjoining nodes using Equation 2.2. The fluid domain HTC was determined using Equations (2.3), (2.4), and (2.5) where the steady-state is assumed to be attained after 36,000 seconds (10 hours). The oversimplification of the solution, which involves a 1D fluid and a 2D solid, may fail to capture the 3D fluid field and solid circumferential variation or axial effects. The assumed HTC conditions may also underrepresent the startup dynamic, particularly in a complex HTC field that varies both temporally and spatially.

$$\rho V_{i,j} C \left(T'_{i,j} - T_{i,j}\right) = \Delta t \frac{k}{d} S \left(T_{i-1,j} + T_{i,j-1} + T_{i+1,j} + T_{i,j+1} - 4T_{i,j}\right) \tag{2.2}$$

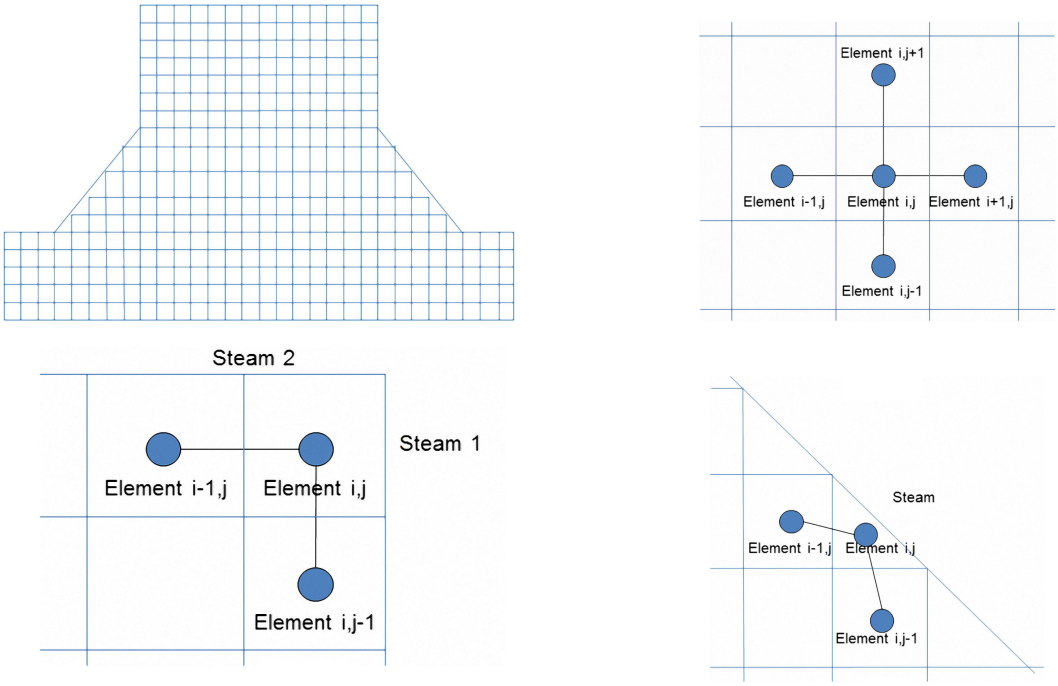


Figure 2.4: 2D finite element discretisation of the turbine inner casing into nodal grid elements used for transient thermal field prediction [32].

$$h_2 = \frac{0.023\, k\, \mathrm{Re}_2^{0.8}\, \mathrm{Pr}_2^{0.4}}{D_2} \tag{2.3}$$

$$h_{2t} = \begin{cases} \frac{t}{36000}\, h_2, & \text{if } t \leq 36000 \text{ (s)} \\ h_2, & \text{if } t > 36000 \text{ (s)} \end{cases} \tag{2.4}$$

$$T_{2t} = \begin{cases} 15 + \frac{t}{36000}(T_2 - 15), & \text{if } 0 \leq t \leq 36000 \text{ (s)} \\ T_2, & \text{if } t > 36000 \text{ (s)} \end{cases} \tag{2.5}$$

All fluid properties are evaluated at the local bulk steam temperature T_2 at the respective flow location [32]. The initial temperature of 15°C in Equation 2.5 represents the ambient air temperature at the start of a cold start-up. Steam temperatures and convective heat transfer coefficients are then assumed to increase linearly from this ambient state to their respective steady-state values during operation. The Prandtl number exponent of 0.42 is adopted directly from Wang [32]. Huo [33] utilised the three-dimensional Reynolds-Averaged Navier–Stokes (RANS) models with advanced CHT methodologies in [34–36] to capture the complex flow structures and boundary effects between fluid and solid domains to analyse cooling

effects on intermediate pressure (IP) blades. The model is yet to be validated by physical measurements, which reduces confidence in its industrial adoption. It only models steady-state conditions and neglects the complex transient states and intricate cavity fields, which have a significant impact on turbine thermal behaviour.

Some challenges, including flow complexity [17, 30] and the unsteady timescale problem [37], significantly impact the use of high-fidelity numerical analysis, such as CHT, especially for long periods of transient simulations [38–41]. Pilkington performed a high-fidelity Large Eddy Simulation (LES) with 0.1 s timestep over 200 seconds for a natural convection turbine shutdown process [30]. They found that commercial CFD models yield more than 20% difference in wall heat transfer prediction compared to physical measurements because they use the Simple Gradient Diffusion Hypothesis (SGDH), which assumes the proportionality of turbulent heat flux to the mean temperature gradient. For a cylindrical-type wall, such as a turbine casing, this assumption fails to hold for natural cooling processes. Natural cooling requires resolving the normal and parallel wall components for accuracy, as the parallel heat component, which was previously insignificant during turbulent flow, becomes more significant for natural flows. The complexity of this challenge for real-world applications cannot be overstated. The ability to tune the normal and parallel wall coefficients for an entire range of flow regimes, ranging from natural to mixed and forced flows, makes it extremely challenging to resolve complex fluid fields. New thermal field solvers must be characterised by the universality of turbulence models for various operational regimes. Yet, the work is limited, with a total timescale of 3 minutes compared to several hours of natural cooling processes in turbines. It also focuses on the near-wall phenomenon, neglecting the complex and intricate cavity flows that occur in mixed and forced states.

These complex and dynamic cavity flows, with their significant impacts, are yet largely understudied. Murat developed a new RANS-based turbulent model with a novel turbulence closure framework for mixed convection cavity flows [42]. The research identifies several additional challenges in fluid domain modelling, including the inaccurate prediction of Reynolds stress and boundary layer treatment [43, 44],

the time required to achieve accurate solutions from scale-resolving simulations, and the convergence difficulties of Reynolds stress models [45, 46]. The proposed model enhances the transport equation and turbulence heat flux solutions to capture non-linear coupling between momentum and heat transfer. While it improves accuracy, it is more complex than the normal RANS equation and requires significant computing power. It is also validated on a very short timescale using a simplified turbine geometry with two concentric cylinders, establishing the need for further validation of this model.

The unsteady time scale problem was detailed by He and Oldfield, who identified the problematic nature of conjugate solutions for unsteady flow due to the mismatch of the solid and fluid timescales [37]. First, the speed in turbines could be in the order of 3×10^2 ms^{-1} blade row axial dimensions are in the order of 10^{-1} m, and fluid structures are in the order of 3×10^{-4} s. Because the high thermal mass of the solid is characterised by slow temperature change, the time disparity between solid and fluid domains is in the order of 10^4. The additional computational effort required for solid analysis is demanding and a significant bottleneck in fluid-solid coupled transient thermal analysis. To address the timescale disparity, He presented a hybrid approach that couples time-domain fluid and frequency-domain solid conduction, continuously updating the Fourier transform at the interface to yield accurate, unsteady results. The methodology is only validated with quasi-3D models rather than a real plant. It is also unclear what the impact of the independent solutions will be, as the validation is limited to simplified geometries rather than complex turbine geometries.

The timescale disparity justifies the use of the quasi-steady, loosely coupled CHT for forced convection heat transfer, as detailed in [47, 48]. These methods are primarily used for forced convection, particularly in steady-state analysis. Like forced convection, coupled solutions for natural convection [49] are computationally demanding. Additionally, commercial solvers face a numerical stability challenge that limits the time step size to very small time steps for transient processes, making solutions prohibitive for long shutdown processes [37, 50]. Fadl et al. demonstrated a loosely coupled CHT for efficient and accurate simulation [29] with

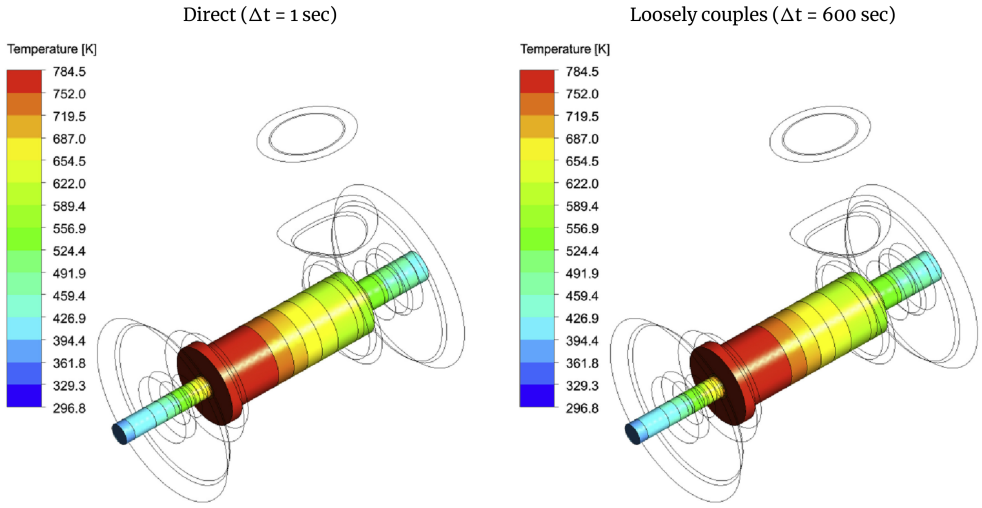


Figure 2.5: Effect of timestep size on transient natural cooling temperature prediction from a loosely coupled CHT model, demonstrating the trade-off between computational cost and temporal accuracy [29].

simplified geometry of an IP turbine comprising the outer casing, inner casing, rotor, bladed steam path, thermal insulation, and fluid domain [29]. While the simulation makes simplifications like constant external wall HTC (10 $\mathrm{W\,m^{-2}\,K^{-1}}$) and constant temperature = 295 K, with a constant temperature and HTC set at the rotor end to model the bearing, the method is 240 times more efficient and provides thermal field solutions at significantly larger timestep sizes, as shown in Figure 2.5. However, it is only validated against over-conductivity correction models. The limitations in validation and oversimplification of the model point to potential inaccuracy and the need for further enhancement in the model and validation methods of conjugate and high-fidelity numerical analysis. However, not simplifying the model requires extreme compute power and timescales that are not realistic if thermal fields of turbines are to be analysed and optimised in real-time to minimise thermal gradients and stresses.

2.4 New Methods and Limitations

Given the challenges of achieving high-fidelity coupled models, a critical requirement for thermal field prediction, optimisation, and control, new methods have been

proposed to predict plant thermal fields rapidly. Baker in [24, 51] presented new approaches to enhance the speed of thermal analysis of power-generating turbines. A method of hybridising high- and low-fidelity solvers in parallel, alongside data interpolation, demonstrated the ability to provide reliable accuracy while achieving high speed and solution resolution for turbine flow and material physics.

Fast solvers and digital twins are proposed by [52–55]. Fast developed an online artificial neural network (ANN) model monitoring system for the condition, monitoring, and diagnosis of a combined heat and power plant in Sweden [52]. The multi-fuel plant consisted of an SGT800 gas turbine, a heat recovery steam generator (HRSG), a steam cycle utilising biomass, a steam turbine, and pre-heaters. The ANN models are trained on 5-minute averaged plant training data from a 3-month operation. Trained data is used to predict plant performance parameters, such as power output, pressure, and temperature, at specific plant locations with minimal error. Predicted values are displayed using the graphical user interface (GUI) to aid operators. Dominiczak et al. demonstrated a non-linear auto-regressive neural network with exogenous input (NARX) model of a steam turbine rotor to control steam turbine stress at critical stress points [53]. The model trained a neural network using turbine transient operating data, including steam temperature, pressure, turbine rotor speed, and load, to define the turbine load cycles. The neural network predicted critical parameters in the turbine within ±5% error for warm start-up and 5-15% for cold start-up compared to finite element analysis. Xin et al. used a stacked autoencoder and an Elman neural network, trained on data including the temperature at the flue gas side inlet, air side outlet, flue gas side outlet, and air side inlet to effectively critical stress factors on components of steam turbine rotors and predict their deformation to avoid damage to sensitive turbine components.[55].

Digital twin models have been utilised on 330 MW and 1000 MW turbines' operation data, including temperatures and pressures of steam turbine control stages. The digital twin model features flowrate and efficiency calculations over the full control stages with limited measurement data. The model predicts the fields, including the exit temperatures and pressures for each control stage, with less

than 1% error [56]. Moroz presented an off-design digital twin model for estimating performance and predicting power correction factors for a 166 MW gas turbine, providing good accuracy for steam turbine characteristics such as mass flow rate and steam temperatures [57]. Fast presented a deep, fully convolutional network to predict and reconstruct rotor stress fields based on a few temperature measurement locations and finite element analysis datasets [58].

While these novel models are invaluable for localised functions like local area stress prediction, they are developed based on often limited plant components with few and simplified boundary conditions that neglect the overall system domain. Moreover, they focus on the few validation points on the rotor or specific control stages. In reality, optimising a single plant variable like temperature in a specific boundary without understanding the impact on other field parts limits confidence in the application of new models and is challenging. Additionally, relying on these models remains unconvincing. The challenges of fluid-solid interactions and the limitations of black-box approaches mean that industrial confidence in the direct application of these models to real turbines remains limited. The above-described models largely neglect the complex fluid and transient start and shutdown physics, which have been identified as a significant challenge to developing robust prediction and control tools [59]. Model validation with physical experiments is equally critical for developing robust, fast-solve, and digital twin models to enable the needed optimisation techniques.

2.5 Validation Challenges

Beyond the complexities of fluid physics and conjugate solid-fluid interactions, physical validation measurements are required to bolster confidence in new tools. Current physical validation of steam and gas turbine thermal models is largely restricted to sparsely instrumented facilities that measure thermal fields at discrete solid domain points, as illustrated in Figure 2.6. Although these studies demonstrate reasonable agreement between measured and predicted temperatures, validation is confined to accessible components such as the outer casing, where thermocouples

and optical probes can be feasibly installed [11, 31, 60]. Fluid cavity regions, where flow complexity is highest, remain largely unvalidated.

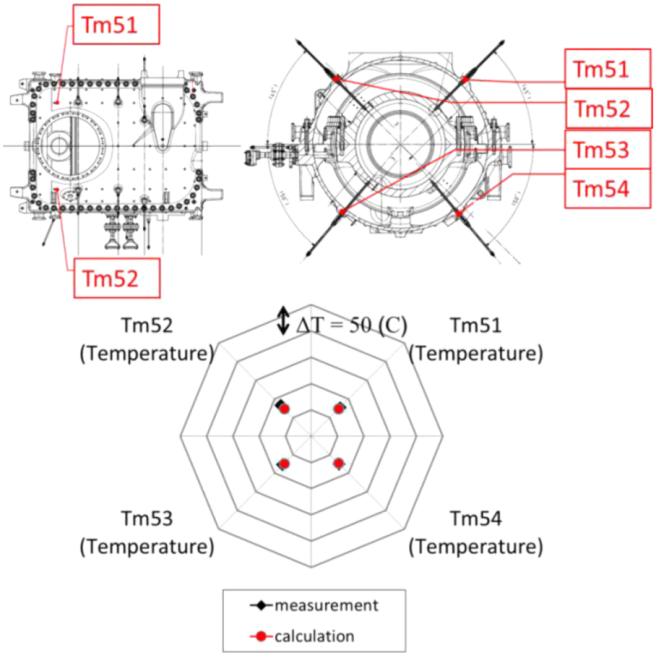


Figure 2.6: Sparse thermocouple instrumentation on the outer casing of an industrial steam turbine, illustrating the limitations of current physical validation data for conjugate thermal models [11].

These facilities, including the SGT800 gas turbine, 330 MW and 1000 MW facilities, have harsh operating conditions that make it challenging to take high-resolution measurements in intricate cavity locations. They are rarely accessible to the wider research community for innovative tests due to their requirement for service and high costs. This restrictive nature allows limited measurements based on fixed plant operations, leaving minimal opportunities to expand the frontiers of research. With minimal fluid cavity and complex field data, new models lack the validation required for plant applicability.

2.6 Applied Flexibility Methods

The real application of methods on plants to enhance flexibility is extremely limited and requires more effort. Kostenko introduces the turbine Hot Standby Mode (HSM), optimising heat transfer using Finite Element Analysis methods across

various regimes of a Siemens Energy plant facility, thereby contributing to more flexible operation [61]. This mode preserves the warm start-up condition for turbine shutdown greater than 40-70 hours by utilising an Electric Trace Heating System (THS) as shown in Figure 2.7, which reduces the turbine restart time. They found that start-up time could be reduced by 60%, which improves the ability to ramp up the turbine, as required for flexible operations, and indicates the potential of thermal heating methods to enhance operational flexibility. However, this method considers the casing as a single unit and simply delivers heat without active discretised control. It is limited by the inability to control localised casing thermal stresses. The methodology also fails to examine the fluid-solid interactions, which could have unforeseen implications.

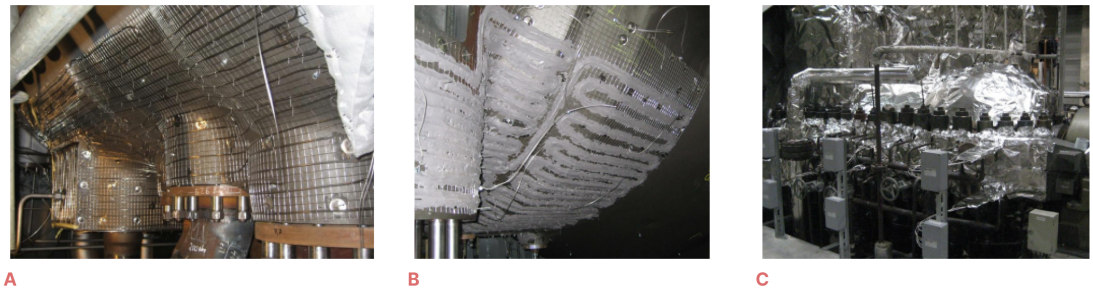


Figure 2.7: Electric Trace Heating System (THS) applied to a Siemens Energy steam turbine casing for hot standby mode: (A) THS elements on outer casing; (B) THS cement application; (C) casing insulation [61].

2.7 Requirements for Flexible Operations

Beyond the limitations of the above-described tools and methods identified in the research on turbine flexibility, a platform system that integrates all novel tools for flexible operations is critical and largely ignored. This requirement is especially true because a turbine is a complex machine with multiple interacting components. However, most developed tools are optimised for local component operation, neglecting the effect on the broader system architecture. For these tools to be adopted in the industry, they must be tested on a robust system with realistic turbine geometry, similar flow conditions, and thermal properties. Figure 2.8 shows

a required turbine operation and control framework for flexible operations. Live plant measurements, high-fidelity solutions, active and passive control, boundary conditions, stress and clearance analysis, and visualisation are crucial to the novelty of digital twinning and optimisation, as well as control, ensuring that systems operate within the limits of engineering design.

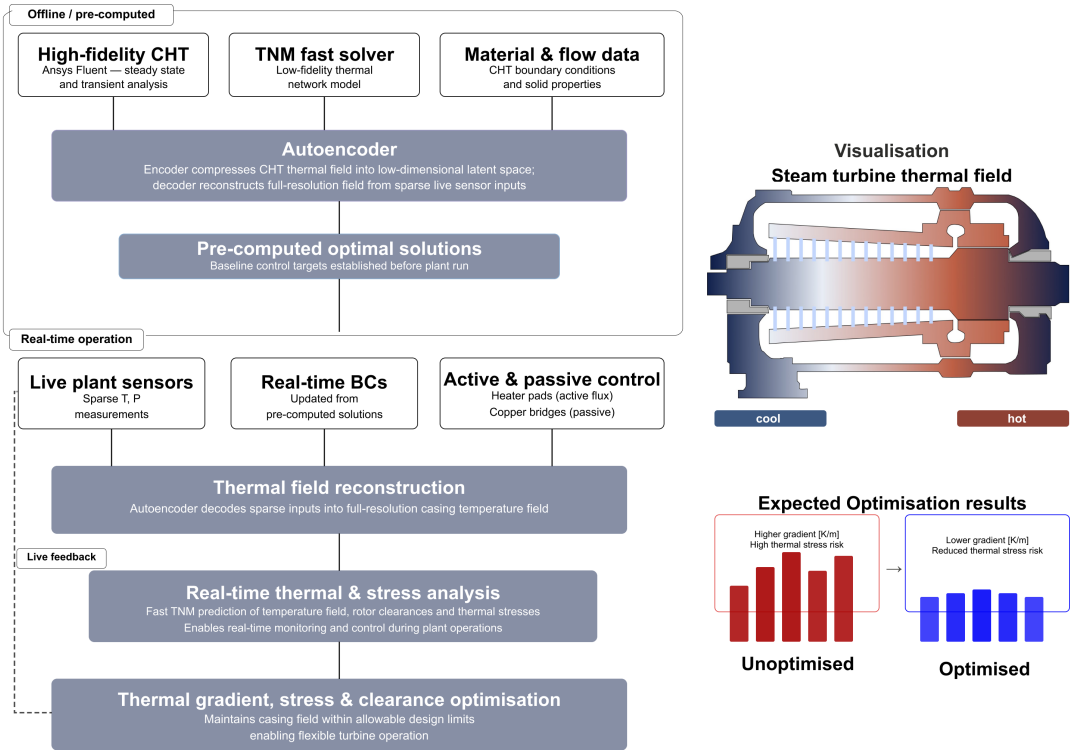


Figure 2.8: Proposed framework for real-time thermal optimisation and control of power-generating turbines, integrating live plant measurements, high-fidelity numerical analysis, active and passive control, and field reconstruction tools.

Data downsampling methods and data transfer between high- and low-fidelity are required to monitor plant fields adequately. The monitoring and prediction of plant behaviour enables the real-time understanding of physics for the optimisation and control of plant conditions such as turbine thermal stresses and clearances, thereby enhancing operational flexibility.

This thesis contributes to the development of these required tools, a significant step towards the validation and adoption of novel methodologies necessary for future plant operations, a missing core component in the literature. It further contributes by illustrating the interdependence of physical measurements and high-fidelity

solvers through automated data resolution and transfer systems. The adoption of the OTCR, with its realistic geometry and flow conditions, and its adaptability for simulating multiple turbine operational regimes and test conditions, enables the tuning of potential universal turbulence models for conjugate thermal analysis. This thesis also demonstrates the use of reduced computational infrastructure and the adoption of novel methods to minimise thermal gradients in steam turbine casings, another critical contribution to future turbine operations.

2.8 Summary

This chapter documents the research into methods applied toward thermal analysis and predictions, which remains a precursor for the optimisation and control of turbine fields. It reviews the concerns associated with extreme operating conditions in flexible power generation and their impact, including faults and failures, on conventional engineering design systems. It explains the requirements to prevent such faults, including fast and accurate numerical analysis layered with novel optimisation and control of thermal stresses. The limitations of accurate numerical analysis, due to its prohibitive computational cost and complex fluid domains, are well-documented, and new methods are suggested to overcome these barriers to numerical analysis. These new methods, including machine learning and digital twinning models, are shown to be advances in research. Efforts have been made to enhance flexible operations like thermal surface heating. However, they are limited due to their localisation, lack of active control frameworks, limited validation, and neglect of complex domains, which remain a black box for fast thermal analysis and optimisation. Without sufficient knowledge of conjugate fluid-solid domain interactions, the validation of new tools, solvers, and processes for flexible power generation remains incomplete. Therefore, the drive to transform the operational philosophy of power-generating turbines from steady operations to flexible operations has some missing research.

A design and optimisation philosophy for turbine parts must be fully developed and implemented. This philosophy requires accurate thermal and flow field analysis,

which necessitates further advances in both numerical analysis and complex physical validation. The whole system framework for such operational changes is understudied. Identifying these gaps, this thesis proposes new methods of turbine thermal analysis, a novel platform facility for complex field validations, and innovative control strategies as a contribution to the body of research and a foundation for the requirements for flexible power generation.

3

Turbine Facility Design and Experimental Campaigns

3.1 Introduction

It is essential to understand and validate the physics of the fluid domain and complex solid-fluid interactions for thermal field optimisation and control. The lack of validation systems in the literature inspires the design and presentation of the Oxford Turbine Casing Rig (OTCR), a turbine casing platform facility, as a unique multi-domain thermal and flow field validation system. Without validation tests through detailed physical measurements, novel numerical analysis models result in reduced confidence for industrial applications due to the well-documented challenges of fluid complexities, wall function, time mismatch, and resolution challenges associated with these models. Previous validation tests have been localised to specific turbine components or fluid flow stages, neglecting the intricate fluid cavity regions with complex flows as described in Section 1.1. Even where localised validation equipment exists, it is often live plants with restricted operating regimes based on peak efficiency rather than flexibility and optimising for control stages, capacity expansion, blade design, and high-temperature use materials rather than active full-domain control for future flexible requirements [62, 63].

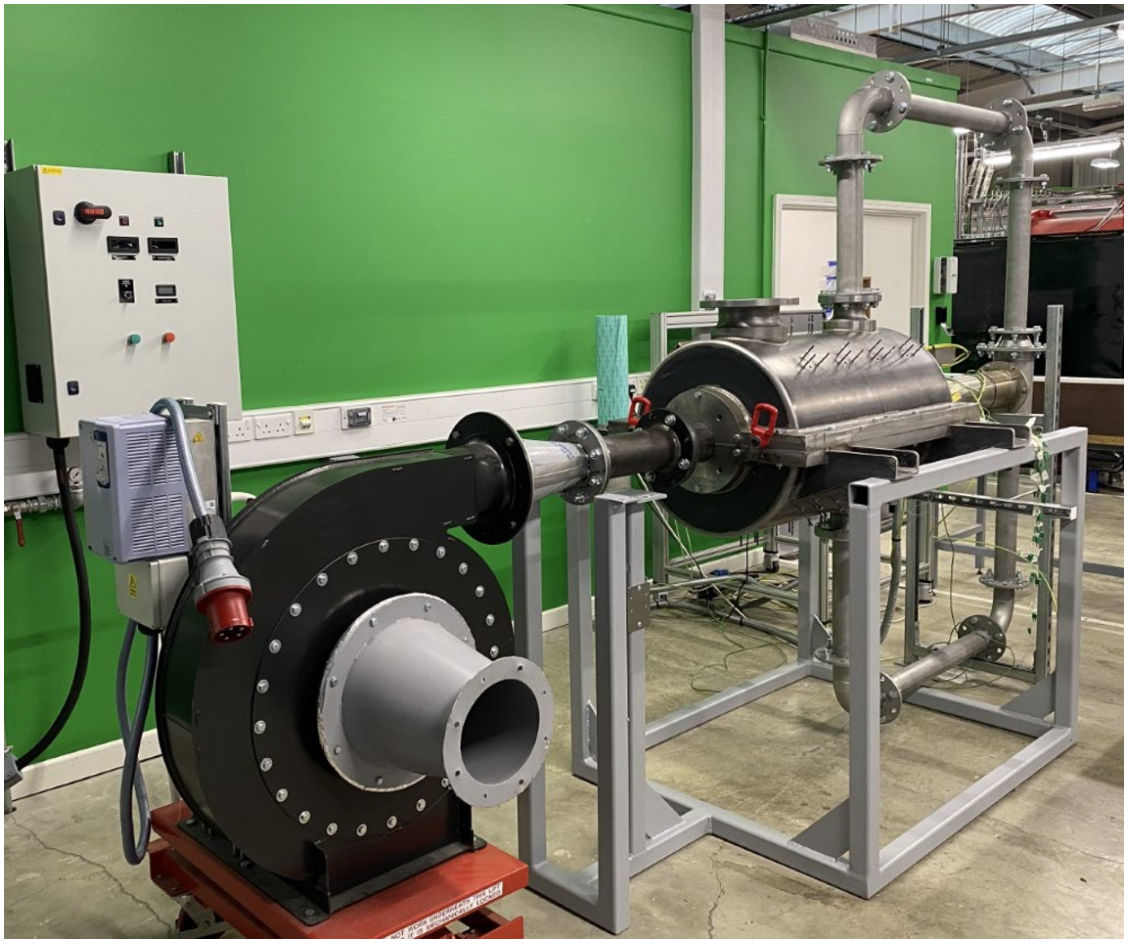


Figure 3.1: A photograph of the Oxford Turbine Casing Rig installed at the Oxford Thermofluids Institute, showing the outer casing, inlet ducting, and instrumentation connections.

Additionally, these existing facilities are inaccessible to the broader research community. The available data are typically based on plant operations rather than innovative designs. These challenges significantly slow the application of new tools and methods for thermal analysis, optimisation, and control. Without new tools and techniques, achieving new turbine design requirements will be impossible, and flexible operations will remain challenging to achieve. Because this thesis explores an approach to changing the operating and design philosophy of turbines towards active optimisation, the test and validation facility is crucial for validating the new tools developed in this thesis. It is also offered to the research community to enhance research on novel turbines.

3.2 The OTCR

In designing a platform facility, the capabilities of the full system to be replicated are incorporated with tolerance for future modifications and evolving design realities. The image of the OTCR is shown in Figure 3.1. The OTCR consists of an industrial fan that convects working fluid, a turbine casing test section, a heater for controlled temperature boundary conditions, and solid and fluid instrumentation, including automated radial motion traverses with fluid motion sensors and thermocouples to measure the fluid cavity fields. Figure 3.2 illustrates the turbine parts in detail as well as the overall flow topology of the turbine working fluid.

The rig design consists of two near-concentric cylinders, modified with an inlet and outlet. Figure 3.3a compares the OTCR with an industrial steam turbine cross-section to illustrate the design rationale. However, the solid turbine shaft is replaced with a hollow shaft, which also serves as the cold crossflow inlet, creating an axial temperature differential across the inner casing. This is designed to replicate the work done between the hot steam and the bladed path to create a temperature differential. The crossflow cold air is heated through electric heaters before the hot air enters the hot inlet as hot annular flow through the main flow path and the inner casing and cavity before exiting through the outlet. Figure 3.3b is a cut-through section of the outer and inner case with turbine-typical features, such as flange thicknesses and non-uniform interfaces. Varying thicknesses, based on the dimensions shown in Table 3.1, enable the measurement of thermal gradient fields. Typically, turbine casings are horizontally split and provide a reliable metal-to-metal joint along the split flange [12]. The injection unit (inlet) is designed with flow control, similar to real turbines, to moderate fluid flow and replicate conditions such as part-load and shutdown regimes. While some components, such as the diaphragm and labyrinth packing, are not included at this design phase, they can be retrofitted later. The horizontal split flanges and the inlet and outlet have some geometric intricacies, including the thicker flanges with design approaches detailed in [12, 64, 65]. They provide a clear view of the complexities and gradients of the thermal field.

Table 3.1: Dimensional Parameters of the OTCR Turbine Casing

Inner casing			**Outer casing**			**Shaft**		
Part	**Parameter**	**Dimension [mm]**	**Part**	**Parameter**	**Dimension [mm]**	**Part**	**Parameter**	**Dimension [mm]**
Body	Length	765	Body	Length	1000	Body	Length	1250
Body	Diameter	240	Body	Diameter	580	Body	Diameter	220
Body	Thickness	8	Body	Thickness	8	Body	Thickness	8
Inlet	Length	180	Inlet	Length	150	Flange	Thickness	10
Inlet	Diameter	80	Inlet	Diameter	80			
Inlet flange	Thickness	45	Outlet	Length	150			
Split flange	Thickness	35	Outlet	Diameter	156			
			Inlet/Split flange	Thickness	60			
			Outlet flange	Thickness	65			

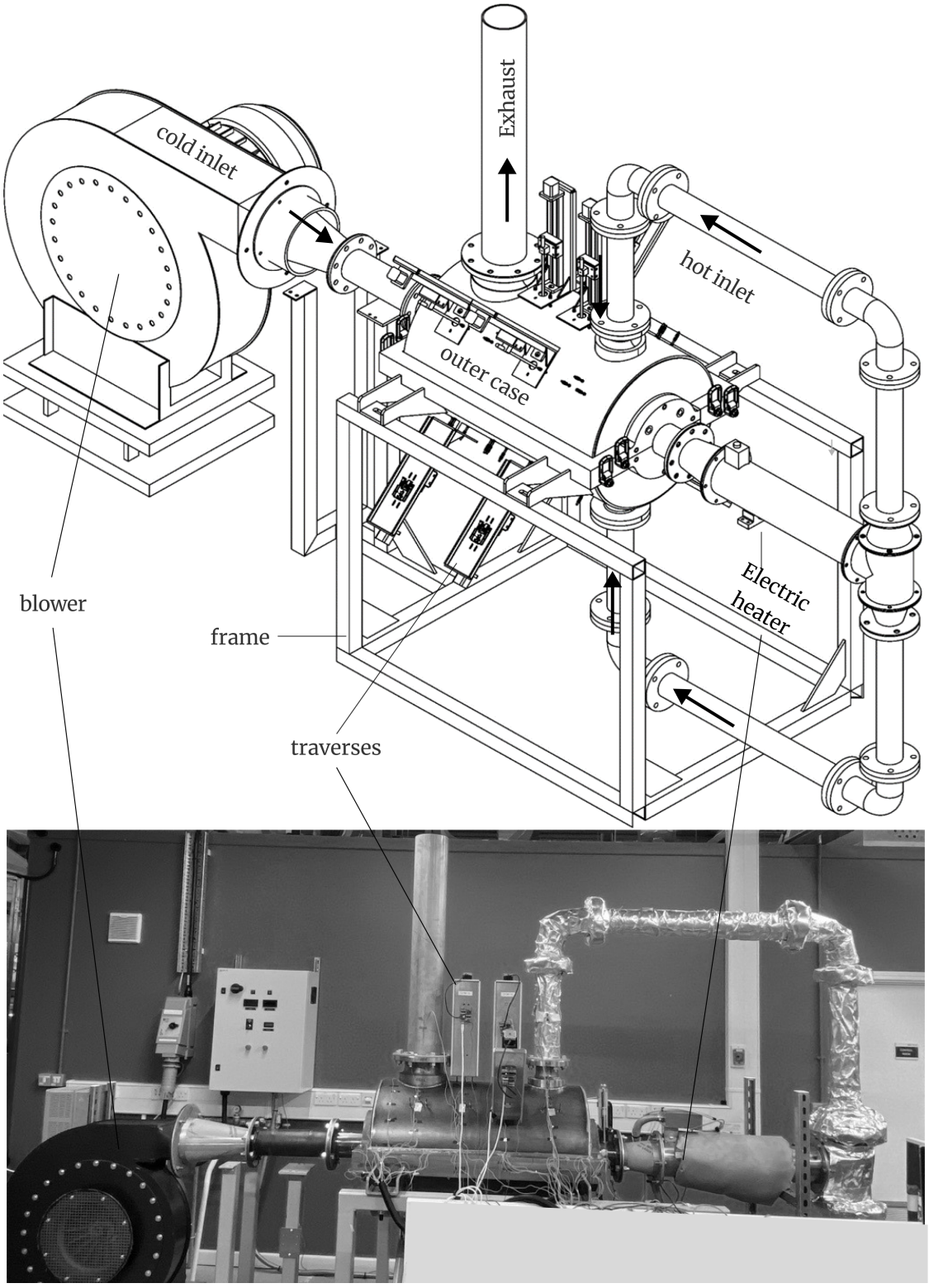
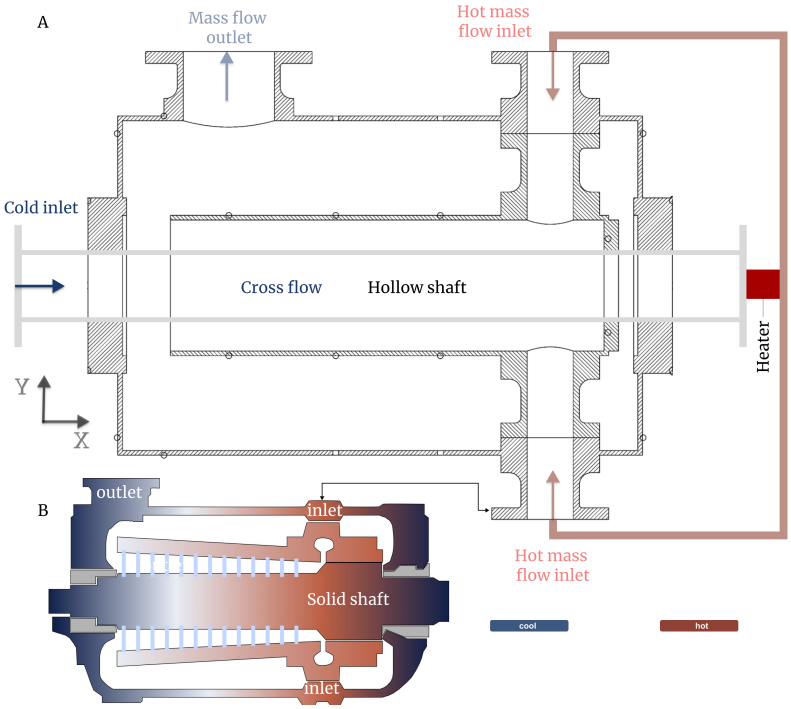
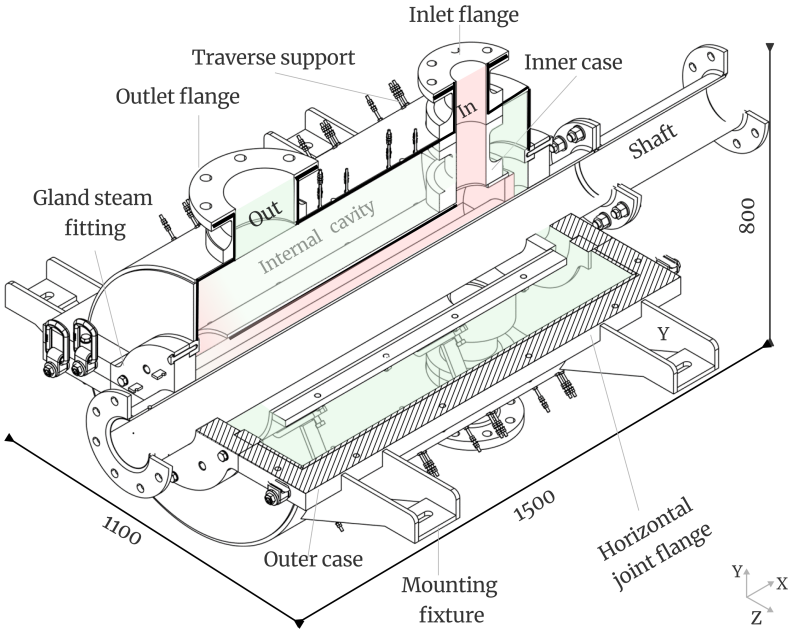


Figure 3.2: The design layout and picture of the OTCR indicating the industrial fan, heater, turbine casing test section, inlet and outlet flow paths, and traverse instrumentation.



(a) (A) OTCR axial cross-section showing the hot annular flow circuit, cold crossflow through the hollow shaft , and the outlet features alongside (B) a schematic cross-section of an industrial steam turbine showing the solid rotor shaft, bladed path, and hot steam inlet regions (B).



(b) Axial cross-section of the OTCR showing the outer casing, inner casing, hollow shaft, split flanges, and inlet/outlet features, with key dimensions consistent with Table 3.1.

Figure 3.3: OTCR design and comparison with an industrial steam turbine.

Table 3.2: Casing material Properties

Component	ρ [kg m^{-3}]	k [W m^{-1} K^{-1}]	c_p [J kg^{-1} K^{-1}]
Outer case	7850	47.6	500
Inner case	7850	47.6	500
Shaft	7850	47.6	500

OTCR's inlet and outlet have flow extension pipes for uniformity of the velocity profile at the inlet boundary condition. It has valves for the main flow control, which determines the operation regime. During natural cooling, the valve is closed to stop the main flow to the turbine. The preliminary design and the calculated parameters before manufacturing the OTCR were temperature, pressure drop, material strength, growth, expansivity, and dimensionless numbers. The material properties of the casing are shown in Table 3.2. Although mild steel exhibits lower creep resistance and high-temperature strength than cast or forged steel alloys used for turbine casings, it is selected as an accessible substitute for evaluating models.

The Biot number is important for determining whether the capacitance method used in finite element analysis (FEA) and thermal network modelling (TNM) can provide reasonably accurate estimates of thermal flow fields [66]. It is defined as $\mathrm{Bi} = hL/k$, where the characteristic length $L = 0.008$ m is taken as the casing wall thickness (the minimum body thickness from Table 3.1), representing the conduction path through which the temperature drop occurs. The convective heat transfer coefficient $h = 40$ W m^{-2} K^{-1} is representative of internal fluid-solid convective boundaries, based on operational data from Mitsubishi Heavy Industries (MHI). The thermal conductivity $k = 47.6$ W m^{-1} K^{-1} is the material property of the mild steel casing given in Table 3.2. We derive $Bi = \frac{40 \times 0.008}{47.6} \approx 6.72 \times 10^{-3}$. Since $Bi \ll 1$, the conduction resistance inside the solid is negligible compared to the convection resistance at the surface. This validates the assumption of a uniform temperature distribution in the solid and justifies the use of the thermal capacitance method.

Preliminary and iterative simulation design was used to determine the temperature range and suitability of the facility. Figure 3.4 shows the thermal field overview of the casing design for a temperature range from 300 K to 900 K. Because of the

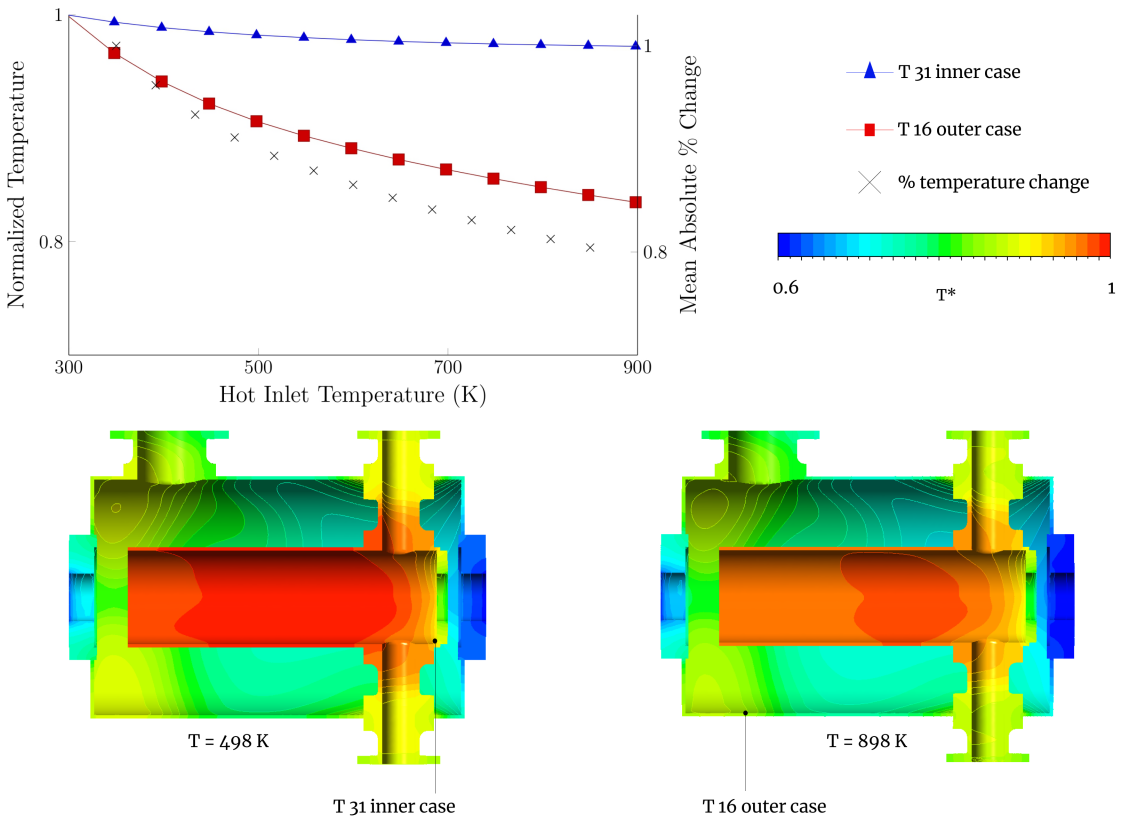


Figure 3.4: Normalised steady-state temperature fields on the OTCR casing for inlet temperatures ranging from 300 K to 900 K, demonstrating qualitative similarity across the range that validates the use of scaled experimental temperatures for comparison with industrial conditions.

limitation of the 40 kW heater [67], which is unable to provide the over 600 K temperature range required for real turbines [68, 69], a study to estimate the change in the thermal field as a result of changing temperature is done. The temperature contour plot displays the normalised fields obtained by $T^* = T/T\,\text{max}$, where $T\,\text{max}$ represents the inlet temperature or the theoretical maximum temperature for the flow simulation, following the normalisation convention adopted in representing temperature fields in the steam turbine literature [31, 61]. The fields show qualitative similarity across the temperature ranges, indicating the viability of lowering the experimental temperatures compared to real turbines in performing validation tests. The thermal contours and gradients are similar, and the change in normalised temperatures was minimal for the temperature range of typical turbine operations. Table 3.3 shows the temperature operating range of the OTCR suitable to meet

Table 3.3: OTCR operating range

Variable	Lower limit	Upper limit
Temperature [K]	273	473
Pressure [atm]	1	1
Mass flow rate [kg/s]	0	0.3

the design constraints while providing viable test information. Note that the convective fluid is not pressurised, and the mass flow rates are based on the capabilities of the blower.

For the rig design setup, understanding the operating regimes is critical to determine the steam turbine possibilities during its operations. It is essential, therefore, to model the capabilities for all potential turbine scenarios, and the OTCR provides the required platform. The OTCR can perform the following operations with equivalent turbine characteristics.

1. Steady-state full and part-load operations
2. Transient start-up and shut-down regimes
3. Ramp-up and down operating conditions
4. Gland steam-mixed flows for vacuum conditioning

These operating regimes result in different fluid flow physics that are critical to the analysis of turbines. In turbine cavities, multiple phenomena occur that determine the flow structures and the physics used to resolve flow and thermal fields. Dimensionless numbers that define turbine cavity flow characteristics are crucial in rig design. Figure 3.5 shows the cavity design, dimensions, and parameters of the concentric annulus of the inner and outer casing used to analyse the dimensionless numbers based on Equation 3.1 for the Grashof (Gr), Reynolds (Re) and Richardson number (Ri), where $\Delta T = T_i - T_o$ and $D_h = 2L_g$.

$$\mathrm{Gr} = \frac{g\beta\,(\Delta T)\,L_g^3}{\nu^2}, \quad \mathrm{Re} = \frac{uD_h}{\nu}, \quad \mathrm{Ri} = \frac{\mathrm{Gr}}{\mathrm{Re}^2} \tag{3.1}$$

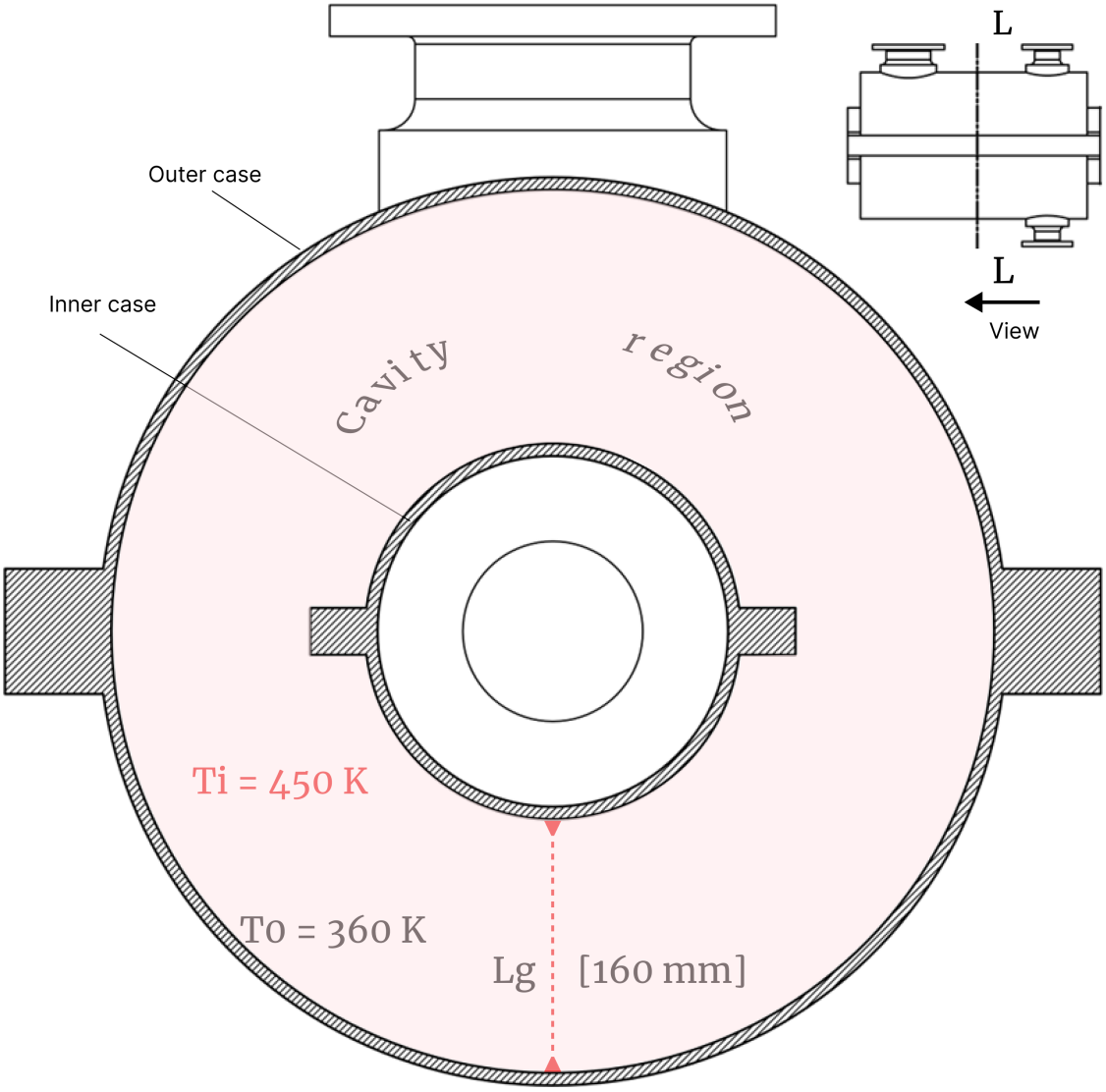


Figure 3.5: Annular cavity geometry of the OTCR showing the key dimensions used to compute the Grashof (Gr), Reynolds (Re), and Richardson (Ri) numbers.

OTCR's operations range from natural convection to mixed flows and forced convection dominance based on MHI-provided data, as shown in Figure 3.6 [17]. The operational regimes for this case, with the full-load steady-state regime ($Ri = 3$ and $Re = 3.4 \times 10^3$) and shutdown regime ($Ri = 5 \times 10^3$ and $Re = 6.8 \times 10^1$), are mixed and natural convection flows, respectively. Traverses and

velocity flow sensors (hot wire anemometers) measure the flow transition between operating points. Corresponding dimensionless numbers imply the transferability of the data and results between the OTCR and a real turbine, satisfying the requirement for validating new tools developed for future operations and design methods of power-generating turbines.

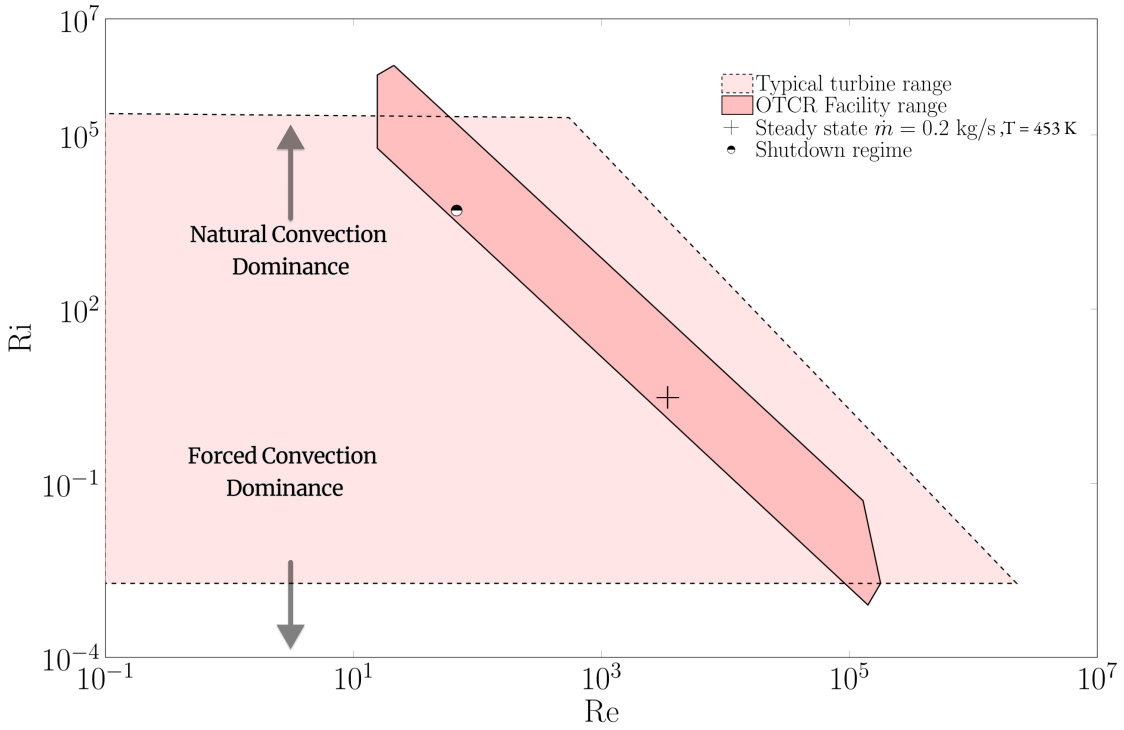


Figure 3.6: OTCR operating envelope in Re-Ri space, showing the range of cavity flow regimes comprising natural, mixed, and forced convection, typical turbine operating range (light red) and MHI target operating range (dark red).

Table 3.4: OTCR Experimental Capabilities

Characterisation Capability	**Enabling Feature**
Casing thermal field	Outer and inner casing
Fluid temperature field	Traverse fittings
Fluid flow field	Traverse and pitot tubes
Rotor thermal field	Retrofittable rotor
Gland steam test	Retrofittable gland steam

Within the operating range, the OTCR has a wide range of operating capabilities detailed in Table 3.4. Future design enablements are incorporated into the facility to

enhance its utility for wider steam turbine capability replication. The gland steam fittings are retrofittable for gland steam experiments, where gland seals replace the fittings in the designed slots to study the effect of start-up and shut-down vacuuming and mixed-flow optimisation designs. The shaft design is compatible with a bladed path to replicate the steam energy extraction and windage heating effect. The wide range of capabilities informs the instrumentation design requirements of the OTCR. Thermocouples, hot wire anemometers, traverses and other measurement techniques can be implemented to obtain the required data and insight for any turbine operating regime and real-time validation.

The structural integrity of the rig installation on the mezzanine floor base was assessed based on the report developed by Glanville in 2018 [70]. There are limits to the weight that the mezzanine floor can support without faults. The total area where the rig will sit lies in the beam section, with a total dimension of 3.4 m x 7.9 m. The floor area has a maximum load limit of 500kg / m^2 and a 450 kg point load limit. Other equipment, such as the blower, must satisfy the mezzanine requirement, with a maximum point load of 1,800 kg for 4 stands of the frame. The proposed rig has a 470 kg mass, allowing enough room for future modification and comprehensive validation.

3.3 OTCR Instrumentation

The measured solid and fluid domain characteristics of the turbine during operation are used to validate new solvers and methods. To enable these measurements, the OTCR solid domain is instrumented with 51 and 33 Type K thermocouples with specifications detailed in [71] on the surface of the outer and inner casings, as shown in Figure 3.7. These 84 thermocouples are optimally placed at design-critical locations on the surface of the turbine casing to monitor solid thermal fields. They are integrated into the data acquisition systems [72] to acquire and record temperature data at a 10-Hz sampling frequency. The solid domain thermocouples are located on the planes A-I defined from the origin and detailed in Table 3.5. Similarly, the inner casing is instrumented with a thermocouple in planes A_i - E_i as defined in

Table 3.5: Planar distribution of thermocouples on the OTCR outer casing

Plane	X distance [mm]
A	0
B	50
C	130
D	241
E	424
F	603
G	786
H	950
I	1000

Table 3.6: Planar distribution of thermocouples on the OTCR inner casing

Plane	X distance [mm]
A_i	241
B_i	424
C_i	603
D_i	786
E_i	890

Table 3.6. The thermocouples are strategically located to capture the intricacies of the thermal field within the design. For instance, Plane G on the outer casing and Plane D_i on the inner casing with the same x-locations have more thermocouples due to the design features of the inlet and split flanges with thicker casing regions. Capturing these temperatures accurately provides confidence in the validation of novel methods to be demonstrated. For easy result comparison across planes, some planes in the inner and outer casing have the same x-distances from the origin.

3.3.1 Fluid field measurements

The OTCR comprises complex fluid cavity instrumentation comprising automated motion traverses with thermocouples to measure the fluid cavity thermal fields. The traverse thermocouples measure near-wall thermal effects and fluid temperatures along multiple axial and radial locations from the outer surface of the inner casing to the inner surface of the outer casing with a 1 mm resolution. The measured fluid

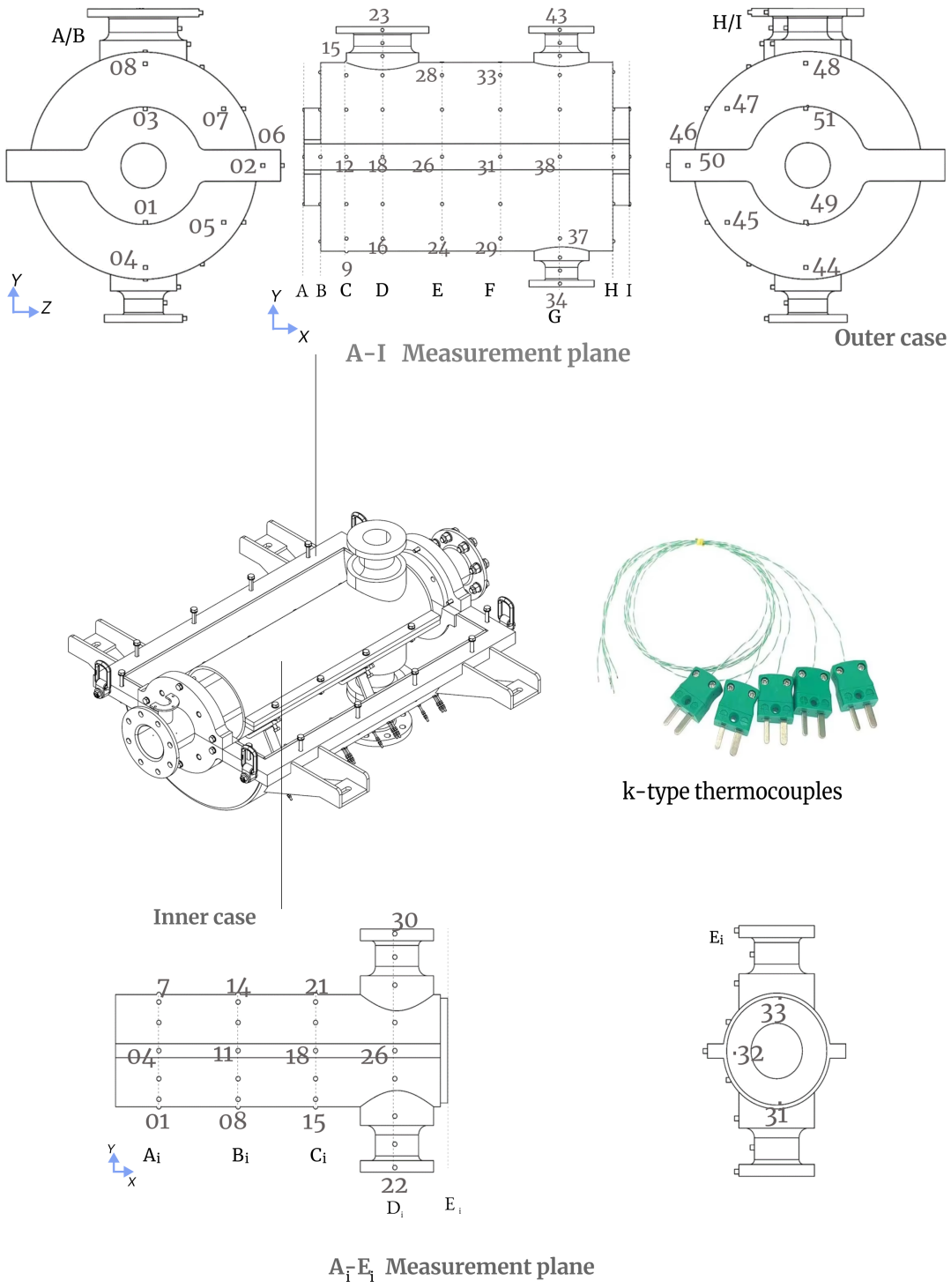


Figure 3.7: Thermocouple distribution on the OTCR outer casing (51 Type-K sensors, planes A-I) and inner casing (33 sensors, planes Ai-Ei), positioned to capture thermal field gradients at design-critical locations.

temperature compensates for the radiative effect of the hot bodies as detailed by Brohez et al. [73]. The traverses are calibrated to a reference point to determine the precise location of the traverse sensors. The detailed traverse is shown in Figure 3.8. By moving it radially using the stepper controlled by the DRV8825 driver [74] mounted on the CNC shield [75], one can measure several fluid temperatures in defined positions. The needle prevents the thermocouple from getting crushed in the downward motion and provides a reliable fluid measurement reference. Figure 3.9 and Table 3.7 provide a guide to locating the 4 traverses used for the fluid measurements. Note that the traverses also enable measurement of velocity fields with hot wire anemometers to characterise mixed cavity flows.

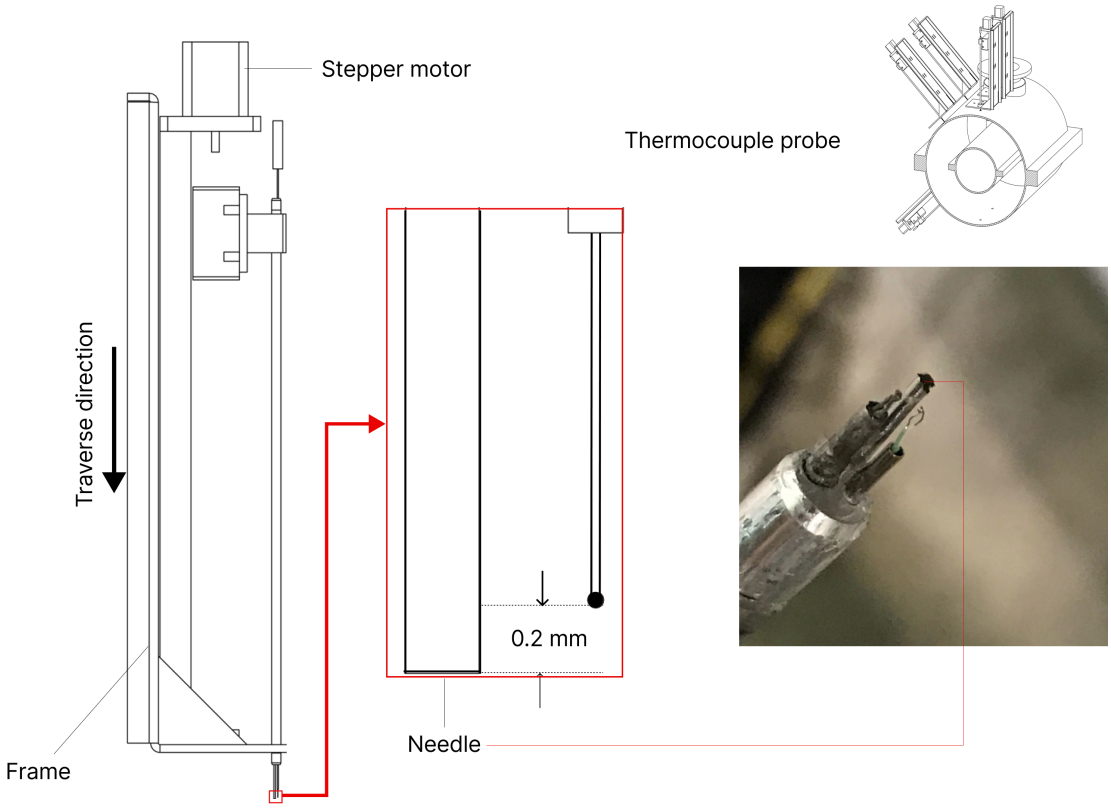


Figure 3.8: Schematic of the automated traverse assembly, showing the stepper motor, driver, needle guide, and thermocouple/hot-wire sensor tip, capable of radial cavity measurements.

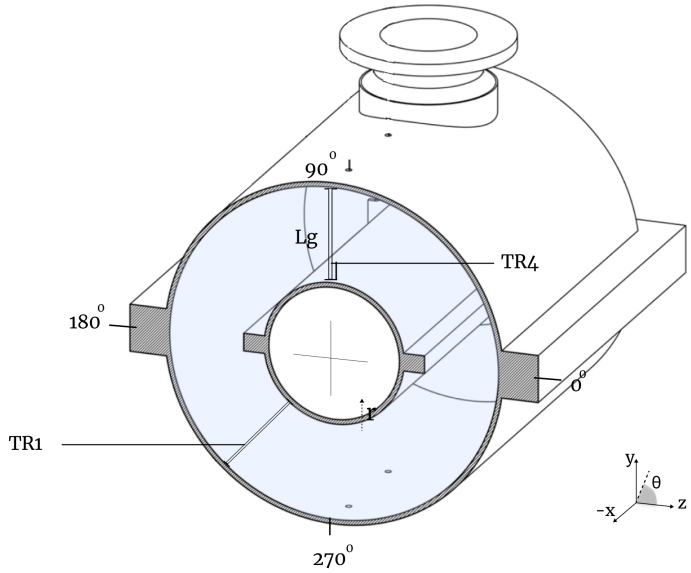


Figure 3.9: Axial and circumferential placement of the four fluid measurement traverses (Tr1-Tr4) within the OTCR cavity. Coordinates are detailed in Table 3.7.

Table 3.7: Traverse fluid temperature measurements locations

Traverse	X distance [mm]	θ^0
Tr1	241	225
Tr2	424	90
TR3	603	135
TR4	603	90

3.3.2 Boundary condition setting

The accuracy of the mass flow rate boundary condition is crucial for cross-validating experimental results with numerical analysis. To determine the mass flow rate accurately, the differential pressure profile in the cylindrical shaft of the mass flow inlet is measured by traversing a pitot tube through the diameter of the shaft. As indicated in the Figure 3.2, the shaft carries the mass flow inlet which also served as counter crossflow working fluid. This mass flow rate is accurately derived by integrating the velocity over the flow area to characterise the main flow properties.

The correlation, $\dot{\mathrm{m}} = \int \rho \mathrm{v} \mathrm{dA} = \int 2\rho \mathrm{v} \pi \mathrm{r}\, \mathrm{d}r$, where $\Delta P = \mathrm{P_T} - \mathrm{P_s} = \frac{1}{2}\rho \mathrm{v}^2$ is used for the characterisation. Figure 3.10 shows the normalised velocity profile for 3 mass flow rates $[\dot{\mathrm{m}} = 0.19, 0.23, 0.26 kg/s]$ shown in Figure 3.11. The uniform

profiles across mass flow rates enable interpolation of the mass flow rates and calculation of the required maximum pressure for a given mass flow boundary. Using this methodology, the required mass flow rate is accurately determined and cross-validated, with a 0.5% deviation compared to analytical models. The maximum pressure differential in Pa is shown in Figure 3.11 for the mass flow rate ranges of the facility. The heater is used to set the temperature boundary condition while the ambient air is measured as the ambient condition during any rig operation.

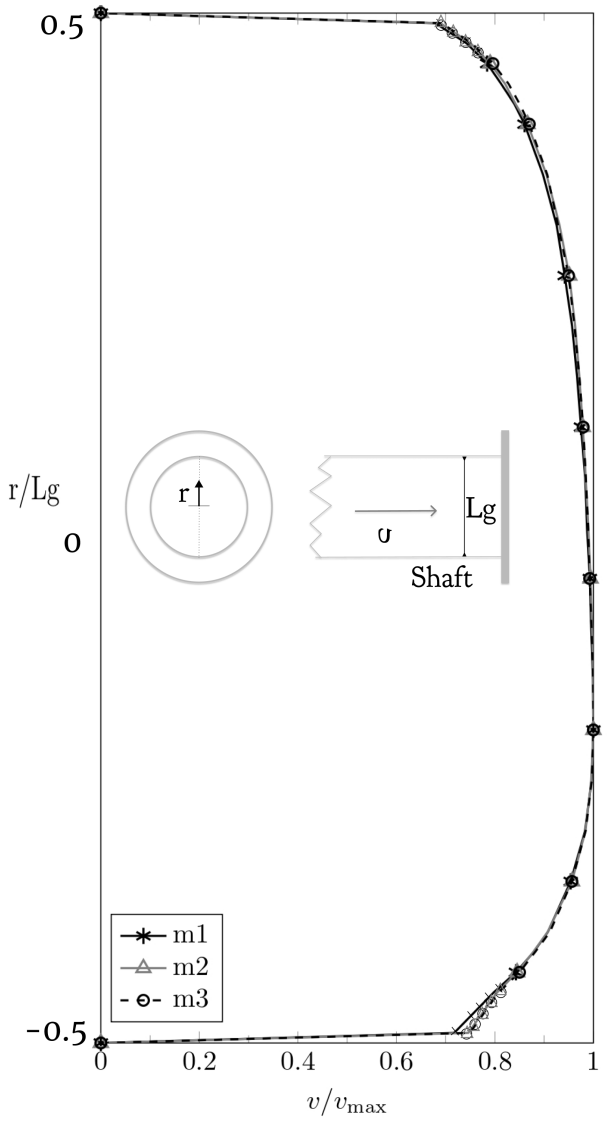


Figure 3.10: Normalised radial velocity profiles (u/u_c) across the OTCR shaft inlet for three mass flow rates ($\dot{m} = 0.19$, 0.23, 0.26 kg/s), showing uniform inlet conditions across the operating range. Radial resolution is 1 mm near the wall, 5 mm in the intermediate region, and 10 mm at the centreline.

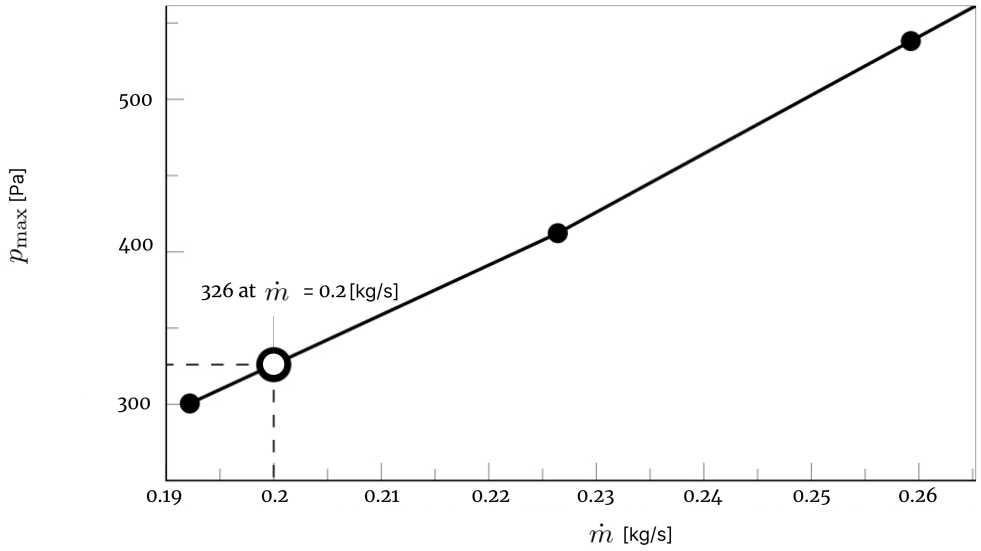


Figure 3.11: Differential pressure versus mass flow rate calibration curve for the OTCR shaft inlet, enabling interpolation of $\dot{m}$ across the full operating range.

An orifice plate was not used for mass flow measurement, as the design required minimal flow distortion through the heater and before the crossflow is split into the top and bottom inlets of the OTCR. An orifice plate requires a minimum of 10 pipe diameters of straight pipe downstream for flow re-development [76], equivalent to 1020 mm for the 102 mm shaft inner diameter, far exceeding the available straight length ($\approx$ 650 mm) upstream of the flow split and incompatible with the uniform velocity profile required before the flow divides between the top and bottom inlets. The pitot tube, by contrast, can be fully withdrawn once the inlet boundary condition has been characterised, leaving the flow path entirely unobstructed to replicate the uniform inlet condition prescribed in the CHT numerical model.

3.4 Experimental campaign

To validate the rig's conformity, steady-state full-load operation and transient natural cooling shutdown regimes were simulated. Figure 3.12 and Table 3.8 illustrate the steady-state experimental campaign, with the counter-crossflow of working fluid serving as the main fluid flow inlet path. Ambient air is assumed to surround the test facility, and the exit pressure is assumed to equalise with the ambient atmospheric pressure. The steady-state experiment includes the following steps.

1. Mass flow rate boundary setting: The industrial fan convects working fluid (air) through the inlet of the experimental facility with accurate and steady mass flow. The shaft cold inlet is also a cross-flow for energy exchange between the hot and cold domains, creating a temperature difference on the inner and outer casings. No air leakage is assumed because the ducting joints are tightly fastened with gaskets to ensure flow conservation. The mass flow rate is determined by the mass flow integration method described in Section 3.3.2. The convective working fluid blower maintains a constant pressure through the inlet.

2. Temperature boundary condition setting: The main flow inlet temperature is set to 453 K $\pm$3 K with an electric heater controlled by a potentiometer system that ensures an accurate and replicable inlet temperature boundary condition.

3. Solid domain temperature measurements: 51 and 33 Type K thermocouples on the surface of the outer and inner casings, as illustrated in Figure 3.7, are connected to the data acquisition systems to acquire and record temperature data at a 10-Hz sampling frequency.

4. Fluid domain temperature measurements: Traverse thermocouples measure near-wall thermal effects and fluid temperatures along multiple axial and radial locations from the outer surface of the inner casing to the inner surface of the outer casing with a 1 mm resolution. The measured fluid temperature compensates for the radiative effect of the hot casing walls by using a two-thermocouple probe arrangement in which two thermocouples of different bead diameters are exposed to the same flow. Since the convective heat transfer coefficient scales with bead diameter whilst the radiative flux per unit area does not, the difference in their readings isolates the radiative contribution and enables correction to the true bulk fluid temperature, as detailed by Brohez et al. [73]. The traverse locations are as illustrated in Figure 3.9.

Table 3.8: Experimental Test Conditions

Variable	Steady-state
Hot inlet	453 K
Cold inlet	298 K
Ambient temperature	298 K
Inlet mass flow rate	0.2 kg/s

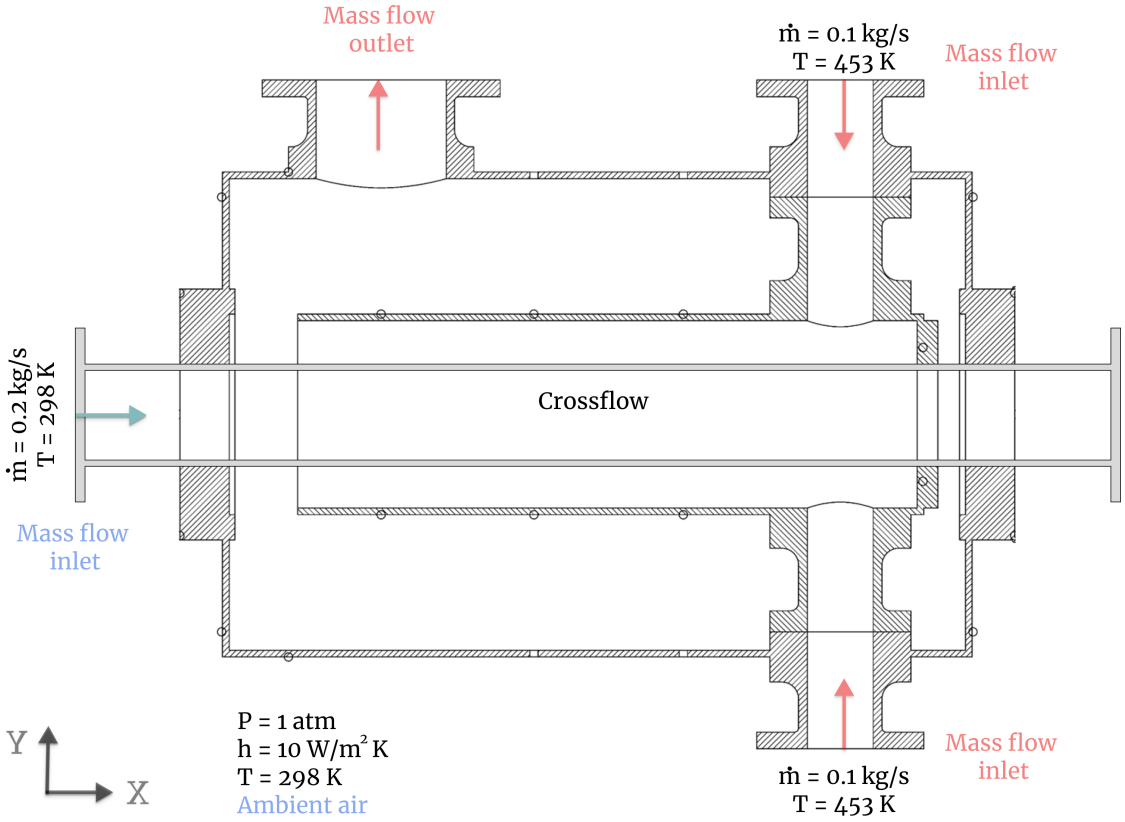


Figure 3.12: Experimental boundary conditions for the steady-state full-load campaign with counter-crossflow inlet at $\dot{m} = 0.2$ kg/s and $T = 453$ K, ambient outer wall condition ($T = 298$ K, $h = 10$ W m^{-2} K^{-1}).

The temperature history of two thermocouples on the inner and outer casings, indicating the steady-state criterion for $dT < 3$ K over a 20-minute interval, is shown in Figure 3.12. The OTCR can replicate cold and warm start-ups where high thermal stresses can be experienced because of the rapid change in solid domain temperature. The temperature change rate is most rapid within the first 30 minutes of a cold start-up. For a warm restart or a ramp-up regime, the time is preconditioned to simulate the frequent and demanding cyclic operations of flexible turbines.

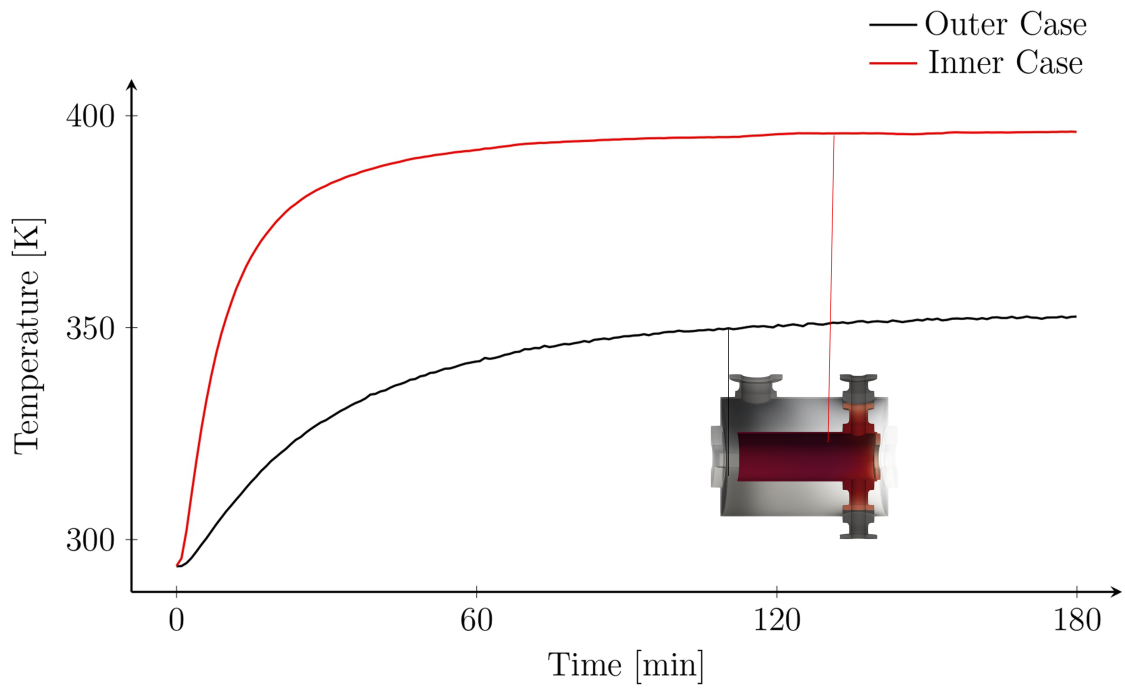


Figure 3.13: Three-hour temperature histories for representative outer and inner casing thermocouples during start-up and approach to steady state ($\dot{m} = 0.2$ kg/s, $T = 453$ K).

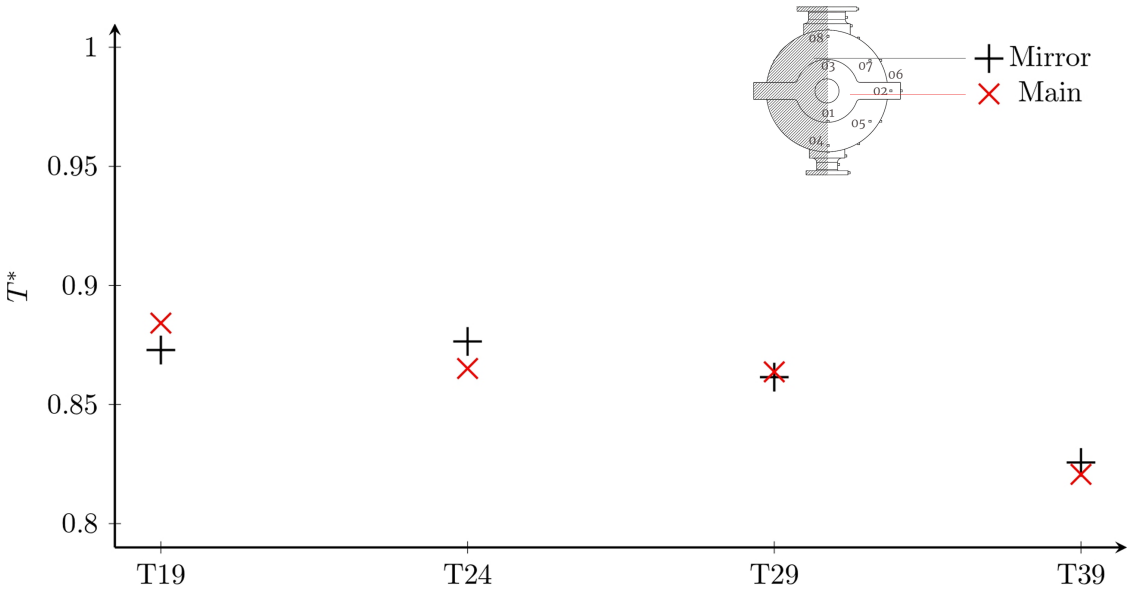


Figure 3.14: Normalised temperature comparison between instrumented and mirror-position thermocouples on the outer casing, illustrating equivalent thermal measurements.

It is instructive to note that the OTCR is axi-symmetric and only half of the casing along the y-plane is fully instrumented on the solid domain to optimise measurement and numerical analysis efficiency, based on similar design models [77].

Table 3.9: Experimental Test Conditions

Variable	Transient shutdown
Hot inlet	-
Cold inlet	-
Ambient temperature	298 K
Inlet mass flow rate	0 kg/s

The experiment assumes a symmetric fluid flow and temperature field. To validate this assumption, four thermocouples are placed at mirror positions on the outer casing and their measurements are recorded and analysed to confirm equivalence, as shown in Figure 3.14.

3.4.1 Transient shutdown

To initiate the transient natural cooling/shutdown, the main path flow is blocked using the flow control valve, as depicted in Figure 3.15, after attaining steady-state. The transient campaign condition is detailed in Table 3.9, indicating the zero mass flow rate and assumed zero heat flux through the inlet and outlet boundaries, replicating the closed valve condition at the onset of the natural cooling shutdown process. While the shutdown process of turbines may be more complex with steam injection, changing flows, vacuuming, and vacuum breaking through the steam ingestion processes and cooling that may take up to 100 hours [78], this test campaign is set to ensure applicability with the numerical model, allowing for validation processes through control experiments. This experiment is designed to validate conjugate fluid-solid models, including those involving transition flows and complex thermal fields.

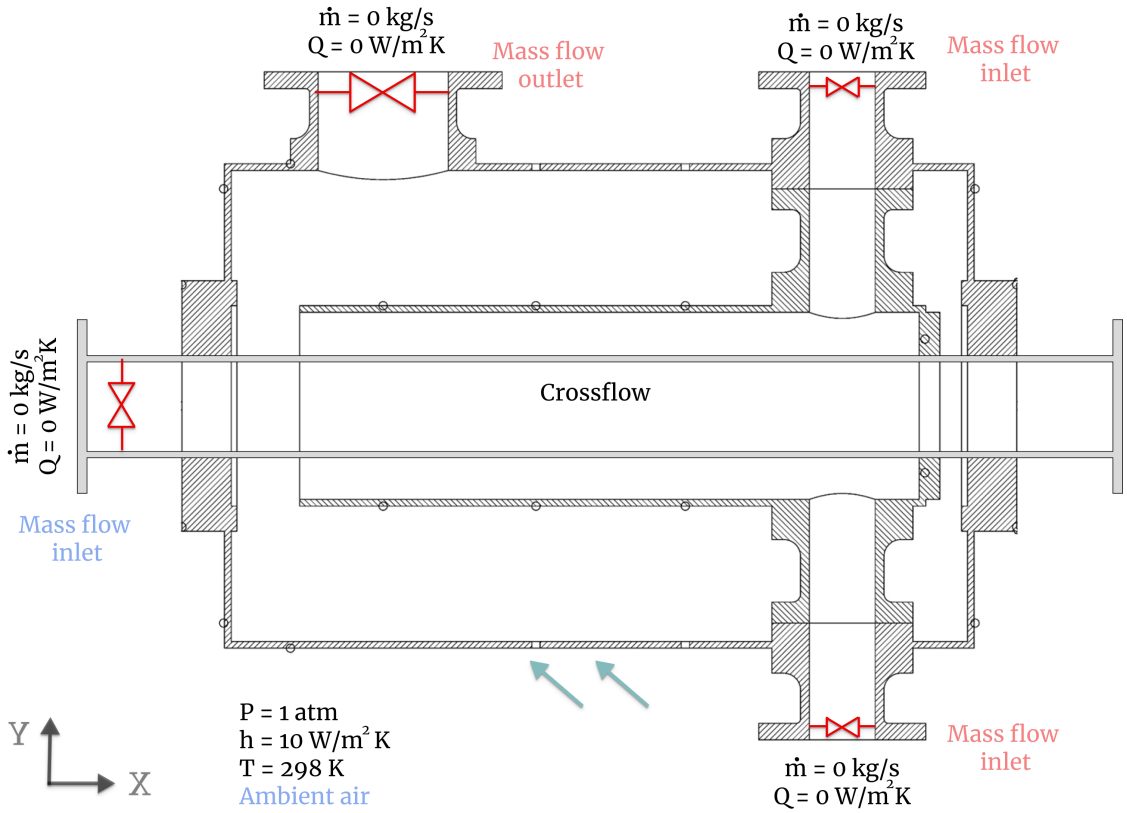


Figure 3.15: Shutdown experimental setup conditions indicating the boundary conditions and experimental configuration for the transient natural shutdown regime.

During the shutdown process, casing temperatures are recorded with a 10-Hz sampling frequency for the natural cooling duration. Figure 3.16 is a depiction of the transient natural cooling curves for two selected thermocouples on the outer and inner casing. Further analysis of the cooling thermal field is detailed in the next chapters. The shutdown and steady-state modes can be modified to demonstrate other experimental regimes, such as warm restart and rapid start-stop cycles. Note also that the turbine has yet to be insulated on the surface to allow for the future installation of active and optimisable heater patches that will discretise the turbine casing and transform it from a basic structural component to a controllable component to obtain the desired thermal fields. This lack of insulation adds to experimental uncertainty.

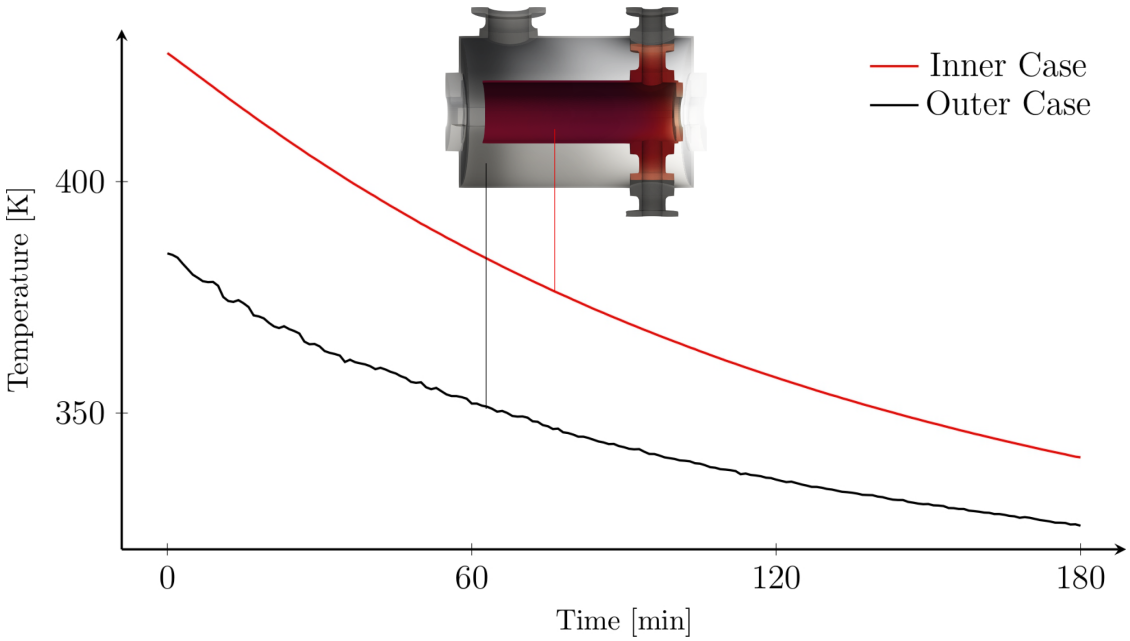


Figure 3.16: Three-hour temperature decay histories for representative outer and inner casing thermocouples during transient natural cooling post-shutdown, initiated from steady-state full-load conditions.

3.5 Uncertainties

Table 3.10 summarises the uncertainties of the measured variables for the OTCR, including positional uncertainty from the placement of thermocouples on the casing surface. The fluid flow effect on thermocouple readings could impact temperature measurements. However, thermocouples are installed on the casing surface with thermally insulating tapes to ensure firm thermal contact between the thermocouple and the solid, thereby minimising fluid heat transfer effects and this uncertainty. Other uncertainty concerns include the thermal boundary condition on the outer casing, which could be mitigated by insulating the surface to ensure predictability. Uncertainties could equally arise from the assumption of symmetry in the thermal field and flow field. The thermal field symmetry has been measured to be 3%, and the assumption remains viable. Variables like the inlet temperature are directly related to the thermocouple uncertainty in the fluid measurement at the inlet.

Table 3.10: Experimental Uncertainties

Variable	Uncertainty
Solid temperature	± 3 K
Fluid temperature	± 0.5 K
Mass flow rate	± 3%
Traverse position	± 0.05 mm
Thermocouple position	± 0.5 mm

3.6 Summary

The Oxford Turbine Casing Rig (OTCR) is presented. The facility design involves an iterative preliminary simulation process that replicates thermal fields and characteristics similar to those of MHI turbines. The operating range, from forced to mixed and natural convection flows in the intricate turbine cavity, further provides dependability of the data to be transferred from the test facility to real turbines, based on MHI's dimensionless numbers range. The OTCR is instrumented to measure solid and fluid thermal fields.

Experimental campaigns, including steady-state full-load and transient natural shutdown processes, are conducted with the OTCR to evaluate its design conformity for future validation and test exercises. The experimental conditions are designed within the operating range of dimensionless numbers based on MHI-provided data. At the full-load steady-state operating point of $\dot{m} = 0.2$ kg/s, the cavity flow is characterised by $\mathrm{Re} = 3.4 \times 10^3$ and $\mathrm{Ri} = 3$, corresponding to mixed convection dominance. During transient natural shutdown with zero mass flow, $\mathrm{Re} = 6.8 \times 10^1$ and $\mathrm{Ri} = 5 \times 10^3$, corresponding to natural convection dominance.

4

Hybrid Steady-State and Transient Numerical Analysis and Physical Measurements

For the OTCR platform facility introduced, this chapter presents a numerical analysis of the thermal fields in the solid and fluid domains. Steady-state and transient analysis are performed using hybrid fidelity methodologies, essential for optimising and controlling thermal fields. Two thermal field analysis approaches are utilised. High-fidelity numerical analysis using the commercially available solver *Ansys Fluent* 2023 R1 has been conducted, and the results are compared with physical measurements. These high-fidelity results and physical measurements are used to support the development and validation of novel Thermal Network Models for fast turbine thermal analysis. This hybrid methodology is demonstrated to enable real-time analysis of thermal fields.

Numerical analysis sets the basis for utilising the novel OTCR in developing optimisation tools for turbine casing thermal field control. It further demonstrates the ability to use the facility to validate turbine analysis tools and models.

4.1 High-fidelity Numerical Analysis

Steady-state and transient shutdown numerical analysis is performed on OTCR using the high-fidelity CHT methodology in *Ansys Fluent 2023 R1* environment to evaluate thermal and flow fields. Compared to the OTCR detailed design geometry, less significant features such as traverse mount supports, traverse holes, and bolts are defeatured for computational efficiency. This efficiency step was critical to enable convergence within the computational resources available. It is noted that these features are accounted for as uncertainties, and steps are taken in the experimental setup to minimise the uncertainty introduced by the model efficiency. The traverse holes on the outer casing are sealed with thermally insulating tapes before physical measurements are taken. In contrast, core design features such as the thickness of the flange, fillets, and the shape of the casing barrel were modelled. These features have the most significant thermal design implications on the OTCR. The flanges enable the capturing of the gradient and are core features of real turbines. Other core components, such as the inlet, outlet, and shaft, with their varying thicknesses, are maintained consistently with the rig geometry.

A non-conformal tetrahedral mesh was used to enable inflation layers between the solid-fluid interface, as shown in Figure 4.1. The computational domain comprises the solid domain (inner case, outer case, and shaft) and the fluid domain (hot fluid and crossflow cold fluid). The solid and fluid domains are coupled for the numerical analysis. Flow velocities range from near 0.1 m/s in the natural convection shutdown regime to 35 m/s at the inlet section at full-load forced convection ($\dot{m} = 0.2$ kg/s). This wide range of flow conditions necessitates inflation layers to accurately resolve the near-wall viscous sublayer across all regimes. Equation 4.1 defines the wall dimensionless distance and Equation 4.2 determines the first inflation layer thickness [79, 80]. The wall y^+ ranges from 0.6 to 0.9 with smooth cell growth to meet the wall treatment and convergence criteria. The mesh comprises 1.1×10^6 nodes and 2.6×10^6 elements.

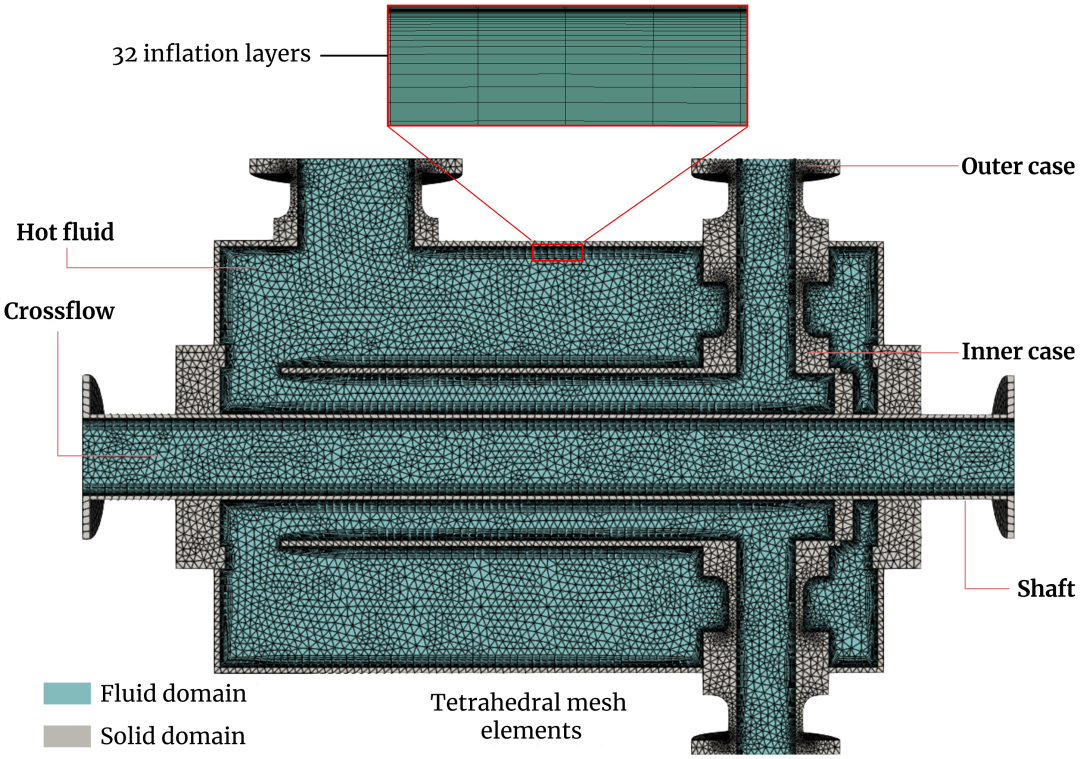


Figure 4.1: Symmetry-plane view of the multi-domain CHT mesh comprising solid domains (outer casing, inner casing, shaft) and fluid domains (hot and cold), with inflation layers at solid-fluid interfaces.

$$y^+ = \frac{\rho y}{\mu}\sqrt{\frac{\tau_w}{\rho}} \leq 1 \tag{4.1}$$

$$\tau_w = \frac{1}{2}C_f \rho v_\infty^2, \quad C_f = 0.058\, Re^{-0.2}, \quad \Delta y = \frac{y^+ \mu}{v_\tau \rho} \tag{4.2}$$

The Reynolds–averaged Navier–Stokes (RANS) k–ω SST viscous turbulence model simulates the CHT between mixed flow fluids and solids. It is governed by the energy equation 4.3, which equates the rate of change in energy in the volume and the energy expelled through convection to the sum of the energy transport into the volume comprising the conductive terms and the viscous dissipation due to high-speed flows. The density is set on the basis of ideal gas laws. This model is suitable for analysing the thermal fields in the solid and fluid domains. Conductive models that resolve heat conduction equations are used within the solid domain. The fluid-solid coupling balances the heat flux at the fluid-solid interface.

$$\frac{\partial}{\partial t}(\rho E) + \nabla \cdot [\vec{v}(\rho E + p)] = \nabla \cdot \left[k_{eff} \nabla T - \sum_j h_j \vec{J}_j + (\bar{\bar{\tau}}_{eff} \cdot \vec{v}) \right] \tag{4.3}$$

The solid properties are equivalent to the rig properties in Table 4.1. These are properties closest to the material properties of the turbine casing of MHI, but which are not replicable due to intellectual property protection. With its similarity to the properties of real turbines, the numerical analysis results are transferable to real turbines. The fluid properties are defined in Table 4.2. The OTCR uses air as the working fluid, whose properties differ from those of steam in typical steam turbines, most notably in the Prandtl number ($\mathrm{Pr}_{\mathrm{air}} = 0.72$ versus $\mathrm{Pr}_{\mathrm{steam}} \approx 1$ [66]). A higher Prandtl number in steam produces a thinner thermal boundary layer relative to the velocity boundary layer, resulting in higher near-wall temperature gradients than those measured in the OTCR. However, rig design with comparable dimensionless numbers in the fluid cavity enables the transferability of results between OTCR and conventional turbines. The boundary conditions are illustrated in Figure 4.2, where the surrounding air is ambient, and the inlet air is mass flow regulated at 453 K. The surrounding temperature during the experiment defines the outer wall boundary condition. Because the experimental facility's surroundings experienced minimal airflow with no forced convection, natural convection governs the outer wall heat transfer. The Churchill and Chu correlation for natural convection over a horizontal cylinder [66], is used to estimate an HTC range of 5 to 7 $\mathrm{W\,m^{-2}\,K^{-1}}$ across the OTCR operating conditions. A conservative upper-bound value of 10 $\mathrm{W\,m^{-2}\,K^{-1}}$ is adopted for the outer wall boundary condition. The steady-state convergence criteria comprises an energy residual of 1×10^{-6} and continuity, momentum, and turbulence residuals of 1×10^{-3}. The simulation converged after 452 iterations, with all residuals satisfying these criteria and ensuring the overall stability of the solution.

Hybrid transient cooling analyses for the defined operating point is also configured with Unsteady RANS (URANS) with $k - \omega$ SST Simple Gradient Diffusion Hypothesis (SGDH) turbulence model [30], for the post-shutdown natural cooling. High-fidelity CHT loosely couples the solid and fluid domains based on the method developed in [81], using a 0.1-second time step over a 1-hour duration (36,000

Table 4.1: Numerical analysis solid material Properties

Component	ρ [kg/m^3]	k [W/m.K]	C_p [J/kg.K]
Outer case	7850	47.6	500
Inner case	7850	47.6	500
Shaft	7850	47.6	500

Table 4.2: Numerical analysis fluid Properties [66]

ρ [kg/ m^3]	μ [kg/m.s]	k [W/m.K]	C_p [J/kg.K]	Pr [-]
1.225	1.789×10^{-5}	0.025	1006	0.72

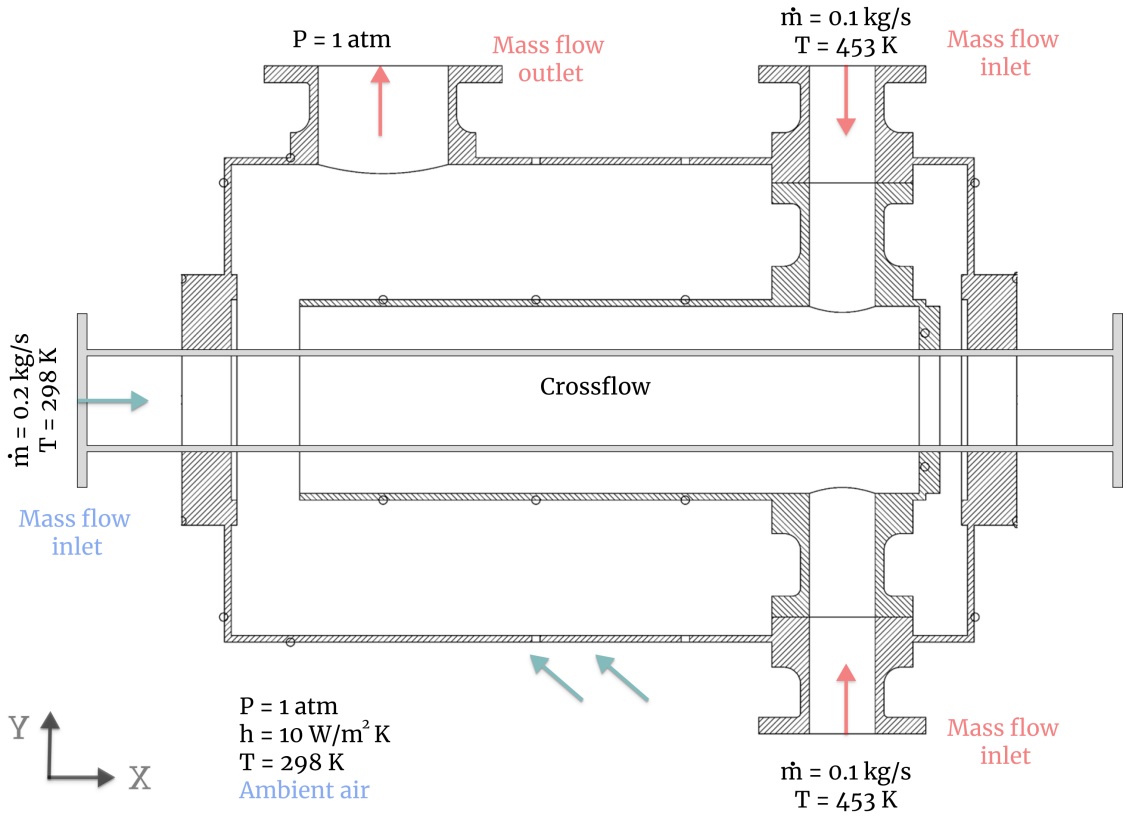


Figure 4.2: Boundary conditions applied to the CHT numerical model, comprising the hot and cold inlets and ambient conditions for the OTCR.

timesteps) with 500 iterations per time step and the same residuals as the steady-state simulations while maintaining solution stability. The solution fields are recorded with a 10-minute periodicity.

4.2 High-fidelity CHT results

4.2.1 Fluid domain contours

The high-fidelity numerical analysis results are presented. Figure 4.3 shows the normalised velocity $v^* = v/V_{\max}$, where $V_{\max} = 35$ m/s is the maximum velocity at the inlet at full-load conditions ($\dot{m} = 0.2$ kg/s). The three cross-sections illustrate the variation of the complex flows within the cavity. The flows range from forced to mixed and recirculating flows, forming complex patterns that characterise steam turbine cavity physics.

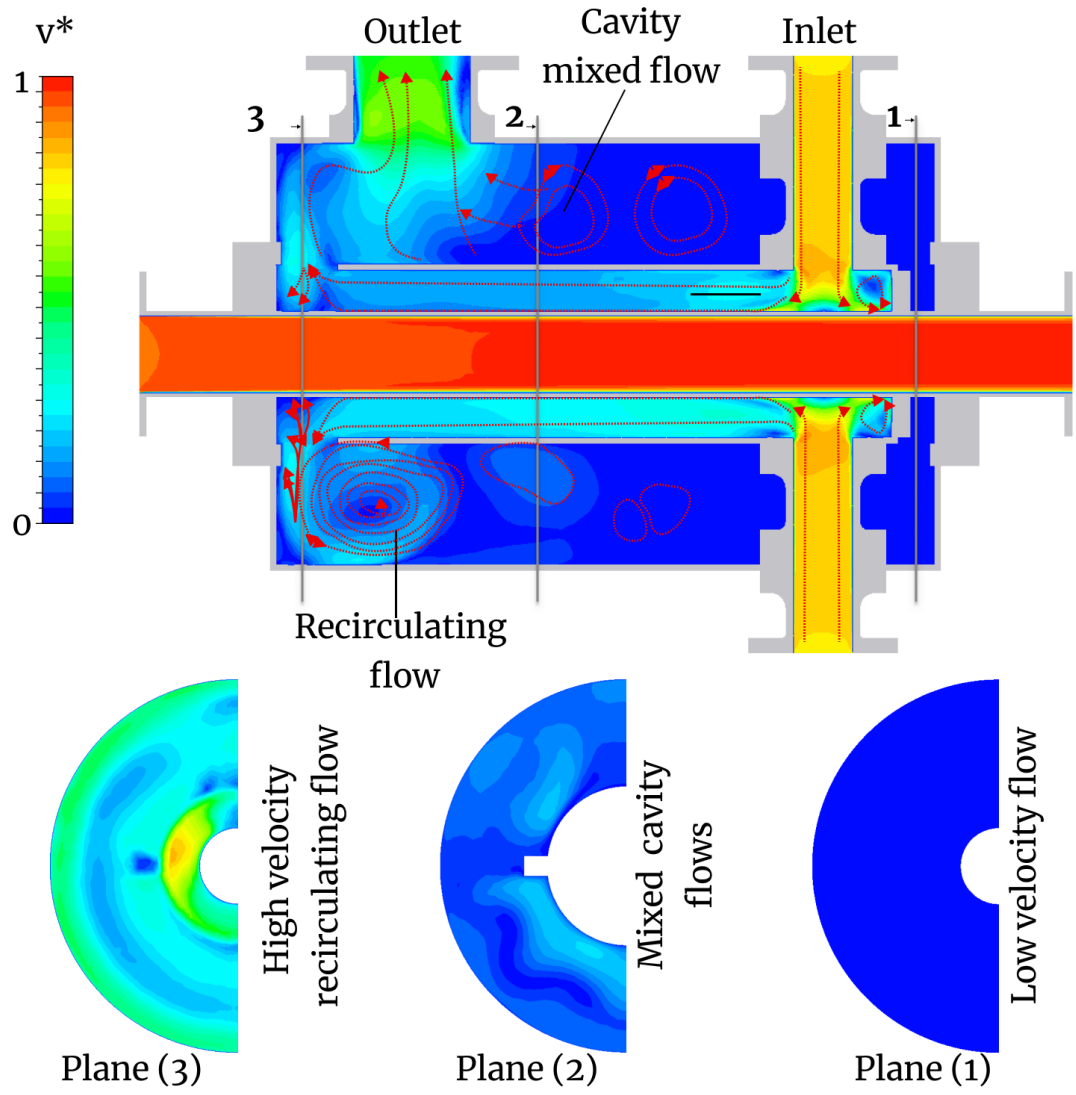


Figure 4.3: Steady-state fluid velocity contours with three axial cross-sections of the OTCR cavity, revealing forced convection in the main flow path and recirculating mixed-convection flows in the annular cavity that drive non-uniform casing heat transfer.

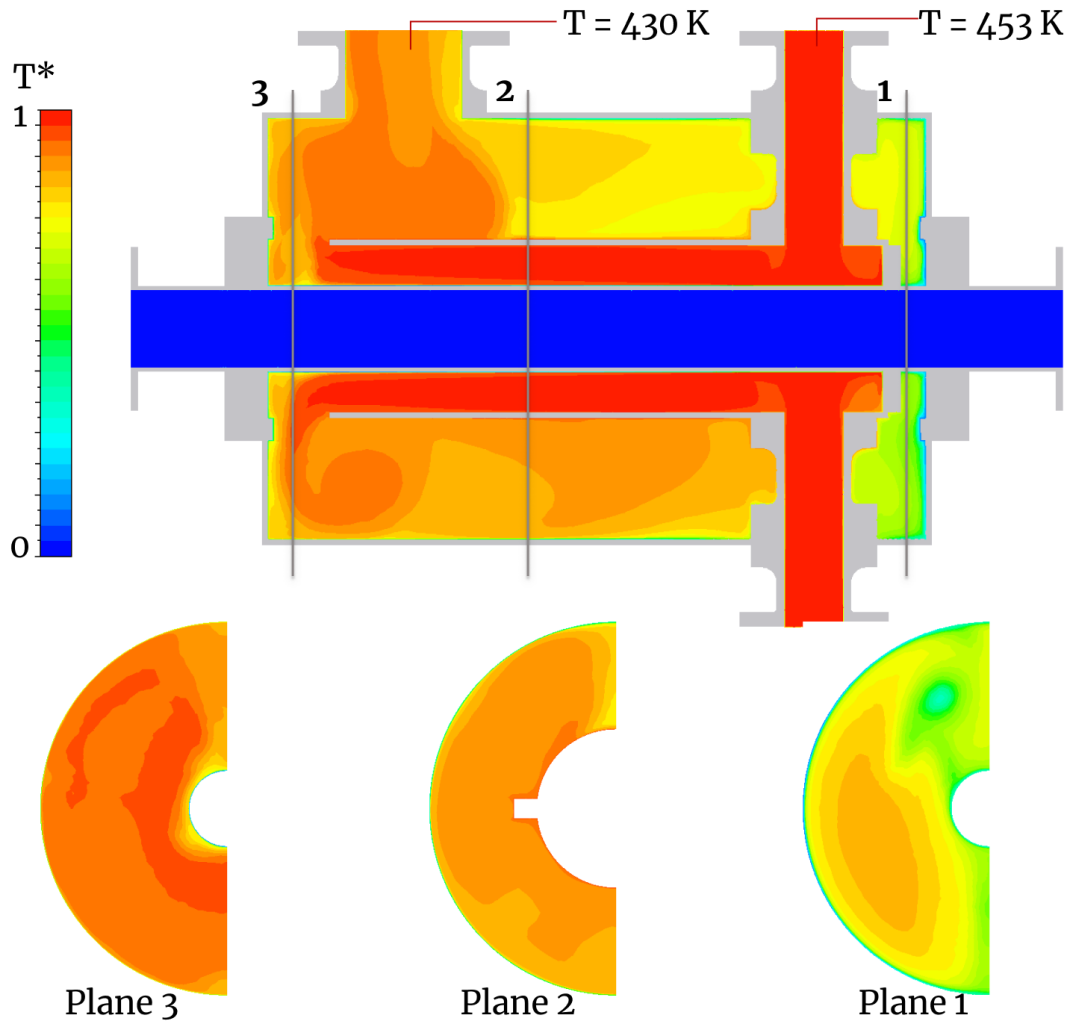


Figure 4.4: Steady-state fluid temperature contours at three axial cross-sections, showing the influence of cavity recirculation on the local fluid temperature field and its coupling to the casing solid domain.

Figure 4.4 illustrates the fluid temperature contours. The inlet and outlet temperatures of 453 K and 430 K provide some temperature difference for conductive heat flux along the casing. The various cut planes indicate different temperature fields, with the inlet regions and the flow path in the inner casing showing the highest temperatures. Together with the end plate on plane (1), which shows the least temperature field, the temperature distribution causes a conductive heat flux throughout the casing. The shaft design supports a rotor-bladed path, improving the convective area and thermal mass. It will boost heat exchange, replicate the windage heating effect, enhance thermal inertia, and model higher thermal

conductive heat flux and casing thermal stresses. The flow pattern affects localised fluid characteristics, such as the boundary layer thickness and Grashof and Prandtl numbers, which influence convective heat transfer between the working fluid and the casing. These characterising quantities were considered in the pre-design to ensure that the OTCR is viable for turbine thermal field tests. These interactions, the casing material properties, and the experimental conditions determine the casing thermal field.

4.2.2 Solid domain temperature field

This section presents steady-state solid temperature field contours resulting from the high-fidelity numerical analysis of the CHT between the fluid and solid domains of the OTCR. Figure 4.5 shows the thermal field of the outer casing with high thermal gradients along and across the flanges and thick-walled regions, and less gradient in thinner regions [82]. The non-uniformity between the thick and thin sections creates different heat flow contours, impacting the temperature field. Thicker sections have higher thermal resistance and Biot number, influencing the conductive-convective heat-transfer interactions. The inlet region and outlet have higher temperatures due to the energy exchange between the fluid and solid. The barrel in the cavity region exhibits lower temperatures, although with defined contours. These temperature contours are interconnected with conductive heat flux, and the convective heat transfer between the intricate fluid flow and solid in the cavities.

Figure 4.6 illustrates the temperature field of the inner casing. In this case, the barrels' near-uniform temperature deviates from a typical turbine thermal field due to the lack of a bladed path that facilitates thermal energy and work to redefine the thermal fields. The thermal properties of the solid and the characteristics of the surrounding fluid flow determine the temperature distribution. Geometric simplifications affect the results compared to actual turbines. However, the validation for test cases and operations is based on the OTCR geometry test improved complexity levels to numerical analysis models.

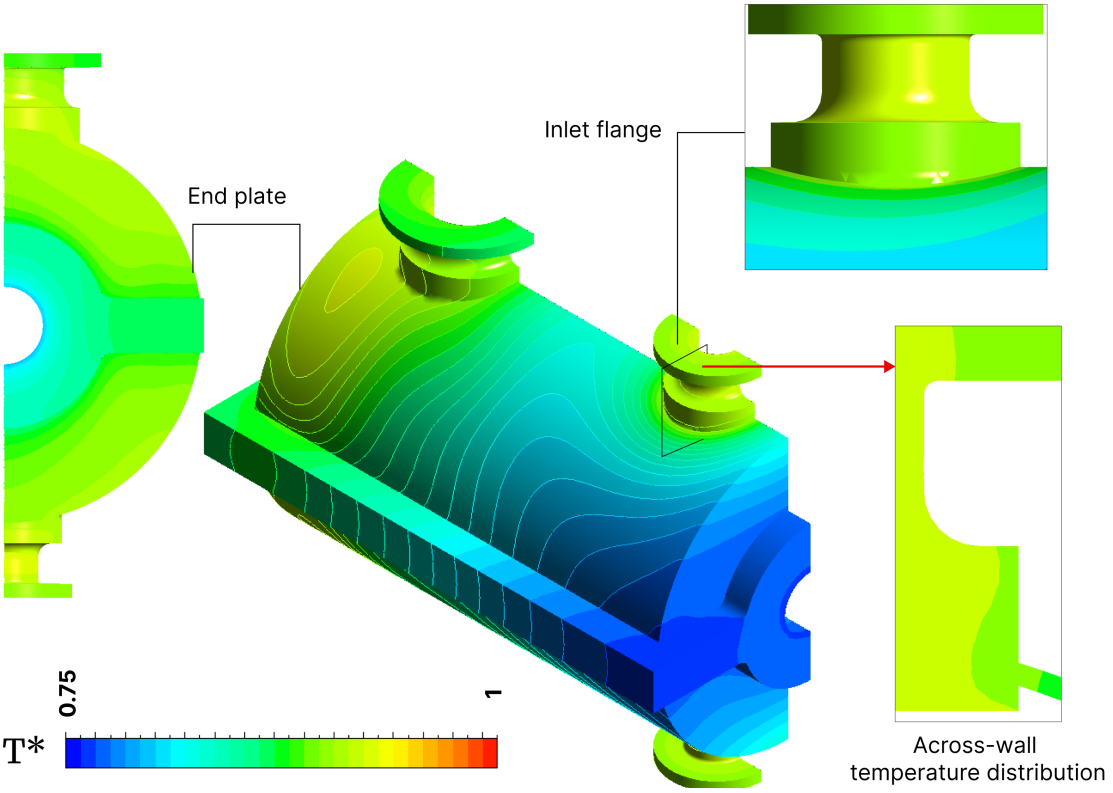


Figure 4.5: Steady-state temperature contours of the OTCR outer casing at full-load conditions ($\dot{m} = 0.2$ kg/s, $T_{in} = 453$ K, $T_{\infty} = 298$ K), highlighting high thermal gradient regions at the inlet interface and thick-walled flange sections.

4.2.3 Result Validation

Numerical analysis and physical measurement results are available in the supplementary repository [83]. Figures 4.7 and 4.8 show the results of the outer casing thermocouples in planes A-I. Temperatures are normalised and defined by $T^* = T/T\,\mathrm{max}$, where $T\,\mathrm{max}$ is 453 K (inlet temperature boundary condition). Table 4.3 shows the difference between the physical temperature measurements from the thermocouples and the corresponding numerical analysis averaged across the planes. Normalised temperatures from the physical measurements and numerical analysis are equivalent, validating the accuracy of the OTCR design and highlighting its value in developing further models. Like in the thermal field contour plot, Planes A, B, C, and D are generally hotter than the planes H and I due to the fluid flow patterns. Note the steep temperature profile in plane G resulting from the steep temperature change between the inlet flanges and the turbine barrel, resulting in a

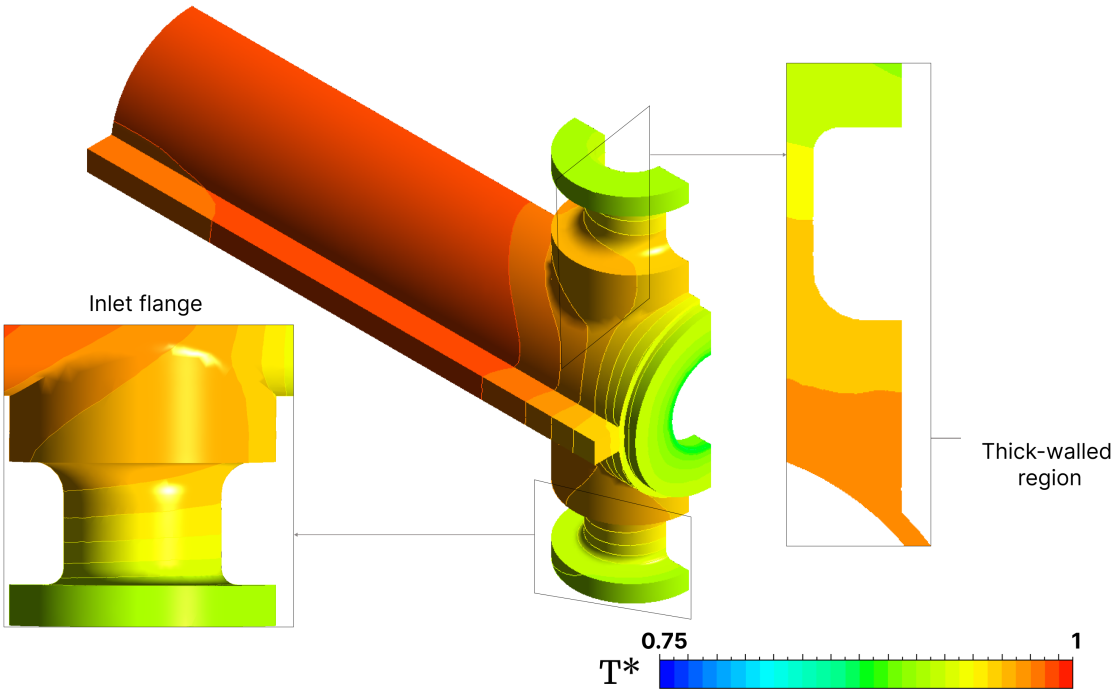


Figure 4.6: Steady-state temperature contours of the OTCR inner casing under full-load conditions ($\dot{m} = 0.2$ kg/s, $T_{in} = 453$ K, $T_{\infty} = 298$ K). The casing shows a higher temperature gradient along the inlet region and a near-uniform temperature distribution in the thin-walled barrel region due to the absence of a bladed path.

steep thermal gradient. This region will be of specific interest in the analysis to decrease the turbine thermal gradient, as will be discussed later.

Table 4.3: Overview of Outer Case Temperature Measurements: Percentage Difference Between CHT Simulation and Experimental Results is calculated as [CHT − Experiment] [%], averaged across all circumferential thermocouple positions within each plane.

Plane	X distance [mm]	[CHT-Experiment] [%]
A	0	1.83
B	50	2.22
C	130	2.65
D	241	2.08
E	424	0.94
F	603	1.52
G	786	3.14
H	950	1.30
I	1000	0.73

Table 4.4: Overview of Inner Case Temperature Measurements: Percentage Difference Between CHT Simulation and Experimental Results is calculated as [CHT − Experiment] [%], averaged across all circumferential thermocouple positions within each plane.

Plane	X distance [mm]	[CHT-Experiment] [%]
A_i	241	1.48
B_i	424	1.83
C_i	603	1.79
D_i	786	1.16
E_i	890	2.16

The inner casing thermocouples in 5 axial planes, A_i-E_i, are shown in Figure 4.9. Table 4.4 summarises the locations and measurement differences on all inner case measurement planes between numerical analysis and physical measurement across all planes. The inner case is hotter than the outer case due to increased heat energy exchange between the inner casing and fluid. Note that thermocouples with lower temperature values than the adjacent thermocouples tend to be in wall regions with increased thickness and thermal resistance. The facility enables further improvements, such as modelling thermal radiative effects and localised heat transfer coefficients, and refining ambient air boundary conditions to enhance result accuracy.

4.2.4 Fluid cavity temperature validation

Normalised traverse thermocouple measurements and CHT results are shown in Figure 4.10. Table 4.5 summarises the locations and polar angles of the traverse θ in the horizontal x-direction. It shows less than 3% the temperature difference between the CHT and the experimental measurements. For traverses 2 and 4 placed at $\theta = 90^0$, the results show a detailed capture of the thermal characteristics and thermal boundary effect. These regions have a fully formed mixed flow that is significant in the analysis objectives of this facility. For Traverses 1 and 3, unlike the CHT, the physical measurement captures the near-wall thermal effect, stressing the importance of the OTCR to tune numerical tools. This result highlights the validity of the OTCR in developing and testing new models. As identified in the literature [30], the resolution of normal and perpendicular thermal and flow fields

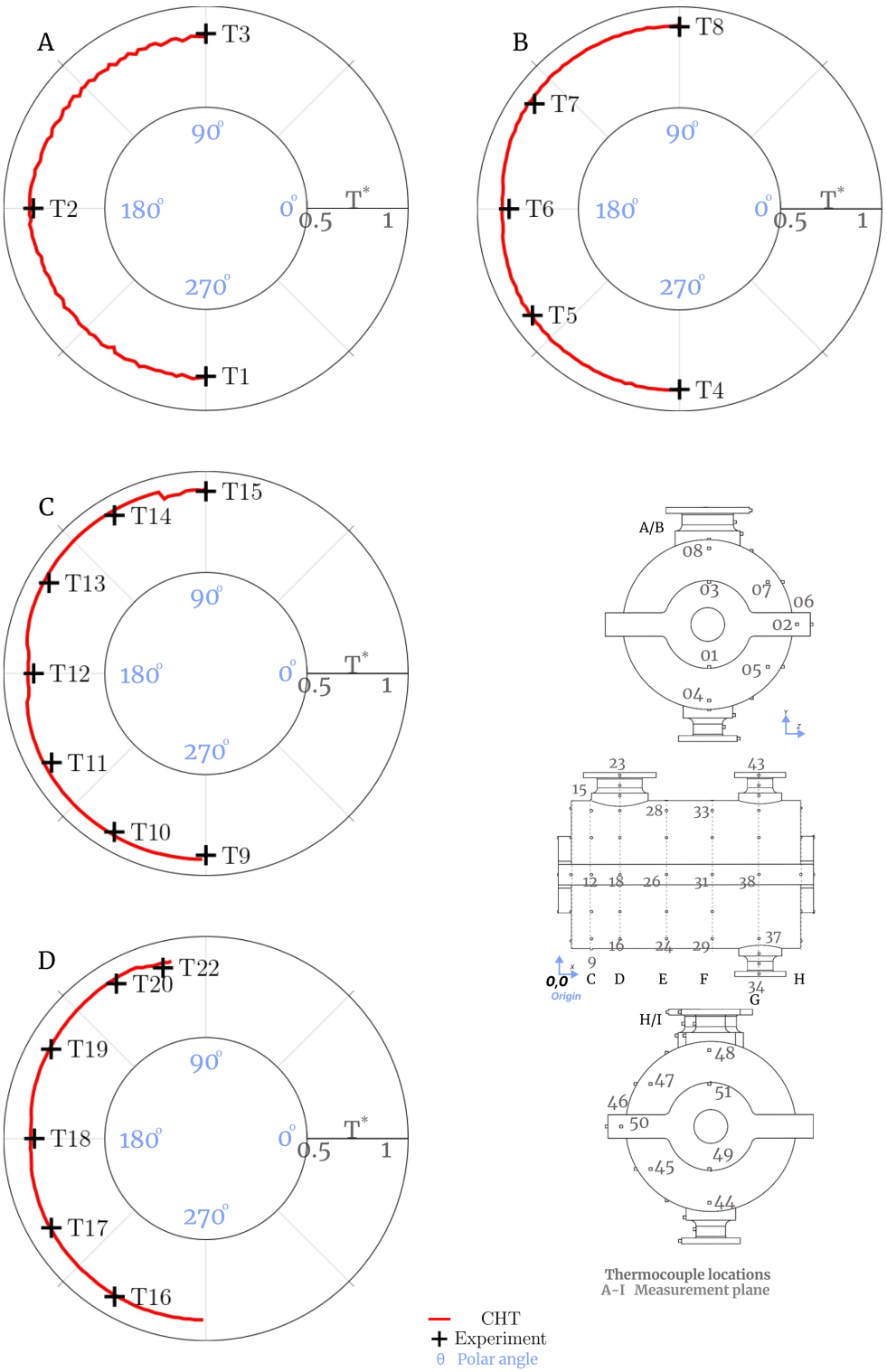


Figure 4.7: Polar plots of normalised outer casing temperature $T^* = T/T_{\max}$ at planes A–D, comparing CHT predictions with thermocouple measurements at steady-state full-load conditions ($\dot{m} = 0.2$ kg/s, $T_{in} = 453$ K, $T_\infty = 298$ K)

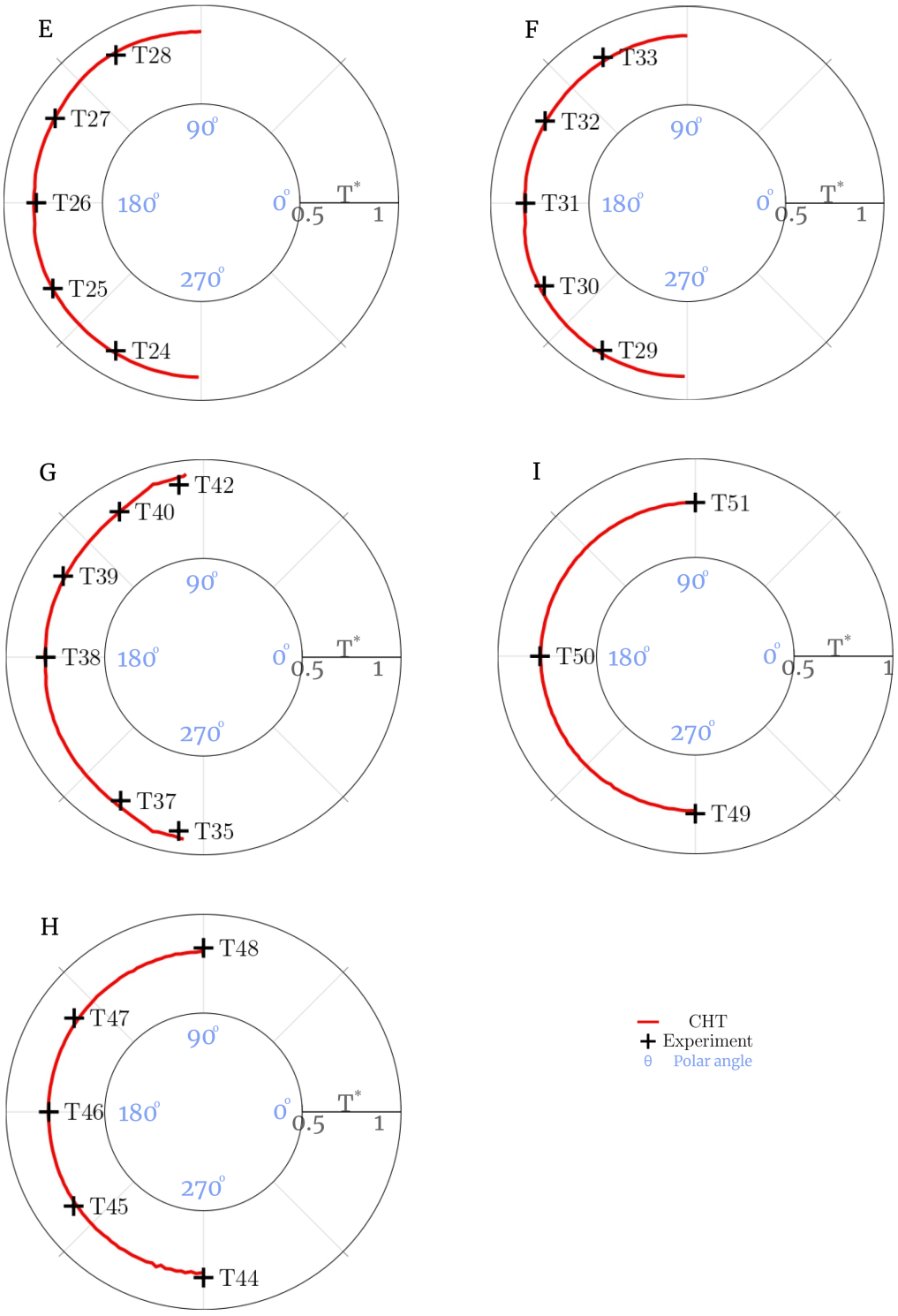


Figure 4.8: Polar plots of normalised outer casing temperature $T^* = T/T_{\max}$ at planes E–I, comparing CHT predictions with thermocouple measurements at steady-state full-load conditions ($\dot{m} = 0.2$ kg/s, $T_{in} = 453$ K, $T_\infty = 298$ K).

in complex turbine cavities is computationally challenging, leading to accuracy concerns. Having a real facility that is accessible for testing novel models that could address these numerical challenges is therefore critical. Even conventional models may need revalidation in such critical conditions where previous tests have not been very robust. These models may require improved tuning of thermal field components for improved accuracy. The OTCR provides data to validate these models and increase confidence in testing new turbine analytic tools and models.

Table 4.5: Traverse fluid temperature measurements: percentage difference between CHT predictions and experimental traverse thermocouple measurements, calculated as [CHT − Experiment] [%] [84].

Traverse	X distance [mm]	θ^0	[CHT-Experiment] [%]
Tr1	241	225	0.76
Tr2	424	90	1.25
TR3	603	135	2.02
TR4	603	90	0.50

4.2.5 Post shut-down natural cooling

Figure 4.11 illustrates the transient natural cooling shutdown with the shutdown natural cooling operating point described in Section 3.4.1. It presents normalised temperature decay over 120 minutes for thermocouples T3, T16, and T29, alongside thermal field contours at 20, 40, and 60 minutes. These casing measurement locations exhibit varying thicknesses and different local Fourier numbers $\text{Fo} = \alpha t/L^2$, where L is the local wall thickness. Greater wall thicknesses correspond to lower Fourier numbers, slower approaches to thermal equilibrium, and reduced cooling rates [66]. The Reynolds number varies across locations due to differences in geometry and flow velocity, influencing convective heat transfer during cooling. The unsteady CHT simulation predicts general temperature decay compared to experimental measurements with less than 5% difference ([CHT-Experiment] [%]) across validated points. The simulation uses a simplified time step, and the Simple Gradient Diffusion Hypothesis turbulence model is used for commercial Ansys Fluent. The location T3, a vertical wall section of the endplate, shows the best agreement between

the measured and calculated values. T16 and 29 show more discrepancies, which could be attributed to the model's inadequate resolution of the normal and parallel heat flux components. It requires specialised boundary layers and turbulent model treatment. Hence, a more advanced turbulence model must be employed to better resolve wall heat flux and to define characteristic length and time-step size over long natural cooling durations to enhance result accuracy [30]. OTCR validation data enable this more complex transient analysis, addressing the transient model bottleneck for advancing turbine models.

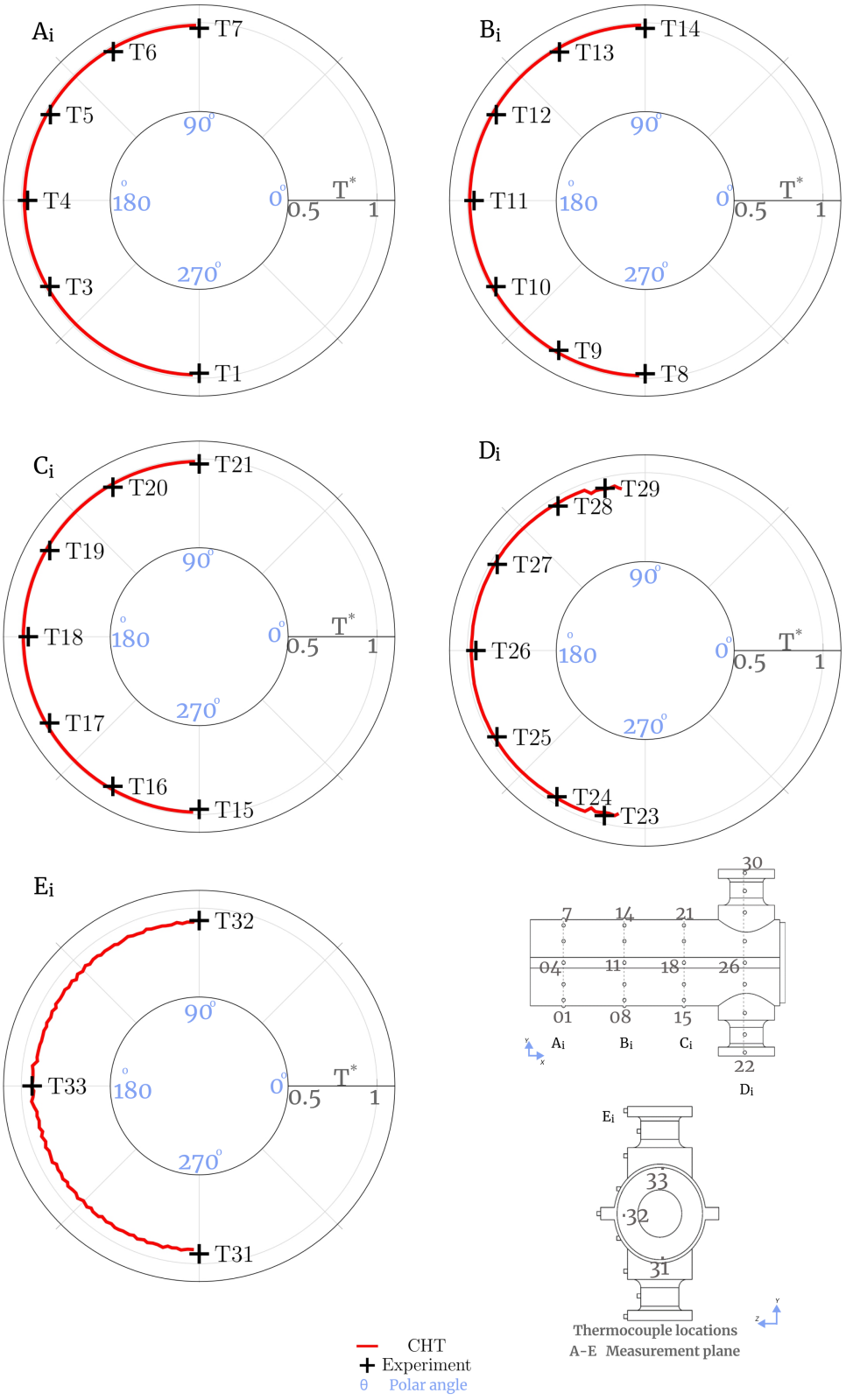


Figure 4.9: Polar plots of normalised inner casing temperature $T^* = T/T_{\max}$ at planes A_i–E_i, comparing CHT predictions with thermocouple measurements at steady-state full-load conditions ($\dot{m} = 0.2$ kg/s, $T_{in} = 453$ K, $T_\infty = 298$ K).

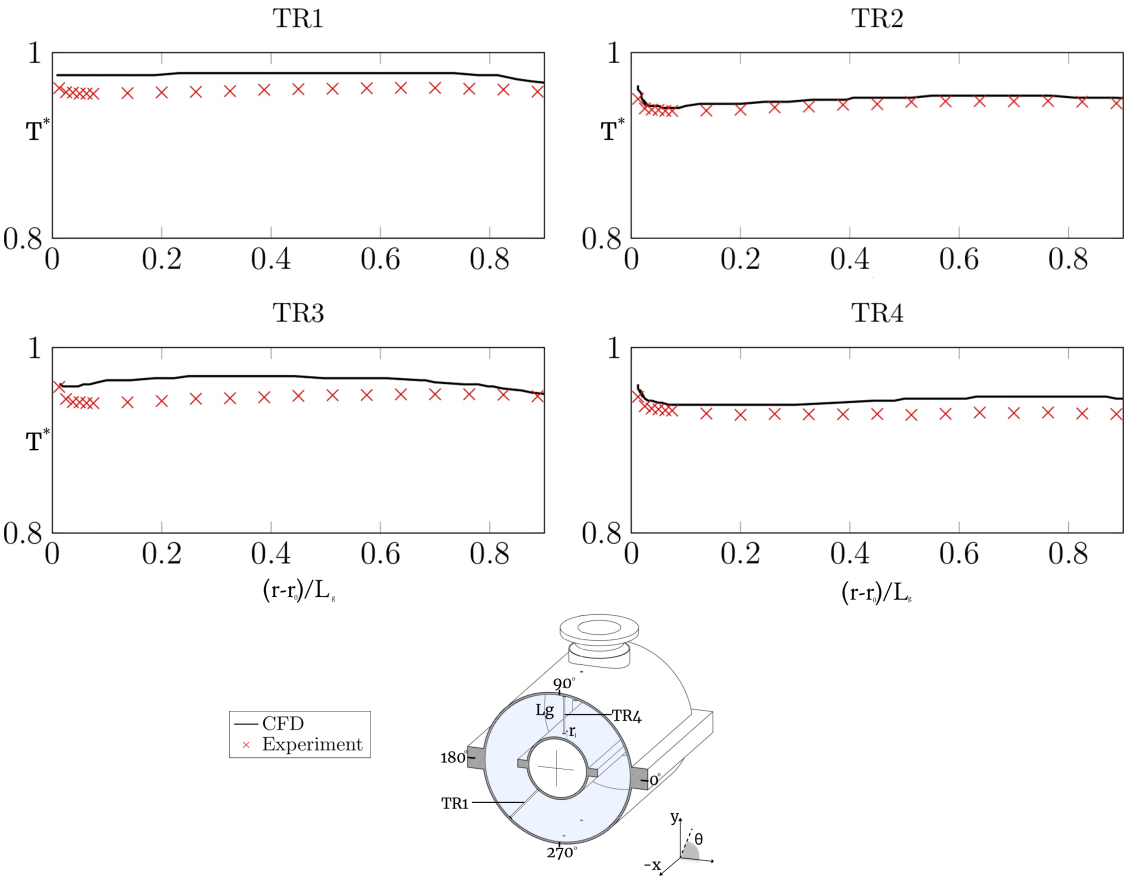


Figure 4.10: Normalised traverse fluid temperature profiles $T^* = T/T_{\max}$ at four cavity locations (Tr1–Tr4), comparing CHT predictions with thermocouple measurements at steady-state full-load conditions ($\dot{m} = 0.2$ kg/s, $T_{in} = 453$ K, $T_\infty = 298$ K, revealing the near-wall thermal boundary layer structure and mixed-convection cavity behaviour.

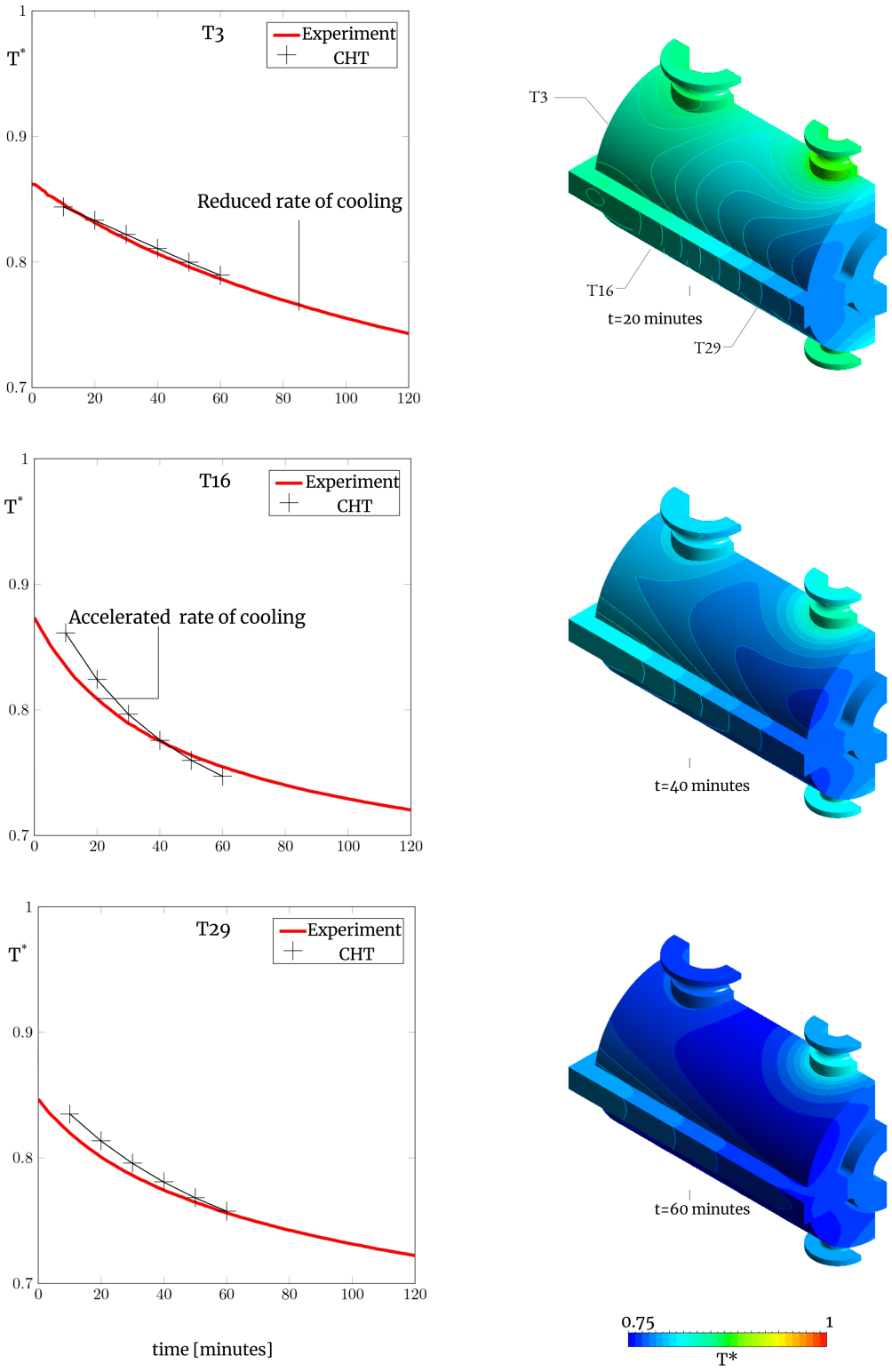


Figure 4.11: Post-shutdown natural cooling showing transient temperature decay at thermocouples T3, T16, and T29, comparing CHT predictions with physical measurements. Initial condition: steady-state full-load ($\dot{m} = 0.2$ kg/s, $T_{in} = 453$ K). Shutdown condition: zero mass flow ($\dot{m} = 0$ kg/s), $T_\infty = 298$ K, Temperature field contours shown at $t = 20$, 40, and 60 min.

4.3 Novel Numerical Tools for Thermal Field Analysis and Optimisation

Because of the complexity of thermal fields, evolving through multi-domains spatially and temporally, fast multi-fidelity thermal field analysis is required for real-time optimisation and control methodologies [24]. Due to the sparsity of live plant measurements, they must be supplemented with high-fidelity analysis for thermal field resolution. High-fidelity numerical analysis, while accurate, is computationally demanding and unfeasible for real-time control. Data downsampling methods and data transfer between high- and low-fidelity analysis are required to adequately monitor plant fields. Hybrid methodology, utilising plant data and numerical analysis, is crucial because it overcomes the limitation of the sparsity of physical measurements and the computational cost of high-fidelity numerical analysis for real-time control. While some new methodologies for fast thermal analysis have been proposed as detailed in Section 2.4, they are developed based on localised plant components, focus on a few validation points, and are largely unvalidated by physical measurements [59].

For the requirements of this thesis, this section utilises the OTCR for validating complex thermal field analysis. The OTCR can be used to evaluate multiple numerical models, providing a unique validation and calibration dataset alongside a hybrid thermal analysis toolset to enable real-time prediction of turbine thermal fields. A newly developed Thermal Network Model (TNM) and a transient natural cooling approach are validated using the OTCR for improved computational efficiency.

4.3.1 TNM setup

A hybrid model methodology is implemented based on the real turbine operating conditions described above. The Thermal Network Model (TNM), as detailed in [24] with the electrical equivalent of thermal circuits, is configured to analyse the solid and fluid thermal fields of the OTCR. The methodology applies Kirchhoff's current law (KCL) with heat flux as the corollary of current and temperature as the equivalent of voltage, resulting in a zero summation of heat flux at any node [85,

86]. Figure 4.12A illustrates the 1D equivalent of thermal circuits. The TNM reads the mesh file created in ICEM and extracts the cell information, including the area, volume, and connectivity, to determine the resistances of the cells. It uses material properties to determine the capacitance of the cells. Each mesh volume has a capacitance, and a resistance is assigned to each connection, resulting in two series resistances between two cell centroids. Solid-fluid multi-zone analysis with mixed material properties and boundary types is achieved by decoupling the solid and fluid components with different equivalent capacitance and conductive and convective resistances with a heat transfer mask for each circuit path, which can be activated for a cell as shown in Figure 4.12B to enable consistent vector sizes across multi-zone matrix analysis [24].

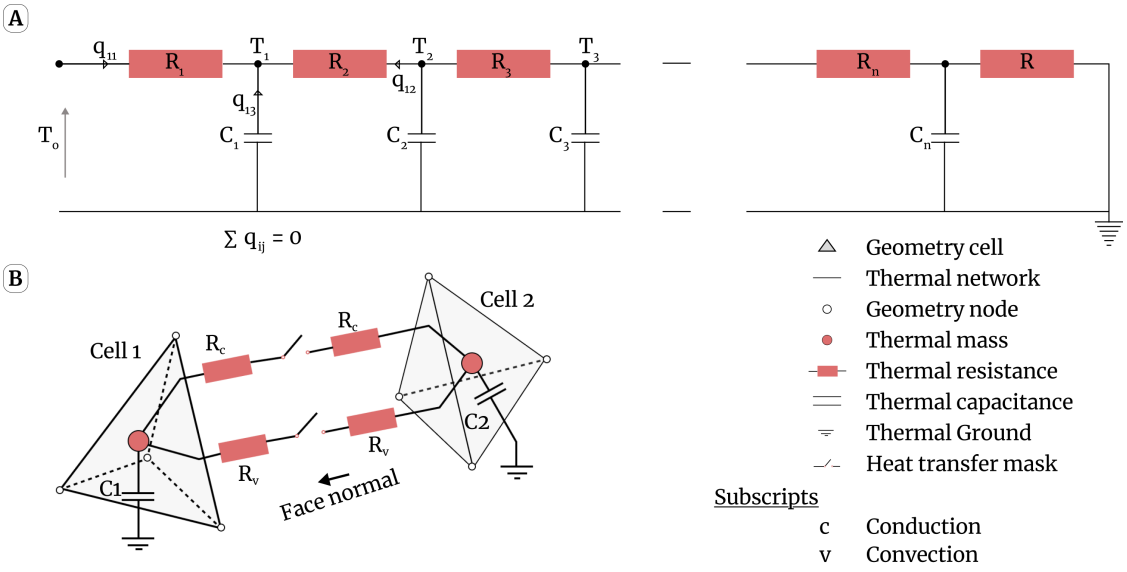


Figure 4.12: Thermal Network Model (TNM) electrical analogy showing the 1D equivalent circuit with conductive (Rc), convective (Rv), and advective (Ra) resistances and nodal capacitances. It further demonstrates the lump-mass blocking strategy, reducing the number of mesh cells to analysis blocks for multi-zone analysis.

Complex systems with multiple nodes and faces are simplified for computational efficiency using lumped mass blocking, in which spatially adjacent cells with similar thermal characteristics are grouped into discrete blocks [87]. A spatial hash algorithm first splits the domain into approximate blocks, followed by a Dijkstra-like connectivity check to ensure no cells become disconnected. The

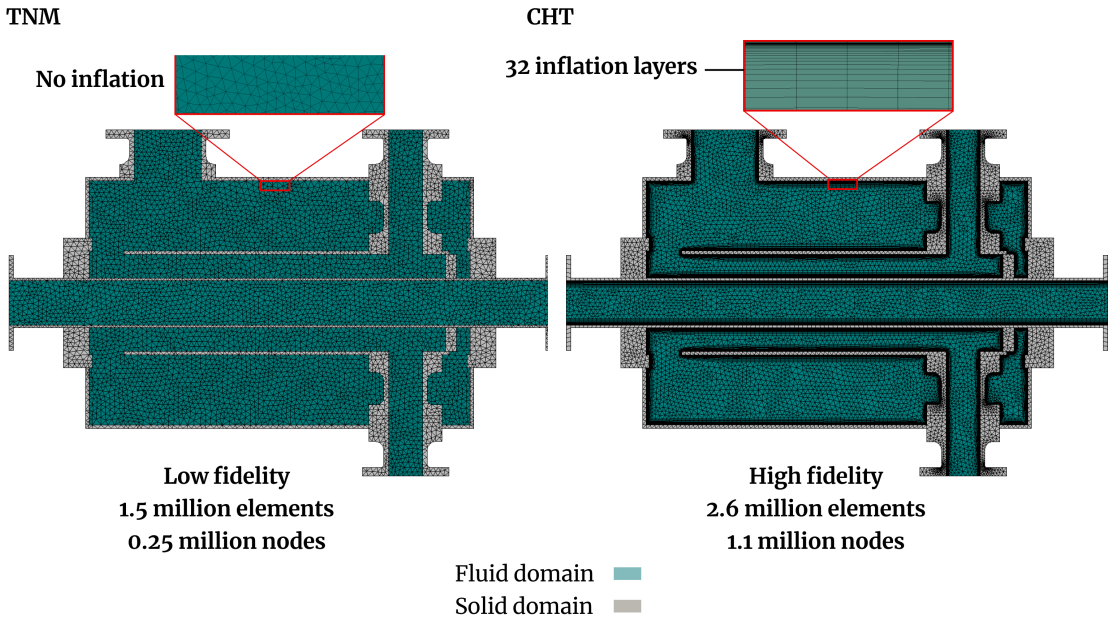


Figure 4.13: Comparison of high-fidelity CHT mesh (2.6×10^6 elements, with inflation layers) and low-fidelity TNM mesh (1.5×10^6 elements, no inflation layers), illustrating the 75% reduction in node density that enables rapid thermal field resolution.

thermal resistances and capacitances of the collected cells are then summed in series and parallel, analogous to combining resistors and capacitors in an electrical circuit, to produce a single equivalent lumped mass for each block [88]. The TNM is designed as a fast temperature numerical model. The 1.5 million cells of the TNM mesh are lumped into 40 blocks, resulting in a much smaller circuit and simplified system analysis. The number of blocks is selected to ensure that the local PC can compute transient analysis within the required timeframe for real-time monitoring during transient natural cooling.

Methodologies for developing thermal networks, including the traditional models and mesh-driven methodologies using a tetrahedral mesh to define the mesh geometry, cell connectivities, cell resistance and capacitance, are detailed in the literature [89]. TNM uses the python library *meshio* to read and extract mesh file data [90]. Figure 4.13 shows the tetrahedral mesh structure, where the TNM mesh is coarser than the high-fidelity CHT mesh. It does not feature inflation layers to minimise the computational requirements while maintaining reliable accuracy.

Based on this blocked circuit, the temperature of every node is computed as:

$$T^{n+1} = (D + C\,E\,G\,F)\,T^{n} \tag{4.4}$$

where **C** is the capacitance matrix, with diagonal entries $C = \rho V C_p$ $[\mathrm{J\,K^{-1}}]$ representing the lumped thermal capacitance of each block, **G** is the conductance matrix, **D** is the diagonal matrix, **E** is the heat flow summation matrix, **F** is the face matrix, and T^n is the temperature vector at the n-th timestep [88]. The matrix product $C\,E\,G\,F$ maps the thermal conductances and face heat flows through the capacitance of each block to compute the temperature update at each timestep.

The numerical model determines a suitable timestep size and then runs for the required duration. For this case, a fluid domain time constant in the order of 1×10^{-5} s is used and stepped to match larger solid timesteps. The blocking system implies that the timestep analysis is implemented on a few nodal points to capture fluid characteristics while enhancing efficiency instead of analysing all mesh nodes. Transformations like kriging interpolation to reconstruct the thermal field after the simulation are further detailed in [24]. Conductive (R_c), convective (R_v) or advective resistances (R_a) are defined by Equation 4.5. While the thermal conductivities, area, specific heat, and characteristic length of the solid and fluid domains cells are pre-set and assumed to only change negligibly with temperature changes, the heat transfer coefficient at the boundary layer is more challenging to resolve, especially with complex solid-fluid interactions and intricate geometries characteristic of steam turbines.

$$R_c = \frac{L}{kA}, \quad R_v = \frac{1}{h_1 A}, \quad R_a = \frac{1}{\dot{m} C_p} \tag{4.5}$$

A hybrid fidelity methodology was applied to address the complexity of defining the heat transfer coefficient (HTC) boundary condition using a pre-computed high-fidelity Conjugate Heat Transfer (CHT) model to set the complex boundary conditions. CHT steady-state and transient shutdown numerical analysis methodology described in Section 4.1 predicts the normative thermal and flow fields on the OTCR. The computational demand of the CHT, requiring cloud-based computing, illustrates the challenge for multiple steam turbine operations or for digital twinning

and machine learning that requires a large learning dataset. It is proposed that a few pre-computed conditions be modelled and used as the basis for faster low-fidelity models to bridge the large data gap for digital twinning systems. The TNM mesh used for the hybrid fidelity model is coarser, comprising 0.25×10^6 of nodes (75% reduction in the mesh node density) and 1.5×10^6 elements, enabling more rapid thermal field analysis.

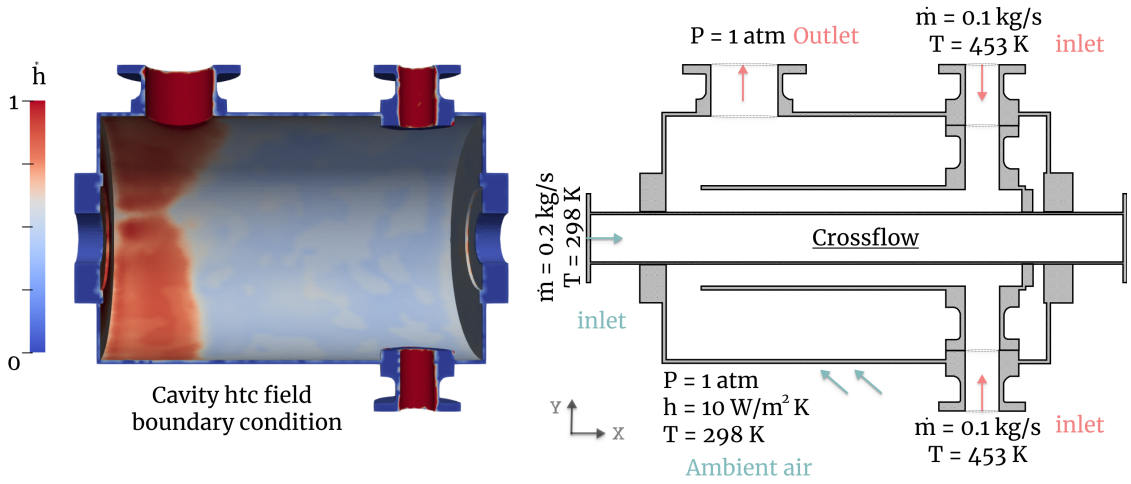


Figure 4.14: Boundary condition setting for the TNM equivalent to the CHT, alongside spatially varying heat transfer coefficient derived directly from the converged CHT solution. The heat transfer coefficient reaches up to $h_{\max} = 40\ \mathrm{W\,m^{-2}\,K^{-1}}$ and is shown normalised as $h^* = h/h_{\max}$ to illustrate the spatial variation across the casing surface.

Figure 4.14 shows the boundary conditions for the hybrid fidelity simulation with the equivalent conditions of mass flow rate, ambient temperatures of the high-fidelity analysis. Fluid properties and coupled conditions like fluid velocity and HTC are pre-computed by the converged high-fidelity CHT and used for the TNM. The solution from the CHT comprising the HTC and velocity fields is directly read by the TNM, which then reconstructs these fields for accurate thermal analysis with the new methodology. These HTCs and fluid field vectors get converted to the thermal circuit conductance and capacitance for the TNM resolution. Boundary conditions could be interpolated with this methodology between operational states to obtain big data for fast machine learning to predict complex turbine fields.

The material solid and fluid properties are equivalent to the OTCR properties and the high-fidelity numerical analysis.

After the solving process is completed, based on the number of iteration timesteps set by the user, the post-process recalculates the interpolated values of the temperature field. The TNM requires two categories of input (imported files and manually entered boundary conditions). The imported files contain the mesh geometry, cell connectivity, cell volumes, and face areas, and the spatially varying heat transfer coefficient and velocity fields extracted from the converged CHT solution. Other boundary conditions, including the inlet temperature and the outer wall heat transfer coefficient, are manually entered as inputs. The spatially varying heat transfer coefficient field from the CHT is interpolated onto the coarser TNM mesh using a nearest-neighbour interpolation criterion, assigning to each TNM cell the heat transfer coefficient of the closest CHT cell by Euclidean distance. The number of solved iterations is determined based on the solid timestep size required to attain steady-state. For a timestep size of $\Delta t = 0.11$ s, 98,200 timesteps are required for the 3-hour experiment duration. This simulation of 98,000 iterations from start-up was completed in less than 30 minutes. Compared to the CHT, the TNM numerical model provides a significant speed improvement, enabling real-time analysis of turbine temperature fields.

Hybrid transient cooling analyses for the defined operating point is also configured with Unsteady RANS (URANS) with $k-\omega$ SST Simple Gradient Diffusion Hypothesis (SGDH) turbulence model [30], for the post-shutdown natural cooling. High-fidelity CHT loosely couples the solid and fluid domains based on the method developed in [81], using a 0.1-second time step over a 1-hour duration (36,000 timesteps) with 500 iterations per time step and the same residuals as the steady-state simulations while maintaining solution stability. The solution fields are recorded with a 10-minute periodicity. The high-fidelity flow field and HTC boundary conditions data are transferred to the low-fidelity analysis using an automated interface between CHT and TNM software in the Python environment, as illustrated in Figure 4.15. $\Delta t = 10$ minutes is used as the stepwise time, and each

TNM transient solution is resolved for this time duration. The resulting solution for one time step is the initial condition of the next timestep, and the process loop continues for the required shutdown duration. Pre-computed HTC is required as the fluid properties evolve through the cooling process. The characteristic stepwise time should be optimised to capture flow field pattern evolutions for enhanced thermal field resolution at the solid-fluid boundaries and enhanced accuracy, as assuming constant HTC results in significant modelling errors. The hybrid fidelity method addresses the limitations of data resolution, computational efficiency, and accuracy of numerical analytic methods. While the CHT analysis could only be achieved with cloud computing capability, the hybrid simulation process, including mesh generation, pre-processing, solving, and post-processing, was executed in 6 hours. The solution requires 4 hours for a 3-hour cooling process, almost tracking the cooling in real time on a 64-bit local PC with 16 cores, 3.5 GHz, and 128 GB RAM. Upgrading the computing capacity or utilising faster GPUs enables the system to execute real-time transient shutdown analysis and facilitates real-time optimisation and control of thermal fields using novel models. Pre-computed CHT simulation can be executed, and the interpolation of boundary conditions between states can enable multiple hybrid fidelity simulations and real-time field prediction.

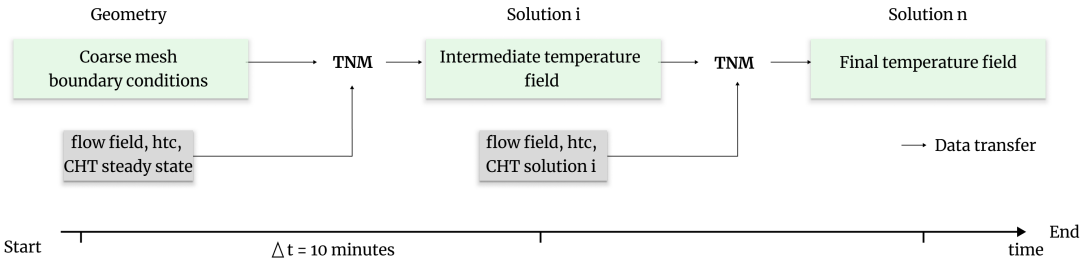


Figure 4.15: The process flowchart for the hybrid fidelity transient shutdown simulation comprises CHT fields, which initialises the TNM at each 10-minute timestep, and the TNM resolves the thermal field for that interval. The output becomes the initial condition for the next step, and this continues for the full shutdown duration.

4.4 Steady-State Results

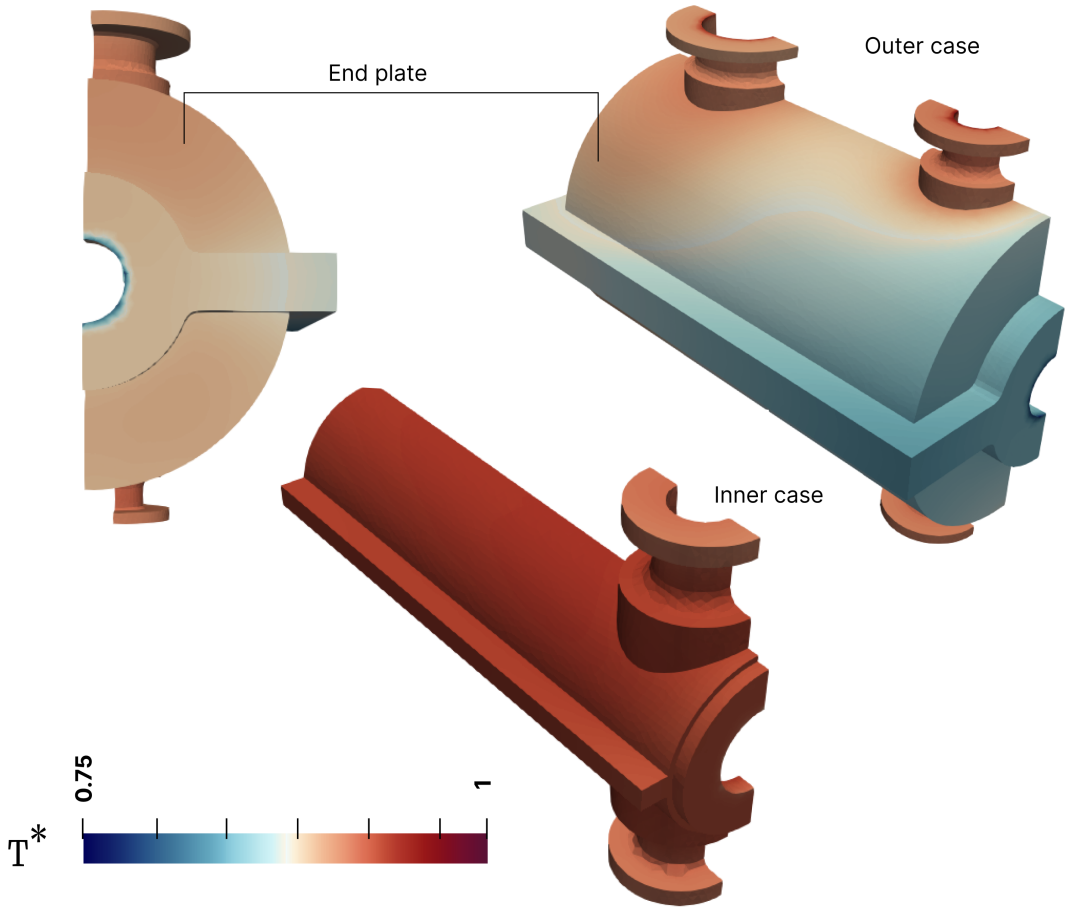


Figure 4.16: The steady-state outer casing temperature field predicted by the TNM numerical model exhibits higher thermal gradients at the inlet flange and in the thick-walled regions.

Figure 4.16 presents the temperature fields of the outer casing for the hybrid fidelity TNM models. They illustrate higher thermal gradients in regions with thicker or non-uniform geometry, such as the inlet and split flanges, due to the varying thermal resistances and fluxes. While both models capture the primary thermal field features, which makes the fast numerical model a viable methodology for real-time control, the TNM exhibits smoother temperature transitions with less pronounced gradients than the CHT. It predicts a warmer and more uniform temperature distribution at the outer case end plate, and the inner casing shows a nearly uniform temperature field. Tables 4.7 and 4.6 show the detailed comparison

of the solid domain results between the sparse physical measurements, high-fidelity CHT and hybrid fidelity TNM models highlighting the difference between the physical temperature measurements from the thermocouples and the corresponding numerical analysis averaged across the planes. Both the high-fidelity CHT and TNM models exhibit results with a deviation of less than 7% from the physically measured values. The CHT performs better with marginally improved accuracy. For instance, in plane A of the outer casing, the CHT results only deviate by less than 1% compared to the physical measurement, whereas the TNM result is 6.8% different due to the nature of fluid flow and casing geometry. At this location, the fluid domain is incident on the outer case end-plate with turbulent flow, which the TNM does not accurately resolve due to the complex pattern. Note, however, the accuracy in planes H, with more contrasting flow structure, indicating the need for improved model development and tuning with OTCR data. The hotter inner casing with reduced flow complexities exhibits higher accuracy, with all the measured planes within a 3% deviation across all measurement planes.

Table 4.6: Average percentage difference between numerical predictions (CHT and TNM) and experimental thermocouple measurements for each axial plane of the outer casing, calculated as [Numerical − Experiment] [%] and averaged across all circumferential thermocouple positions within each plane [84].

Plane	X [mm]	CHT-Experiment [%]	TNM-Experiment [%]
A	0	0.78	6.81
B	50	2.37	4.04
C	130	3.37	4.01
D	241	0.32	3.32
E	424	1.51	2.95
F	603	2.26	2.78
G	786	2.32	1.82
H	950	0.93	0.42
I	1000	2.74	3.73

Complex steam turbine systems involve dynamic, interacting properties across solid and fluid domains. Figures 4.14, 4.15, and 4.16 present the polar plots of normalised temperatures at defined locations on the outer and inner casings. It illustrates that while the end plate (plane E_i) of the inner case shows that the

Table 4.7: Average percentage difference between numerical predictions (CHT and TNM) and experimental thermocouple measurements for each axial plane of the inner casing, calculated as [Numerical − Experiment] [%] and averaged across all circumferential thermocouple positions within each plane [84].

Plane	X [mm]	|CHT–Experiment| [%]	|TNM–Experiment| [%]
A_i	241	1.69	2.05
B_i	424	2.83	2.33
C_i	603	2.47	2.44
D_i	786	1.79	2.80
E_i	890	0.53	0.87

TNM results align with the physical measurements and the high-fidelity CHT, the other planes show lower TNM temperatures. The hybrid fidelity models are also aligned in the outer casing polar plots. Integrating hybrid physical measurement and high-fidelity models could enhance the calibration of the data reconstruction process, capture localised thermal behaviours, and improve the thermal contour field accuracy.

Figure 4.20 illustrates the natural cooling post-shutdown, showing normalised temperatures at defined measurement locations over a 120-minute temperature decay period. Variations in casing thicknesses and dynamic flow conditions result in different Prandtl and Fourier numbers, influencing cooling rates [66]. Although the unsteady CHT implemented in ANSYS Fluent relies on a simplified time-step and the Simple Gradient Diffusion Hypothesis (SGDH) turbulence model, which may not fully resolve normal and parallel heat flux components at solid-fluid interfaces, it captured the temperature decay process for this validation with less than 5% difference between measured and analytical values. More accurate models are computationally intensive and require specialised boundary layers and turbulent model treatment, like a more advanced turbulence model that better models wall heat flux, precise characteristic lengths, and adaptive time-step sizes over long-duration natural cooling process [30].

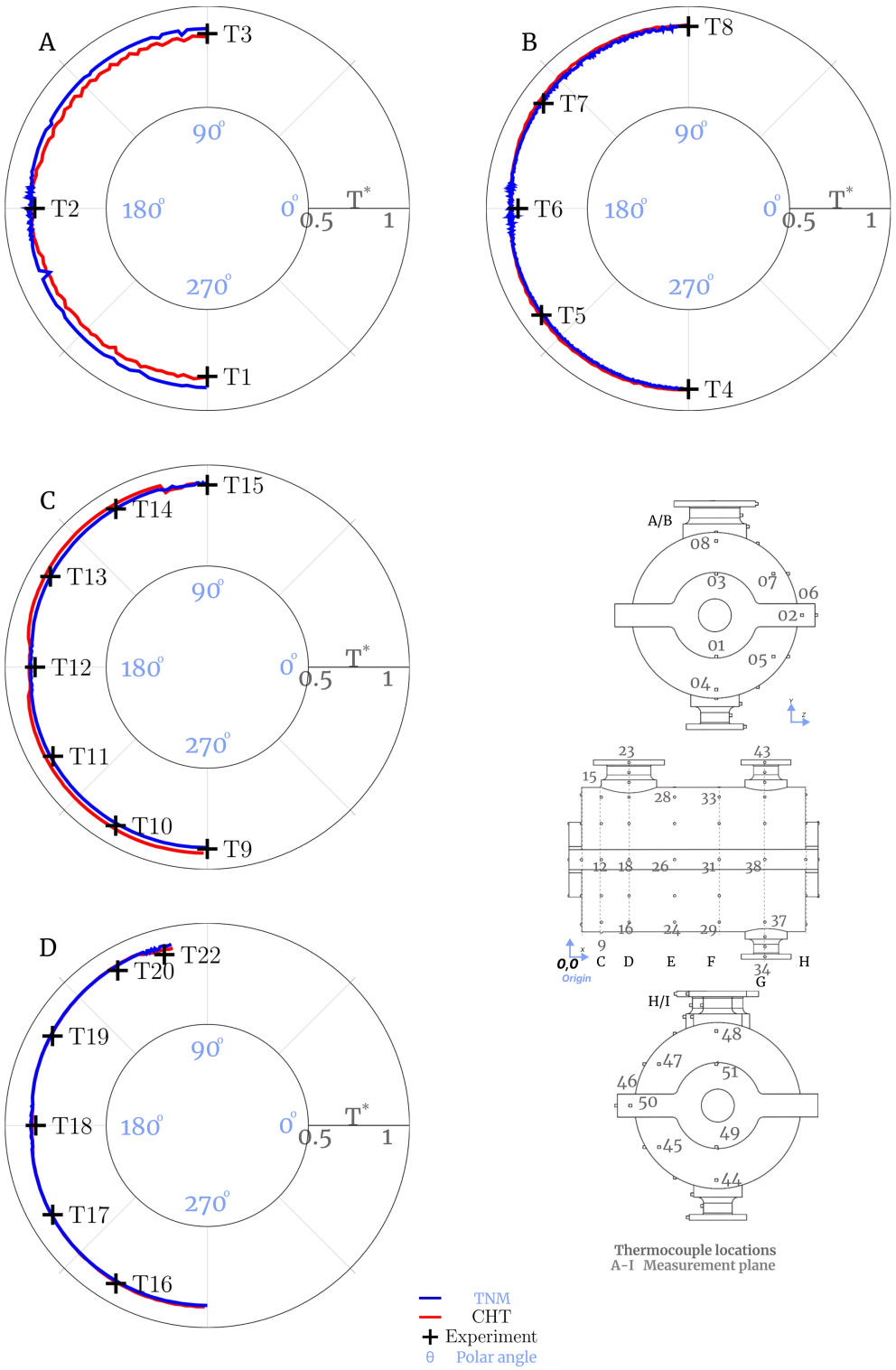


Figure 4.17: Polar plots of normalised outer casing temperature $T^* = T/T_{\max}$ at planes A–D, comparing CHT, TNM, and experimental measurements at full load steady-state conditions ($\dot{m} = 0.2$ kg/s, $T_{in} = 453$ K, $T_\infty = 298$ K.)

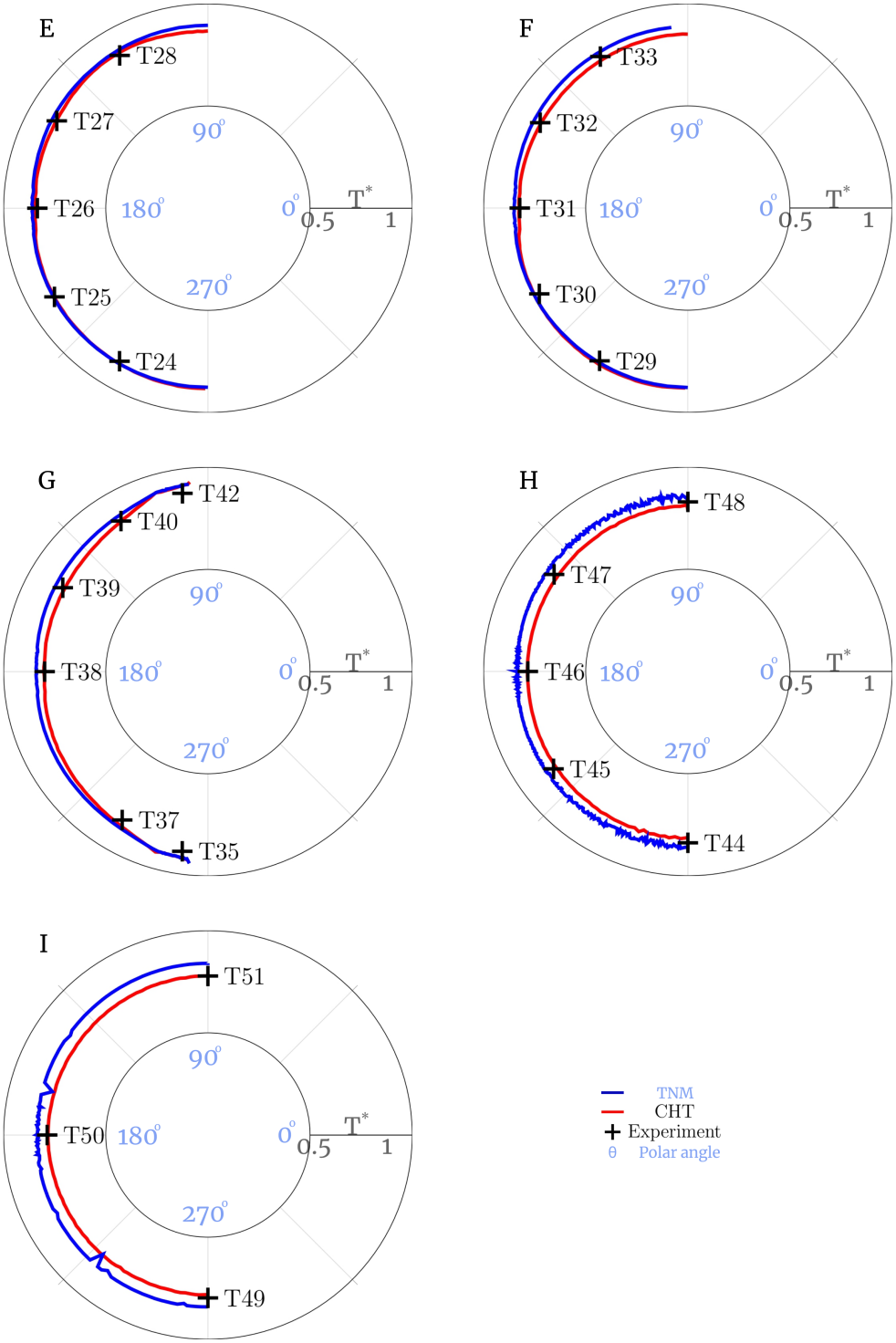


Figure 4.18: Polar plots of normalised outer casing temperature $T^* = T/T_{\max}$ at planes E–I, comparing CHT, TNM, and experimental measurements at steady-state full-load conditions ($\dot{m} = 0.2$ kg/s, $T_{in} = 453$ K, $T_\infty = 298$ K.)

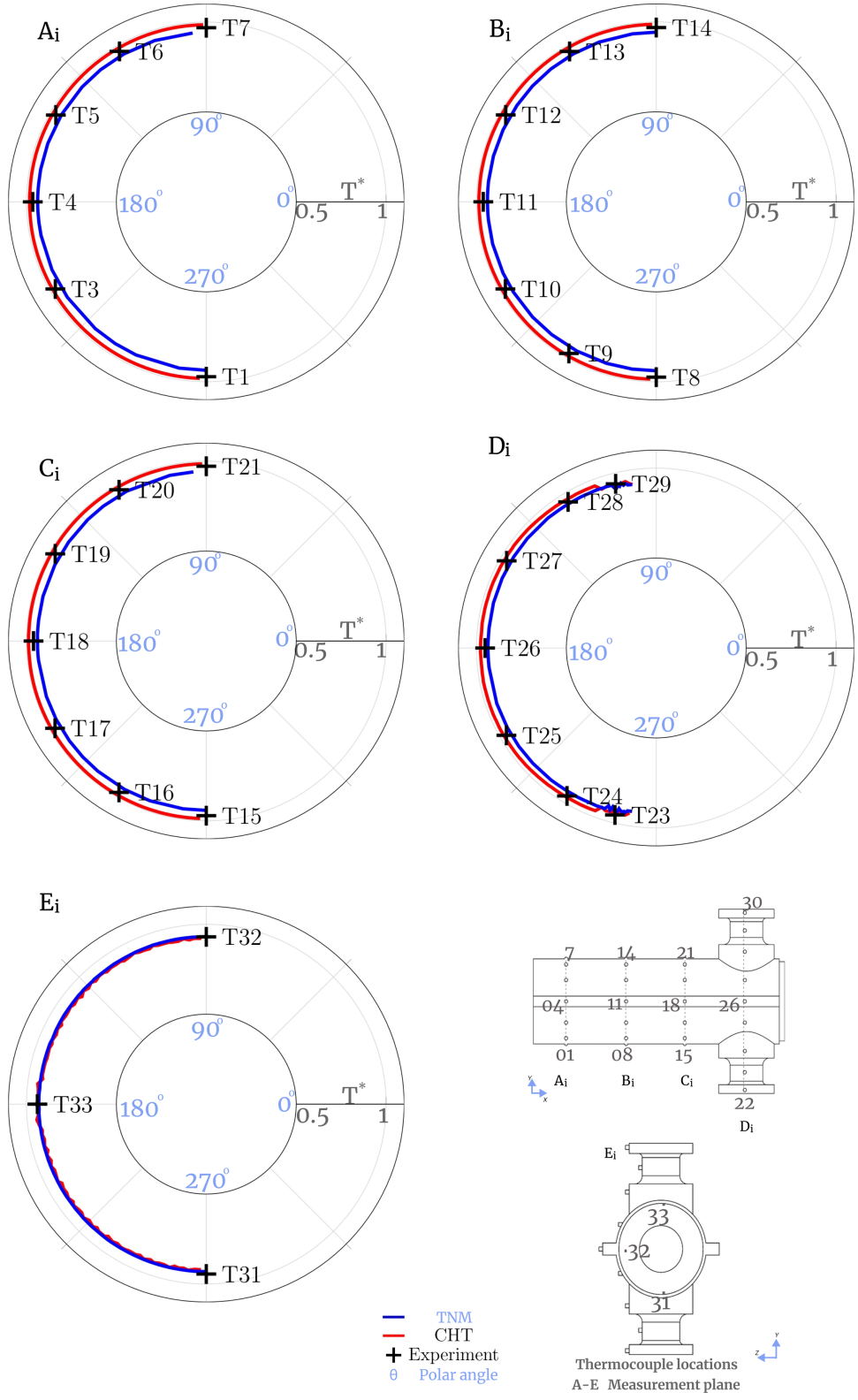


Figure 4.19: Polar plots of normalised inner casing temperature $T^* = T/T_{\max}$ at planes A_i–E_i, comparing CHT, TNM, and experimental measurements at steady-state full-load conditions ($\dot{m} = 0.2$ kg/s, $T_{in} = 453$ K, $T_\infty = 298$ K.)

Transient state TNM and experimental results

The ability of the TNM model to replicate the high-fidelity CHT cooling rate suggests that complex transient cooling can be captured for real-time control using simpler models with hybrid data transfer and field resolution. To enhance computational efficiency and solution accuracy, sensitivity analysis and optimisation are needed to determine the optimal data transfer frequency between the multi-fidelity models. Addressing steady-state energy transfer and reconstruction modes will further enhance the transient methodology developed in this work. The OTCR and hybrid methodology enable rapid prediction of turbine thermal fields through fast hybrid analysis. Hybrid TNM enables real-time analysis of complex transient processes, facilitating the optimisation and control of thermal fields and stresses for improved plant operational flexibility.

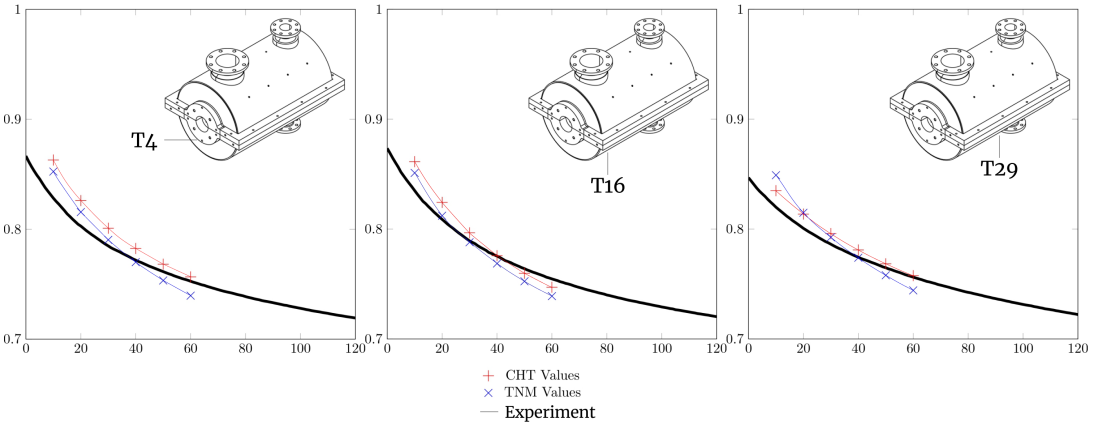


Figure 4.20: Post-shutdown transient natural cooling at thermocouples T4, T16, and T29, comparing CHT, TNM predictions, and physical measurements. Steady-state full-load- ($\dot{m} = 0.2$ kg/s, $T_{in} = 453$ K). Shutdown condition- ($\dot{m} = 0$ kg/s), $T_{\infty} = 298$ K.

4.5 Summary

This chapter presents a high-fidelity and hybrid-fidelity numerical analysis of the thermal fields of the OTCR. Steady-state and transient analysis are performed to evaluate the conformity of the OTCR to validate novel numerical analysis tools and methods. Because of the complexity of turbine thermal fields and the computational complexity, new models are required for rapid and accurate analysis of various turbine components. Rapidly analysing these components is the critical enabling factor for actively controlling components and changing the operational philosophy of these systems from simple passive structural members to control systems.

High-fidelity steady-state and transient analysis is performed using the Ansys Fluent 2023 R1 environment for the solid-fluid coupled CHT on the five domain components. The simulation, conducted on the cloud computing cluster, converged, providing high-fidelity fields of fluid velocity, fluid temperature, and solid temperature. The fluid velocity results depict flow topologies ranging from low to high velocity and recirculating flows that impact the solid-fluid HTC boundary and the solid thermal field. The solid domain comprised the outer and inner casing with marked regions of high temperature gradient, especially at the interface between thick and thin-walled surfaces and around the inlet. These regions are critical areas explored for design changes aimed at reducing thermal gradients.

The steady-state and transient simulation results are compared with physical measurements, and the results are tabulated. For all the measurement locations, the numerical results and physical measurements are within 5% difference. The complex fluid cavity is also analysed for its accuracy. The results capture the critical features, such as near-wall physics, while providing confidence in the accuracy of the OTCR to validate novel turbine analysis models.

Due to the computational demand of the high-fidelity model, a hybrid fidelity thermal analysis using TNM and data transfer from high to low fidelity tools is introduced. The TNM converts thermal systems into electrical circuits, lumps cells, and applies electrical laws to resolve thermal fields quickly. The real-time analysis leverages high-fidelity results to validate the possibility of interpolating

between states, thereby enabling accurate pseudo-transient analysis and facilitating real-time turbine thermal analysis. Like the high-fidelity results, the hybrid thermal analysis incorporates physical measurements and offers the framework for automated data transfer between varying resolutions of thermal fields. The OTCR's ability to validate thermal fields and the ability of new models to capture thermal and flow characteristics of the OTCR enable critical turbine flexibility research. It creates possibilities for optimising design components to play active, real-time control functions.

5

Active and Passive Thermal Gradient Optimisation

This chapter presents methodologies to reduce thermal gradients on the casings of power-generating turbines. Real-time active control methods using heat flux as the input control variable are presented and verified using the OTCR experimental setup. The new optimisation methods employ complex hybrid fidelity numerical analysis for both steady-state and transient natural cooling shutdown cases. Hybrid active and passive control methods are presented and numerically analysed.

5.1 Thermal Gradients Overview

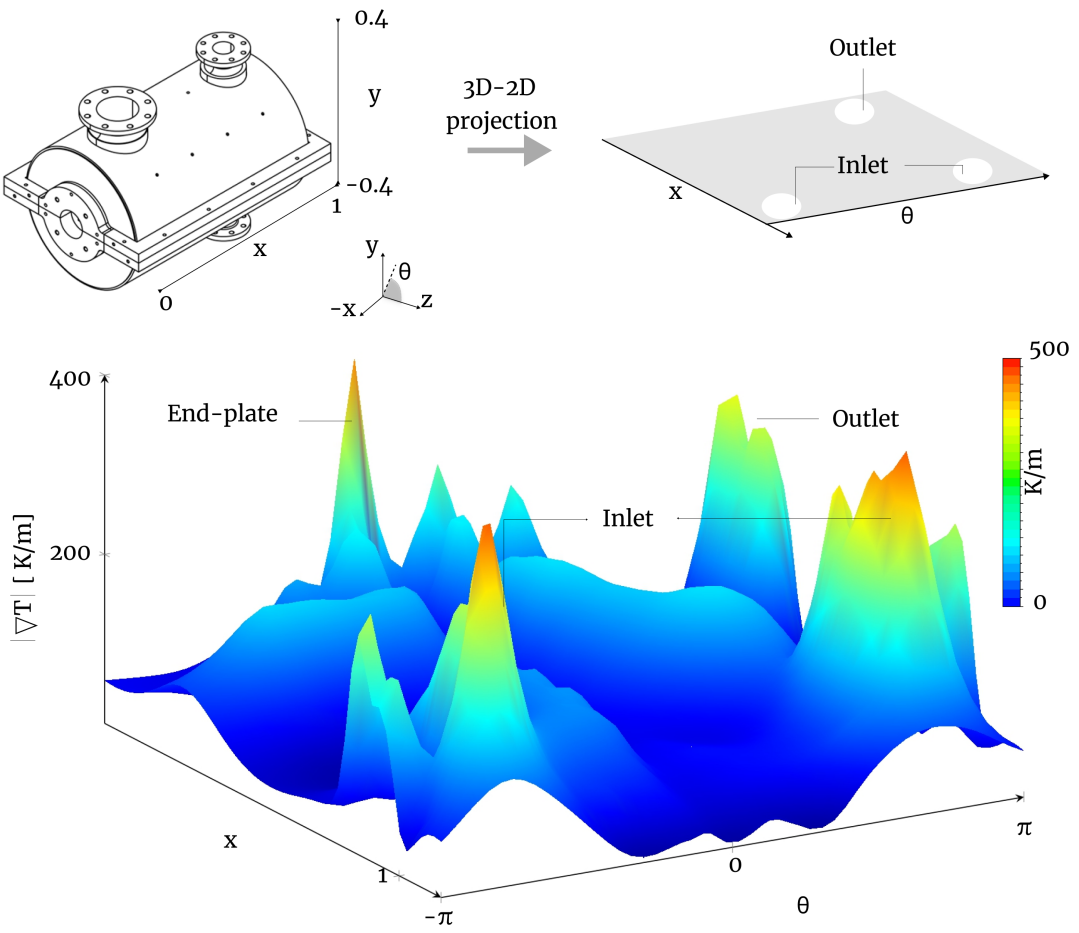
The thermal and flow field of the OTCR result in the thermal gradient field depicted in Figure 5.1. The thermal gradient field is computed by evaluating the magnitude of the local temperature thermal gradient vector at each mesh cell centroid as:

$$|\nabla T| = \sqrt{\left(\frac{\partial T}{\partial x}\right)^2 + \left(\frac{\partial T}{\partial y}\right)^2 + \left(\frac{\partial T}{\partial z}\right)^2} \quad [\mathrm{Km}^{-1}] \tag{5.1}$$

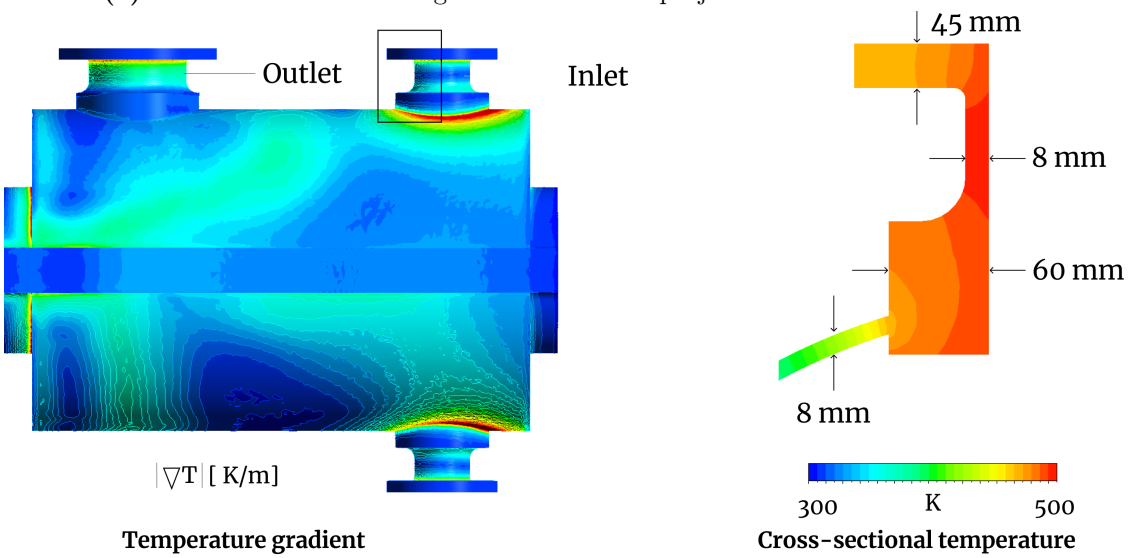
where $\partial T/\partial x$, $\partial T/\partial y$, and $\partial T/\partial z$ are the partial derivatives of temperature in each coordinate direction, computed from the cell-centred temperature values of a Green-Gauss cell-based scheme of *Ansys Fluent*. The thermal gradient, $|\nabla T|$ $[\mathrm{K\,m}^{-1}]$ is proportional to the local thermal stress along the length over which

the thermal gradient acts. Figure 5.1a shows x-θ plane 2D projection of the 3D thermal gradient field of the OTCR. The thermal gradients are plotted on the 2D surface to represent the intensity of the thermal gradient on the casing. The identified regions of high thermal gradient and, consequently, stresses, including the inlet, outlet, and end plate regions, are highlighted, aligning with previous studies in the turbine literature [91]. Figure 5.1b shows the 3D thermal gradient field on the casing to reference. It shows the temperature field on a scaled inlet region with casing geometry intricacies, including the wide-ranging thicknesses [8 mm - 60 mm] and the shape complexities, which implies complex thermal analysis when coupled with fluid fields. In the inlet region, the hot working fluid flows from the inlet of the outer casing to the inlet of the inner casing, through the main flow path to the exhaust with some recirculating flows in the turbine cavity. The flow pattern indicates that the working fluid exchanges energy with the inner casing, and the recirculating flows have resulted in a lower temperature increase in parts of the outer casing. The heat transfer mechanism, governed by complex flows, is influenced by the effect of casing geometry, varying thermal resistance, and other thermal properties, which affect the conductive-convective heat transfer interactions and result in a thermal gradient field.

Numerically analysed and measured thermal fields and thermal gradients for steam turbine casings to identify thermal stresses, clearances, and deformations are further detailed in research [11, 57, 92, 93]. Geometric features such as wall thicknesses and flow characteristics such as pressure, main flow, and cavity flow, produce distinct thermal effects, as observed with the OTCR. These thermal stresses and clearance limitations affect the cyclic operation of power-generating turbines. The following sections present new methodologies to minimise these thermal gradients.



(a) An overview of thermal gradient on 3D-2D projected surface of the OTCR



(b) OTCR casing with high thermal gradient section showing geometric detail and cross-section temperature profile

Figure 5.1: Steady-state thermal gradients on the OTCR casing, indicating corresponding thermal gradient distribution [$\mathrm{K\,m^{-1}}$] and potential regions of higher thermal stress, especially in geometrically non-uniform and complex flow regions.

5.1.1 Active Control Methods

Active control is a thermal management strategy utilising the active transfer of external heat flux to the turbine to modify the thermal boundary condition and thermal field distribution. Although active control for steam turbine casings has been limited in the literature, similar models have been applied to other turbine parts and to other optimisation objectives by actively changing some boundary conditions, especially in the fluid domains. NASA developed active cooling of turbine surfaces using fluidic devices, active fluid jets, and film cooling to vary surface boundary fluxes. Similar methodology is utilised where spacecraft panels are heated or cooled by radiators with modulated fluxes to keep the boundary surface within desired ranges [94].

For active control using thermal fluxes, the governing equation when heat flux q is applied to the boundary for a homogeneous solid body of density ρ, specific heat c_p, and thermal conductivity k, the temperature field $T(\xi, t)$ and thermal diffusivity $\alpha = k/(\rho c_p)$. When an external heat flux $q(\xi_s, t)$ is applied on the boundary, the boundary condition evolves with the transient heat, where $\partial T/\partial n$ is the normal derivative at the surface. Equations (5.2)–(5.3) show the prescription of boundary as active thermal control.

$$\rho c_p \frac{\partial T}{\partial t} = k\nabla^2 T, \tag{5.2}$$

$$-k\frac{\partial T}{\partial n} = q(\xi_s, t), \tag{5.3}$$

For the transient behaviour of a solid initially at temperature T_i, subject to a constant surface heat flux q_0 at $\xi = 0$, the temperature at a point evolves from past flux history with the rate of diffusion of heat from the boundary through the entire solid body to attain a steady-state condition. This implies a decaying effect with depth ξ and time t, as diffusion spreads the thermal energy throughout the solid. This phenomenon, where the heat flux increases temperatures over time until a decay occurs towards more uniform fields, is explored in the active control methodology.

$$T(\xi,t) - T_i = \frac{2q_0}{k}\sqrt{\frac{\alpha t}{\pi}}\exp\left(-\frac{\xi^2}{4\alpha t}\right) - \frac{q_0\xi}{k}\mathrm{erfc}\left(\frac{\xi}{2\sqrt{\alpha t}}\right) \tag{5.4}$$

Equation (5.4) [66, 95] illustrates the analytical principle exploited in this methodology. The applied surface heat flux q_0 establishes a boundary thermal gradient that initially drives a rapid rise in surface temperature, where $\mathrm{erfc}(\cdot)$ is the complementary error function. This influence decays with both depth, ξ, and time, t, as diffusion spreads the thermal energy throughout the solid. By actively modulating the boundary flux, one can therefore shape the temperature fields: producing transient rises where heat is injected, and gradually steering the distribution toward more uniform fields as conduction equilibrates. Optimum heat flux magnitudes for casing parts result in predetermined temperature fields that can be defined and controlled. Determining the optimum heat flux on the casing is a very complex problem due to the limitations of thermal analysis as detailed in Section 2.3.

For the turbine casing, the optimisation problem is challenging. First, the non-homogeneity and complex nature of the geometry, with its various parts, make such analytical optimisation practically impossible. Treating the casing as a single unit will introduce significant errors because the parts (inlet, barrel, shaft, and outlet) depict distinct thermal fields and characteristics. Even for defined geometries, analytical solutions are demanding, and conventional thermal analysis requires partial differential equations on control volumes in the form of meshes to determine the thermal field solutions. Thus, optimising the entire field becomes even more complicated for basic analytical solutions due to the complexity of thermal fields, which involve millions of mesh control volumes as optimisation variables. Computing for this level of optimisation is prohibitively expensive.

To this end, this research proposes reimagining the design of turbine casings as dynamically functional sub-components that play active control functions, rather than a single structural unit. It adopts a finite element-like discretisation of a turbine casing for subsequent optimisation. Splitting the casing into a series of discrete thermal blocks allows for a more accurate calculation of the thermal

fields. Similar methods have been proposed to analyse turbine components in research and industry [12].

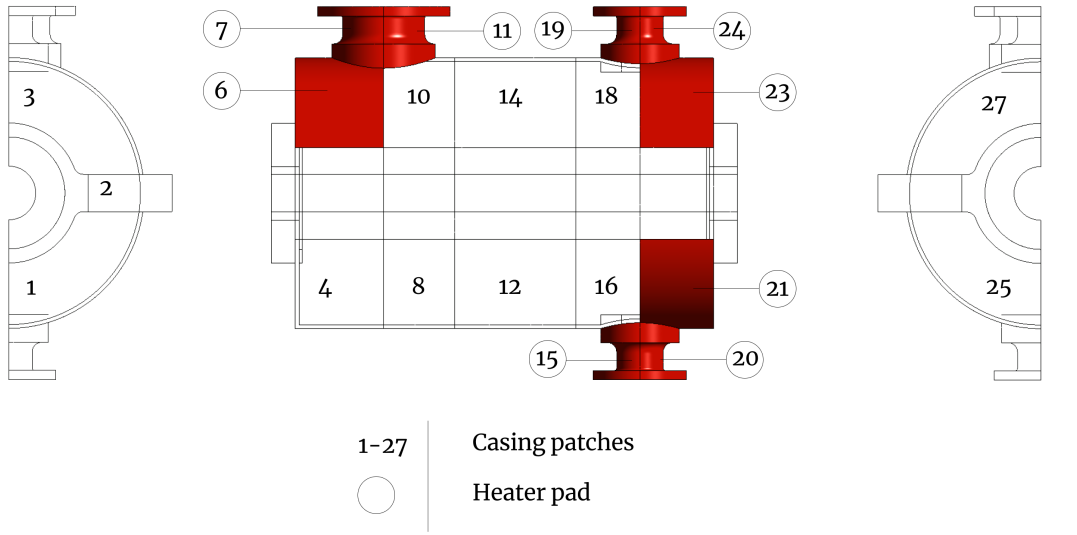


Figure 5.2: Discretisation of the OTCR casing into 27 independent thermal blocks, with heater pad locations identified for active boundary condition control. Red patches indicate the zones selected for active heat flux optimisation (zones 6, 7, 11, 15, 19, 20, 21, 23, and 24), corresponding to regions of highest thermal gradient identified from the preliminary CHT analysis.

As shown in Figure 5.2, the casing has 27 discrete components determined based on the preliminary analysis of the thermal field to identify regions of thermal field similarity and to compensate for geometric characteristics. For the methodology, each discrete block is treated as a solid body interacting with the adjoining bodies, similar to thermal networks, where each part is resolved based on the field characteristics in that part and the effect of the thermal characteristics of the other parts. The optimisation zones are selected based on regions of highest $|\nabla T|$ identified from the preliminary CHT analysis, to demonstrate the ability to control these high thermal gradients. Ideally, optimisation would cover the entire casing, but material and installation constraints limit the number of heater pads. The heater pads' silicone insulation minimises direct convective losses. Heating on turbine casings has been demonstrated industrially on a Siemens turbine by [61], confirming the feasibility of this approach on industrial turbines. More localised

heating strategies targeting individual geometric features were not investigated, but represent a natural extension for future work.

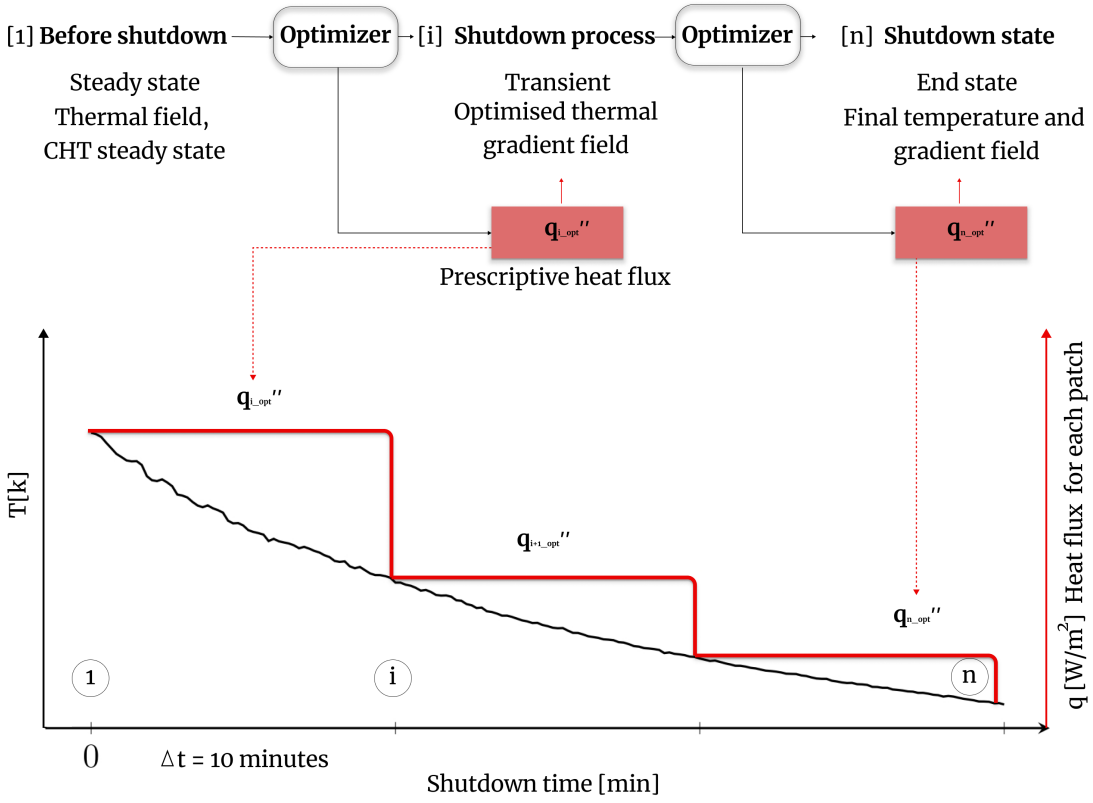


Figure 5.3: The spatio-temporal active control optimisation framework, which comprises the steady-state optimal heat flux, initialises the transient loop. At each 10-minute timestep, the optimiser determines the flux distribution to minimise the thermal gradient across all blocks, and the output field seeds the next timestep.

Figure 5.3 presents the framework for the discretised spatio-temporal optimisation problem of active control. The workflow is implemented in the PyFluent environment, which couples Ansys Fluent with Python. This integration provides access to Python's extensive optimisation libraries and the ability to automate solution processes, retaining Fluent's numerical analysis capabilities, enabling dynamic and automated control of the simulation process [96].

The second challenge is that real turbines exhibit complex and time-varying thermal fields during and between operating stages, necessitating transient optimisation approaches accounting for the unsteady nature of coupled fluid-solid domains. The Fourier number criterion ($\mathrm{Fo} = \alpha t / L^2 \gg 1$), where α is the thermal

diffusivity of steel and L is the characteristic wall thickness, is used to select the 10-minute timestep. For the OTCR casing wall thicknesses ranging from $L = 8$ mm to $L = 65$ mm, the Fourier number ranges from approximately 2 to 114 for the 10-minute discretisation interval.

Superposing the complexity of fluid flow, convective and advective heat transfer modes, and transitioning shutdown regimes further complicates the thermal response, introducing multiple timescales. Solving for a transient optimum is equally challenging due to the unsteady timescale problem [37]. To enable the spatio-temporal optimisation, both the spatial and temporal domains require discretisation for computational efficiency. A fast pre-computed solution could accelerate optimisation for turbine operations and serve as the zeroth-order solution for subsequent thermal gradient-based refinement. For each zone and at each timestep, the optimisation is solved to find an optimum heat flux and resolve the thermal field of the casing. $\Delta t = 10$ minutes is used as the stepwise time, and each optimal solution is resolved for this duration.

The optimisation process can be summarised as:

1. Begin with an unoptimised steady-state case and find the optimum thermal gradient under steady-state conditions.

2. Use the optimum steady-state temperature field as the input for the next transient (10 minutes) solution.

3. Optimise the thermal gradient field for the next transient (10-minute step). The output of each time step forms the input temperature field for the next transient time step, and the process iteration continues until the entire shutdown optimisation is simulated.

5.1.2 Optimisation Problem

For each time step defined as above, the optimisation approach is shown in Figure 5.4. At the start of the optimisation, the Fluent Case with geometry and a multi-domain mesh, as defined in Chapter 4, is imported into the PyFluent environment.

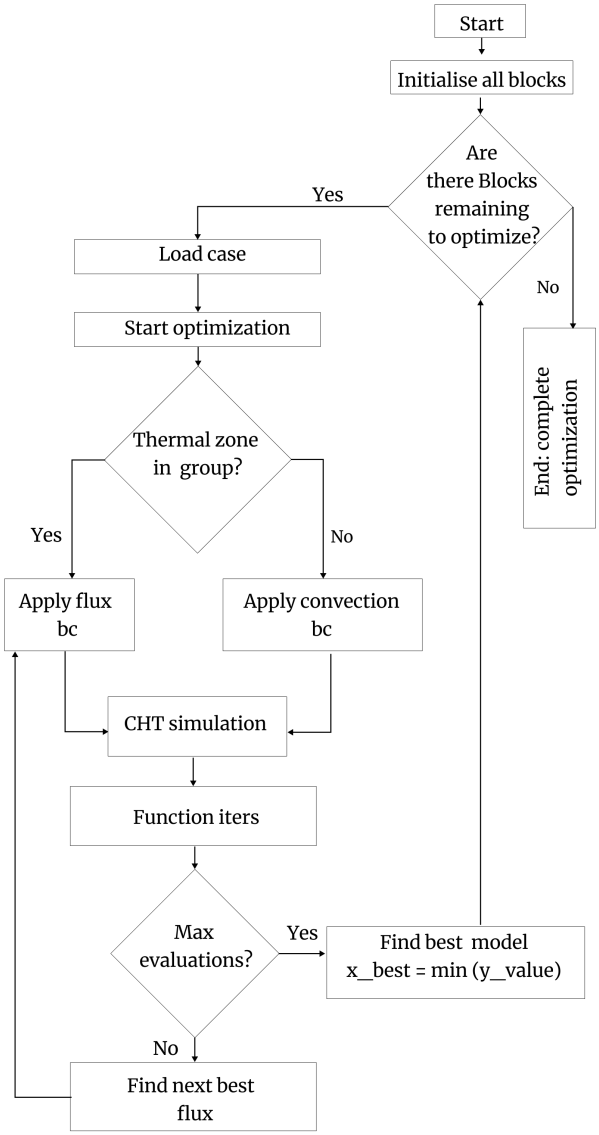


Figure 5.4: The block-wise Bayesian optimisation prioritises zones with a critical thermal gradient. A parametric heat flux is varied in steps via PyFluent automation, and the global optimum flux distribution is selected and applied.

The average thermal gradients of each discrete block are computed and evaluated to prioritise the zones where the objective function will be evaluated, thereby minimising computational requirements. The criteria to determine the worst thermal gradient zones could be dynamic based on absolute or normalised values, as well as average or maximum thermal gradient values. The average thermal gradients are computed, and the regions with thermal gradients, $|\nabla T| > 200\ \mathrm{K\,m^{-1}}$ are

denoted as the *blocks to optimise*, which are stored in a list for the optimisation problem through an automated process flow.

For the case to be optimised, and for the timestep, the boundary conditions are prescribed. Non-critical zones with no optimisation requirement maintained fixed convection boundary conditions (h = 10 W/m^2K, T = 298 K), consistent with the steady-state and transient CHT. The critical optimisation zones undergo parametric boundary condition setting through discrete heat flux variation, yielding a discrete parameter space $q \in [0, 1000]$ W/m^2 with discrete steps of 100 W/m^2. This parametric discretisation transforms the continuous optimisation problem into a finite combinatorial space, reducing the solution domain from an intractable continuous space to a more efficient discrete set. Without zone prioritisation, the total computational matrix encompasses a minimum of 270 transient solutions per time step, or 1,620 full-domain transient solutions for 1 hour. Even this simplified format is computationally demanding. Priority zone selection further constrains the problem to 60 transient evaluations per timestep and (600 for the one-hour transient shutdown), a significant reduction in computational costs. The PyFluent automation framework enables the systematic assignment of boundary conditions within the prescribed design space, facilitating autonomous optimisation iterations through the parametric landscape for improved tractability and efficiency.

The optimisation objective is to minimise the thermal gradient, a function of heat flux, thermal, and flow field, subject to the changing heat flux in the defined range.

$$\min_{q} \quad J = |\nabla T| \tag{5.5}$$

$$\text{where:} \quad |\nabla T| = \text{PyFluent}(q,\, BC,\, IC) \tag{5.6}$$

$$\text{subject to:} \quad q \in [0, 1000]\ \mathrm{W\,m^{-2}} \tag{5.7}$$

$$q_i = \text{discrete heat flux for zone } i$$

BC and IC are the boundary conditions and initial conditions, respectively. The objective function is modelled based on the energy and momentum equation of the Reynolds–averaged Navier–Stokes (RANS) $k - \omega SST$ viscous turbulence CHT

model in Equation (4.3). The Bayesian optimisation of the Python optimisation library [97] is used to determine the optimal thermal gradient and the input flux that results in this thermal gradient. Bayesian optimisation model constructs a probabilistic surrogate of the expensive objective model and intelligently selects the next evaluation point for flux. It begins by evaluating random inputs to assess the objective function and trains the model to identify the optimal input that yields the best output. New iterations are done until the result converges. This model further enhances computational efficiency and integrates well with the Fluent model, incorporating multiple constraints [98]. It can also scale with dimensionality. For instance, more sampling points could be evaluated, and refined changes in flux could be used to enhance results and for other applications.

After the evaluations, the optimisation results are saved, including the fluxes and temperature fields. If an unoptimised region remains in the list, it is evaluated; otherwise, the optimisation loop is stopped. The model extracts relevant temperature and thermal gradient field data from the case, and the case is automatically exported as input for the next iteration step. The process is repeated until the set duration (1 hour) for the transient shutdown, and the results are saved.

Table 5.1 presents the optimal results of the heat flux distribution obtained using the thermal gradient optimisation framework. It shows the varying boundary condition requirements across discrete 10-minute intervals, where $t = 0$ corresponds to the steady-state optimal configuration. A critical post-processing and validation procedure involves quantifying the coupling effects between optimisation zones, specifically examining how parametric modification of boundary conditions in individual zones influences the thermal response of adjacent zones.

To validate the discrete optimisation methodology, thermal gradients computed from the full-domain boundary condition specification were compared against results obtained using the discretised parametric approach, using the optimal flux boundary condition as a control metric. The deviation magnitudes are below 5% ($|\Delta T_{full} - \Delta T_{discrete}|/\Delta T_{full} < 5\%$), confirming the fidelity of the discrete solution strategy. Validation establishes confidence in the rapid optimisation

Table 5.1: Optimised heat flux requirements [$\mathrm{W\,m^{-2}}$] for active thermal gradient control of the OTCR at each timestep during transient shutdown ($\dot{m} = 0$ kg/s, $T_\infty = 298$ K, $\Delta t = 10$ min, initial condition: steady-state full-load at $\dot{m} = 0.2$ kg/s, $T_{in} = 453$ K).

Time [min]	Zone 6	Zone 7	Zone 11	Zone 15	Zone 19	Zone 20	Zone 21	Zone 23	Zone 24
0	400	1000	1000	800	800	800	400	400	800
10	1000	200	200	100	100	100	1000	1000	100
20	1000	100	100	100	100	100	1000	1000	100
30	1000	100	100	100	100	100	1000	1000	100
40	1000	100	100	100	100	100	1000	1000	100
50	1000	100	100	100	100	100	1000	1000	100
60	1000	600	600	100	100	100	1000	1000	100

framework for minimising thermal gradients and reducing consequent thermal stress in transient turbine operations.

5.1.3 Optimisation Results

Figure 5.5 shows the optimised transient temperature field of the OTCR from a steady-state full load condition before shutdown, through the shutdown process. The temperature field of the optimised OTCR maintains higher values for the optimised case compared to the unoptimised case. This result is significant in developing hot standby conditions for restarting turbines. Such hot standby modes developed through trace heating systems have been found to decrease start-up time by over 60% compared to cold start-up [61].

The start-up rate depends on the turbine field before restart, and controlling the field is crucial in achieving optimal start-up conditions without exceeding allowable stress values [99–102]. Low metal temperatures necessitate longer heating times, which lengthen turbine start times; therefore, a higher initial temperature shortens the start time [99]. Start-up stress values are not only affected by metal temperature but are also significantly impacted by the thermal field distribution in time and space. Hence, optimising and controlling the field before restart has been identified as a critical lever for flexible turbine operations [103, 104]. Rather than having a uniform and static thermal heating with trace heating elements on a single body casing to achieve the hot standby mode, this optimisation result introduces the possibility of a dynamic pre-specified thermal field, allowing for the best restart conditions to be designed and implemented. Because the simulation accounts for the spatial and temporal conditions of operations, a solution can be obtained for every instantaneous timestep. The unique fluid flow characteristics that define thermal fields at multiple locations will be more accurately modelled, and a controlled start-up could be better designed, resulting in enhanced outcomes. This transient strategy could enable the shortening of time to start-up, significantly improving operational flexibility.

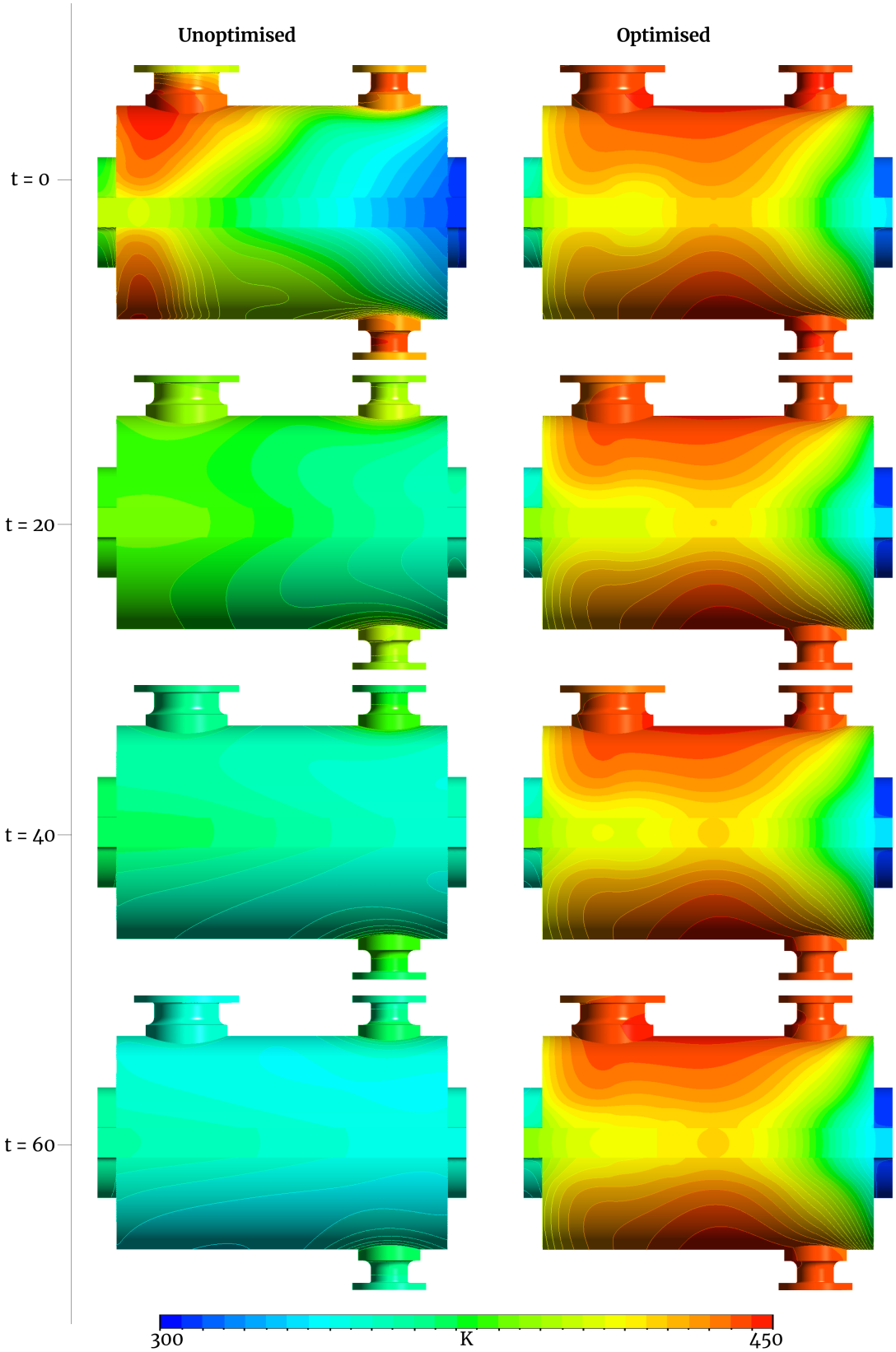


Figure 5.5: Time evolving temperatures for optimised and unoptimised cases showing a warmer casing through the entire cooling history of the optimised case, compared to the unoptimised case.

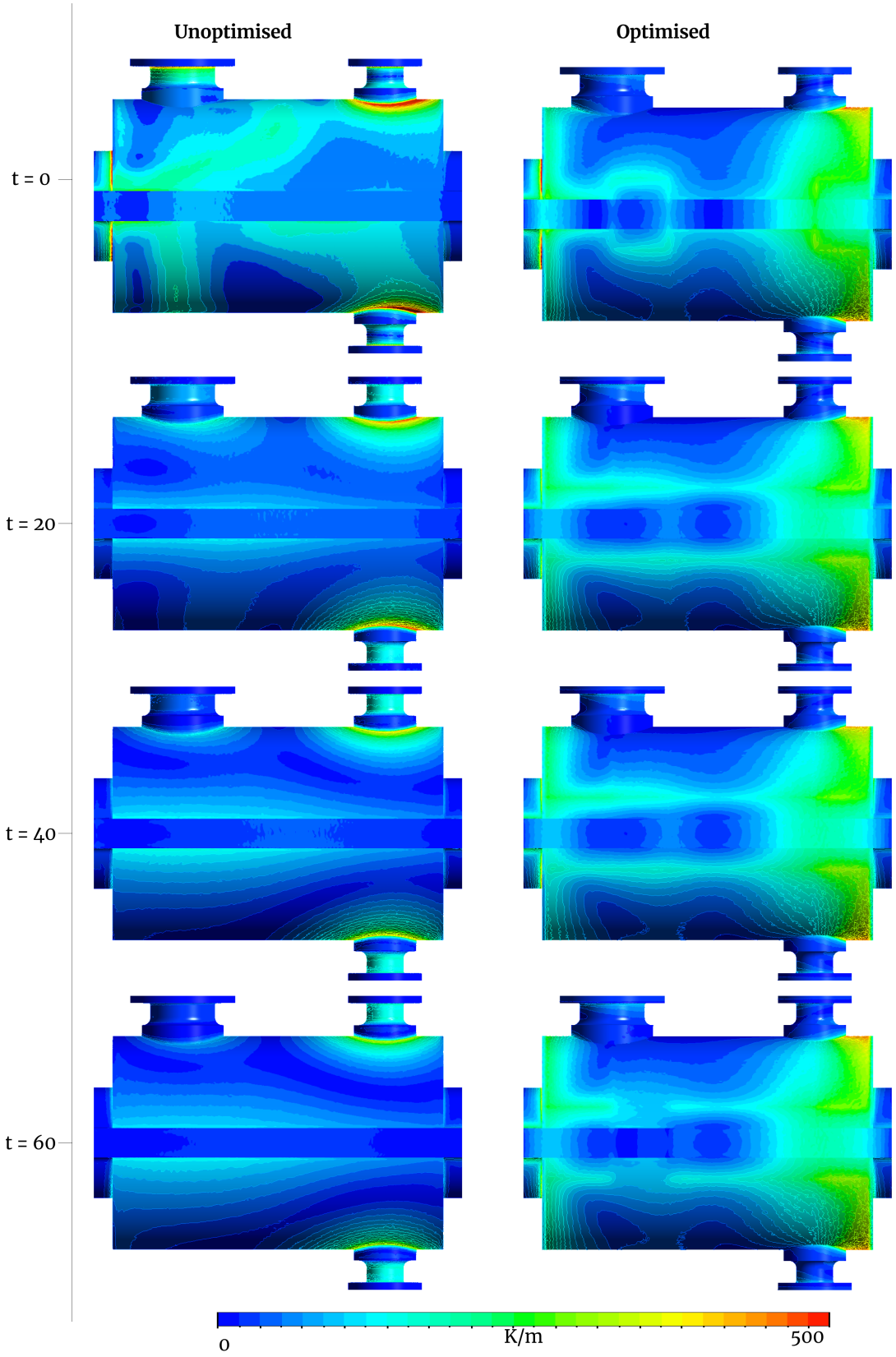
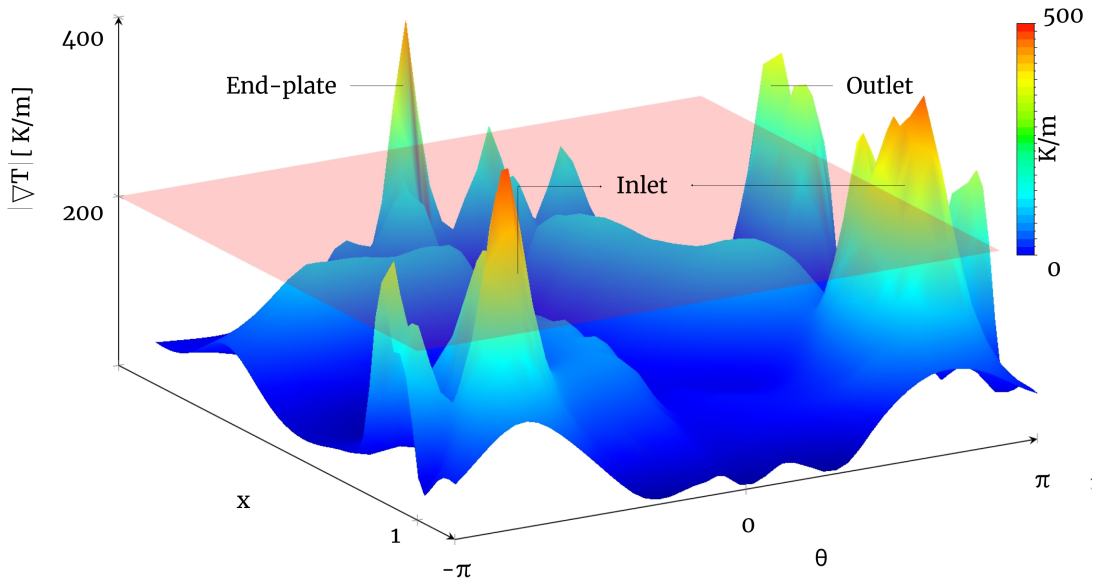


Figure 5.6: Transient thermal gradients for optimised and unoptimised cases showing the impact of actively controlled heat fluxes on the solid metal body.

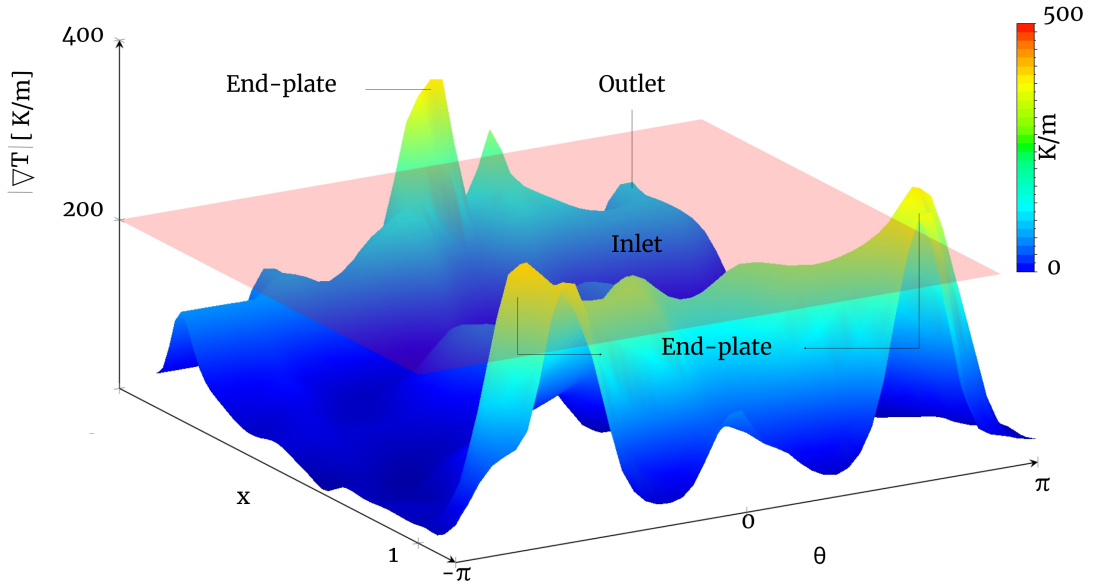
Figure 5.6 shows the thermal gradient field through the transient shutdown process for the optimised and unoptimised cases of the OTCR. Both cases exhibit different profiles. The unoptimised case shows significantly higher thermal gradients at $t = 0$, especially at the previously identified critical regions, such as the inlet, outlet, and regions of complex fluid flow patterns. The optimised case produces a more controlled thermal gradient field in these regions. Whilst the thermal gradient in the optimised case at $t > 0$ is higher than in the unoptimised case, this is a consequence of the controlled cooling process, which maintains elevated casing temperatures throughout shutdown. However, the thermal gradient at these times is below the critical threshold where thermal stress becomes a design concern. In addition, preserving higher casing shutdown temperatures between 0.4 and 0.5 of the operational temperature throughout standstill reduces start-up time by more than 60% compared to a cold ambient start [61]. The optimised thermal gradient field keeps the casing warm during shutdown and ready for rapid restart.

A detailed visualisation of the optimised thermal field is presented in Figure 5.7, illustrating the surface projection of thermal gradient distributions. Figure 5.7a depicts the unoptimised thermal gradient field, highlighting the baseline condition before the thermal gradient optimisation. The optimised thermal field is presented in Figure 5.7b, demonstrating the spatial redistribution of thermal gradients achieved through the active optimisation framework. There is a significant reduction in thermal gradient in vital thermal gradient and stress hotspots, such as the inlet, outlet, and endplate zones, with more pronounced thermal gradients and stress concentrations. The optimisation algorithm minimises the thermal gradient of regions exceeding the thermal gradient threshold of 200 $\mathrm{K\,m^{-1}}$. The spatial redistribution of thermal gradients demonstrates effective thermal stress mitigation through the optimisation of active heat flux.

Zone-specific thermal gradient plots are presented in Figure 5.8, providing an assessment of optimisation across zones. Thermal gradients in all optimised zones, excluding zones 6 and 24, illustrate a significant reduction ranging from 68% to 75% relative to the unoptimised case. In the transient analysis, thermal gradient



(a) 3D plot of OTCR casing with unoptimised thermal gradient with projection illustrated in Figure 5.1a



(b) 3D plot of OTCR casing with actively controlled and optimised thermal gradient with projection illustrated in Figure 5.1a

Figure 5.7: Surface projection of steady-state thermal gradient on the OTCR casing showing the unoptimised baseline comprising high thermal gradients at inlet, outlet, and end plate regions. The actively optimised case shows redistribution and reduction of peak thermal gradients in optimised zones.

magnitudes exhibit marginal elevation compared to steady-state optimal conditions; however, the optimisation framework maintains significant performance gains,

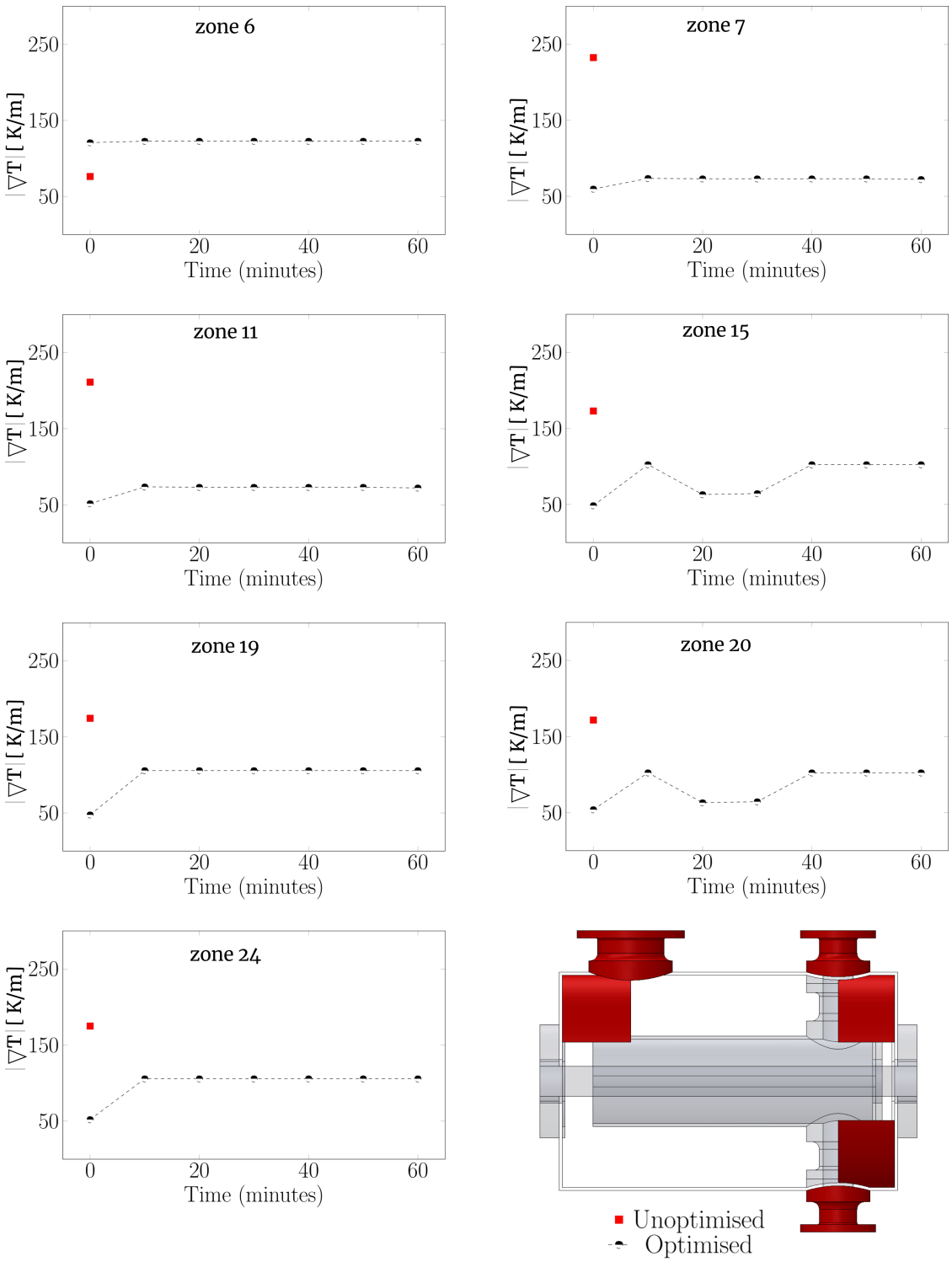


Figure 5.8: Graphs of the optimised transient thermal active thermal gradient in the optimised OTCR field plotted on the same axes as the steady-state unoptimised field.

achieving 40% to 70% thermal gradient reduction relative to unoptimised cases. This performance differential is attributed to the inherent thermal loading characteristics

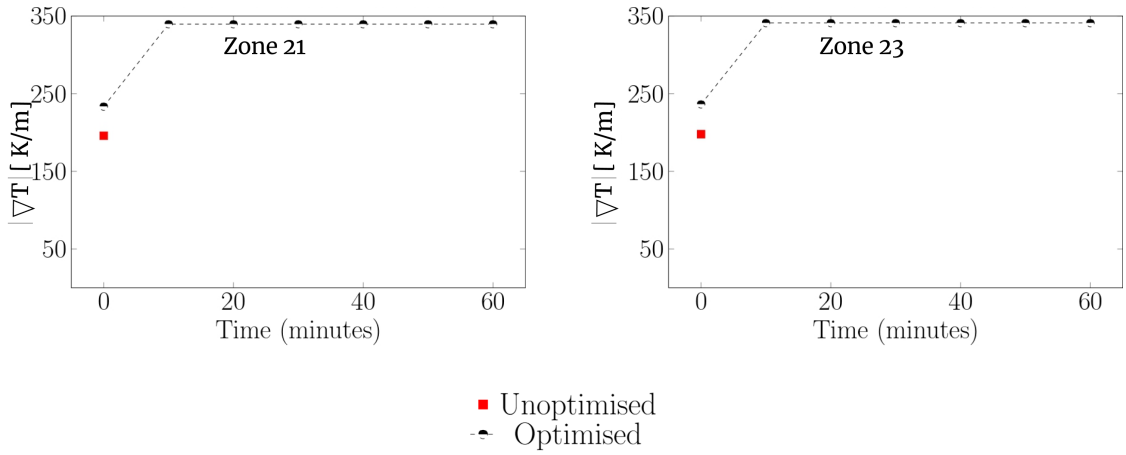


Figure 5.9: Localised increase in thermal gradient in response to external heat flux in specific zones, including zones 21 and 23. These zones illustrate the need for enhanced treatment of thermal gradients in some localised zones.

of transient operations with external heat flux, which generate elevated temperature fields compared to the natural shutdown process. The residual thermal gradients observed in the optimised transient case are consistently below the optimisation threshold of 200 $\mathrm{K\,m^{-1}}$. This result demonstrates the multi-optimisation objectives of enabling improved turbine restart capability while maintaining thermal stress levels within allowable design limits.

The thermal response to external optimum heat flux application is indicated by the localised increase in thermal gradient at the end plate-inlet/outlet interface regions, including zones 6, 21, and 23. These zones exhibit thermal gradient amplifications of 60%, 72%, and 73%, respectively, relative to the unoptimised cases. These increased thermal gradients are reflected in the projected graph in Figure 5.9, with the end plate regions showing elevated thermal gradients, relative to the casing body. The near-symmetric thermal gradient distribution observed at the inlet region is indicative of flow field symmetry between the upper and lower inlet configurations, also shown by the temperature field of the casing geometry. The similarities in properties imply that material and flow physics will yield equivalent results. This behaviour is further demonstrated by the equivalence of optimal heat flux requirements determined for the upper and lower casing halves.

The thermal gradient penalty observed in zones 6, 21, and 23 is a trade-off to the complicated and constrained optimisation problem with multiple interacting fields and variables. Without heat flux application in these zones, thermal gradients would increase due to thermal effects from adjacent optimised zones, inducing rapid temperature variations. The optimisation results in localised heating to mitigate more severe thermal gradient formation. The exclusion of end plates from the parametric optimisation domain contributes to steep temperature transitions and increased thermal gradients between the optimised casing zones and the end plates. To address this fundamental limitation and achieve comprehensive thermal field optimisation, a hybrid methodology is later proposed for enhanced control of thermal gradients.

5.1.4 Experimental Validation of Active Control Optimisation Methods

Experimental validation campaigns are conducted to validate the numerical optimisation framework through implementation of active thermal control methodologies employing the modified Oxford Turbine Casing Rig (OTCR) configuration illustrated in Figure 5.10. The experimental setup is designed to maintain functional equivalence with the computational optimisation protocol, ensuring comparability between numerical predictions and physical measurements.

The OTCR is modified with heater pads with resistive heating elements to provide controlled thermal boundary conditions. These pads enabled the precise replication of optimised heat flux distributions. This setup is modified from the steady-state experimental methodology described in Section 3.4.1. The heating elements consist of flexible silicone-insulated resistive pads with a thickness of 1.5 mm. The electrical connection is established through 20 AWG copper conductors, capable of delivering a 24 V supply voltage, with heating elements rated for a maximum power density of 1000 W/m^2. The heater pads operate as constant power density devices with predetermined resistance characteristics, leading to the assumption of constant heat flux output across the area. Figure 5.10 illustrates

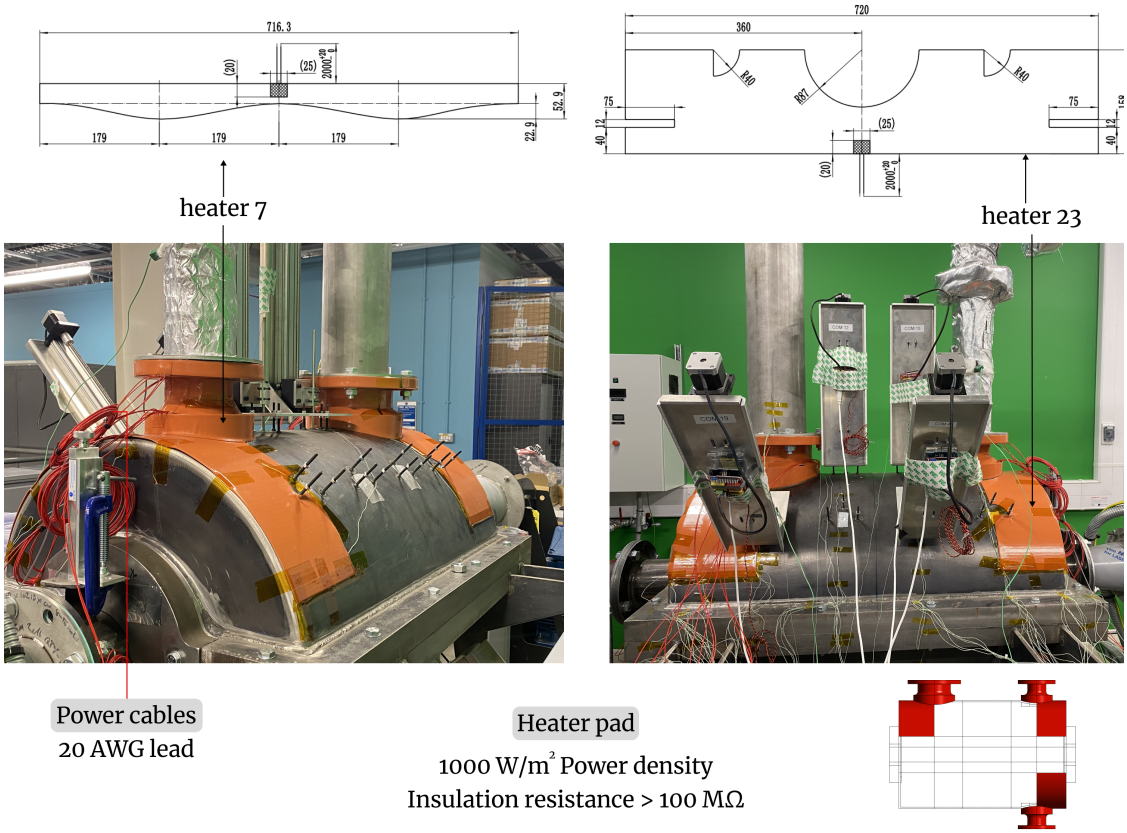


Figure 5.10: A photograph of the OTCR modified for active control validation, showing flexible silicone resistive heater pads installed on zones 6, 7, 11, 15, 19, 20, 21, 23, and 24, conforming to casing geometry, including flanges and fillets.

the detailed heater pad geometry, designed to conform to the complex OTCR surface topography, incorporating detailed geometric features to accommodate casing intricacies, including fillets, traverse mounting features, and weldments. It is essential to quantify the inaccuracies resulting from such modifications, as the implementation of active control frameworks in real turbines will involve accounting for the geometric complexities that must be modelled.

A uniform heat flux distribution is assumed on the heater pad surface. Given that only electrical power is supplied to the heaters through the voltage difference and current flow, we assume that surface heat flux $q = P/A$, where P represents electrical power in watts and A denotes the heater pad surface area. A simplification of the design assumed negligible heat flux losses due to radiation and convection to the ambient environment. Such unaccounted losses introduce measurement and

validation uncertainty, as they are challenging to measure [105, 106] and could impact the accuracy of validation. The heater placement corresponds to the specified locations of the optimisation (zones 6, 7, 11, 15, 19, 20, 21, 23, and 24).

Power is supplied through the use of power control devices that can actively control current and voltage to produce a constant output to the heaters. With a rating of 300 W and 30 V, these devices meet the electrical circuit requirements for operating the heaters. The range of the power supply units enables the tuning of power input to the heaters, allowing for the maintenance of heat fluxes at desired levels for each heater. The capabilities of the heaters, controls, and power supply units are explored in designing the experiment to validate active optimisation of thermal gradients.

5.1.5 Validation Experimental Campaign

The modified OTCR setup is used to run an experimental campaign equivalent to the optimisation framework. The experimental setup is illustrated in Figure 5.11 detailing the process of natural shutdown with the boundary and flow conditions described in Section 3.4.1. In addition to the convection boundary condition from the ambient air, heat flux boundary control conditions are implemented on the casing through the heater pads. Heat flux is derived from the power input that is controllable through the automated power supply and control unit. Table 5.2 shows the pad power configuration for the entire transient shutdown process. For each timestep, the power is preset to deliver the required heat flux with a manufacturer's error rating of $\pm 5\%$ and achieve the desired optimisation result. It is assumed that the response times for power and flux are negligible, and minimal losses are encountered during transmission through the cables and heater pads' thermally resistive elements. These theoretical assumptions are made because copper losses over the short cable distance of 2 m are minimal (approximately 1% of the power input).

The pre-computed optimal solution from numerical analysis is used to set turbine operations. The power input is dynamically changed until the end of the

shutdown process. Temperature, flow, and electrical power data are sampled and stored at a 10 Hz frequency during both steady-state and transient experimental campaigns. These stored data are then analysed with previous recorded data from the experiment, such as pad characteristics and geometry, to validate the active control optimisation framework.

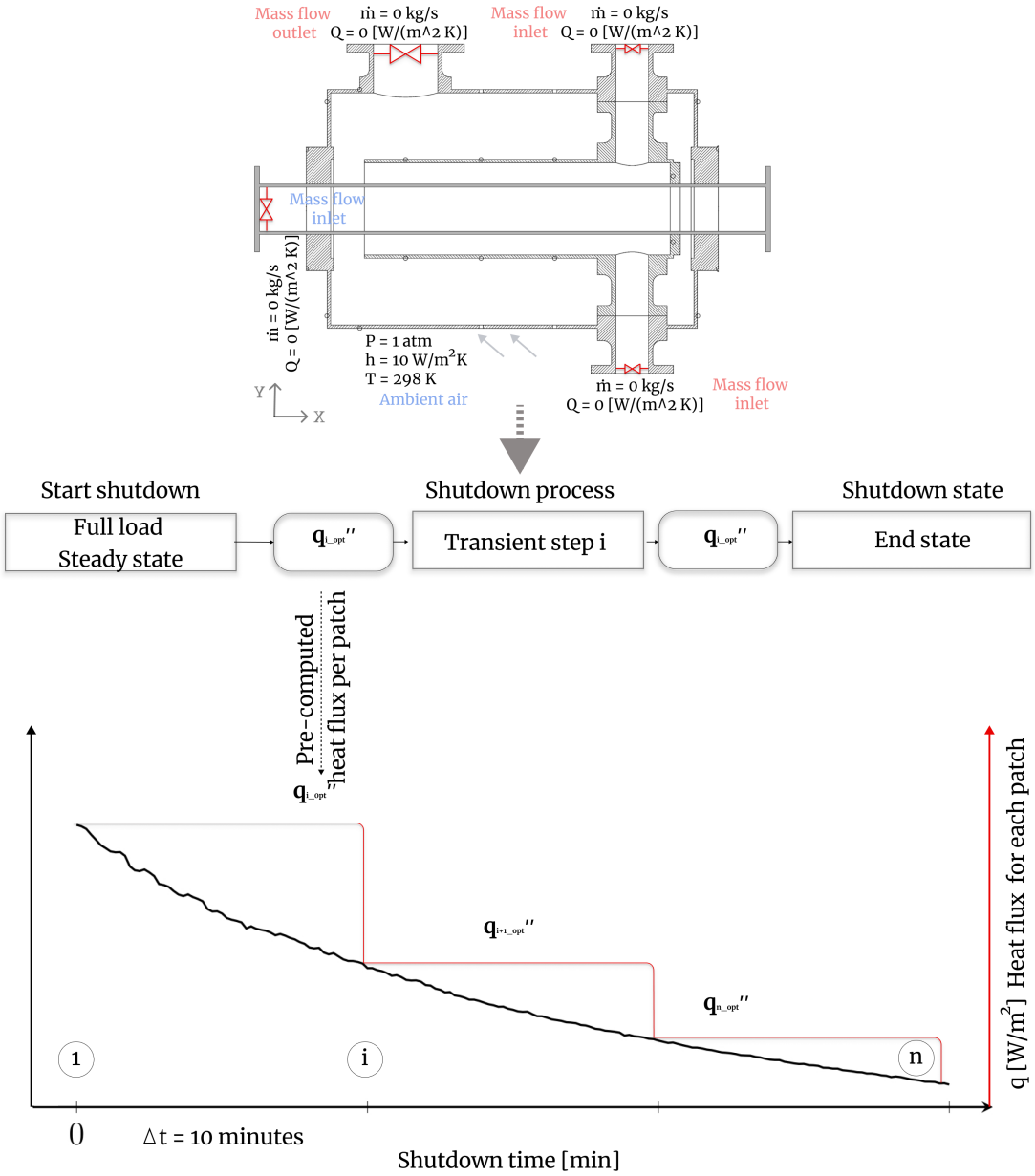


Figure 5.11: Validation experiment for transient shutdown thermal gradient optimisation framework showing the control of heat flux per the analytical optimisation solution.

Table 5.2: Heater pad power input for all heating zones during the active control validation test campaign

	Zone 6	Zone 7	Zone 11	Zone 15	Zone 19	Zone 20	Zone 21	Zone 23	Zone 24
Area [m2]	0.12	0.06	0.06	0.04	0.04	0.04	0.10	0.10	0.04
Time [min]	Power [W]								
0	46.70	63.86	63.86	34.25	34.25	34.25	40.88	40.88	34.25
10	116.75	12.77	12.77	4.28	4.28	4.28	102.20	102.20	4.28
20	116.75	6.39	6.39	4.28	4.28	4.28	102.20	102.20	4.28
30	116.75	6.39	6.39	4.28	4.28	4.28	102.20	102.20	4.28
40	116.75	6.39	6.39	4.28	4.28	4.28	102.20	102.20	4.28
50	116.75	6.39	6.39	4.28	4.28	4.28	102.20	102.20	4.28
60	116.75	38.32	38.32	4.28	4.28	4.28	102.20	102.20	4.28

5.1.6 Active Control Experiment Results

The experiment results from the optimisation campaign are presented in Figure 5.12. The polar plot illustrates temperature profiles along measurement planes C, D, and G, which constitute primary optimisation regions. Across all planes, the temperature measured in the optimised case is elevated by 20-40 K relative to the unoptimised case, consistent with the numerical analysis results. The temperature rise results from the heat flux transient conduction equations, which are explained by conductive heat transfer in transient conditions coupled with convective transport phenomena [85, 107]. While some measurement locations exhibited thermal response due to rapid conductive-capacitive and convective equilibrium, the thermal response from other locations was less significant, compensating for the temperature thermal gradient across measurement locations. In plane C, for instance, there is a pronounced thermal discontinuity in the region towards the inlet. The optimised solution has smoothed this thermal gradient. Similarly, the steep, unoptimised thermal gradient in plane G is transformed into a more uniform temperature distribution in the optimised solution with a flux distribution.

The physical measurement results validate the framework and philosophy of actively controlling the temperature field. By controlling external power inputs and heat flux, the temperature of the turbine casing is modified, achieving two aims: maintaining higher temperatures for a turbine restart and creating a more uniform temperature distribution. Such methodologies can be implemented on turbines, dynamically changing the temperatures to achieve prescribed optimisation goals. Although some experimental errors are observable, the result aligns with the expected physics, highlighting the potential to leverage such physics to solve complex, multivariate, and spatio-temporal optimisation problems. The errors analysed could affect the results. It is noticeable that the physical measurements are not perfectly aligned on the thermal profile curve due to experimental errors; however, the qualitative trend from the numerical analysis is consistent with the analytical solution, and the physically measured quantities have a deviation of less than 6% from the numerical analysis values.

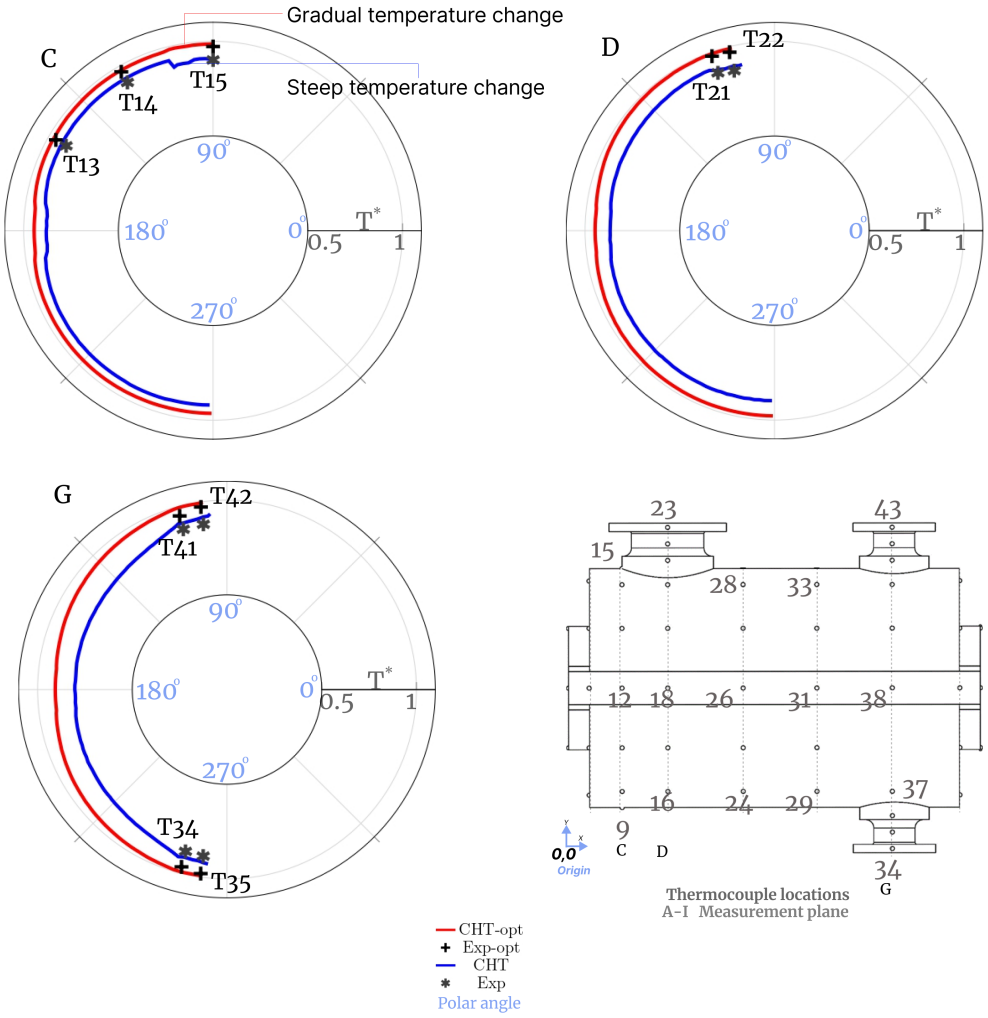


Figure 5.12: Polar plots of normalised casing temperature at planes C, D, and G comparing physical measurements and numerical predictions for the unoptimised and actively optimised cases.

5.1.7 Hybrid Active and Passive Methodology

The results of the active optimisation in Section 5.1.3 show a significant reduction in overall thermal gradient but pose a challenge in some regions where the thermal gradients increased due to the rapid change in temperature with adjoining end plate walls. This section examines methods for minimising the thermal gradients and compensating for the optimisation penalty associated with the active control method. The principle of electrical equivalence of thermal circuits in resolving conductance and heat flow is adopted in this approach.

As described by the thermal network model analysis, thermal models are

converted to electrical models by converting the characteristic length and thermal conductivity of solid bodies into resistances, which allow or impede the flow of heat flux when a temperature differential is created. This system, similar to electrical circuits, creates the possibility to resolve complex thermal circuits electrically [24]. The electrical equivalent correlation of thermal resistance is $R_c = L/kA$, where L is the length, k is the thermal conductivity, and A is the cross-sectional area. Therefore, for equivalent lengths and areas, a higher thermal conductivity material will have lower resistance to heat flux and exhibit a lower thermal gradient when exposed to external heat on its surface. Some materials, such as copper and graphite, have been identified as possessing high thermal and electrical conductivities, and multiple studies have shown how to utilise them as thermal bridges for thermal management systems [108–110]. These materials have thermal conductivities of 400 $\mathrm{W\,m^{-1}\,K^{-1}}$, up to 8 times higher than the conductivity of steel. Therefore, they could exhibit far less resistance to heat flux transfer than steel, leading to better thermal performance [111].

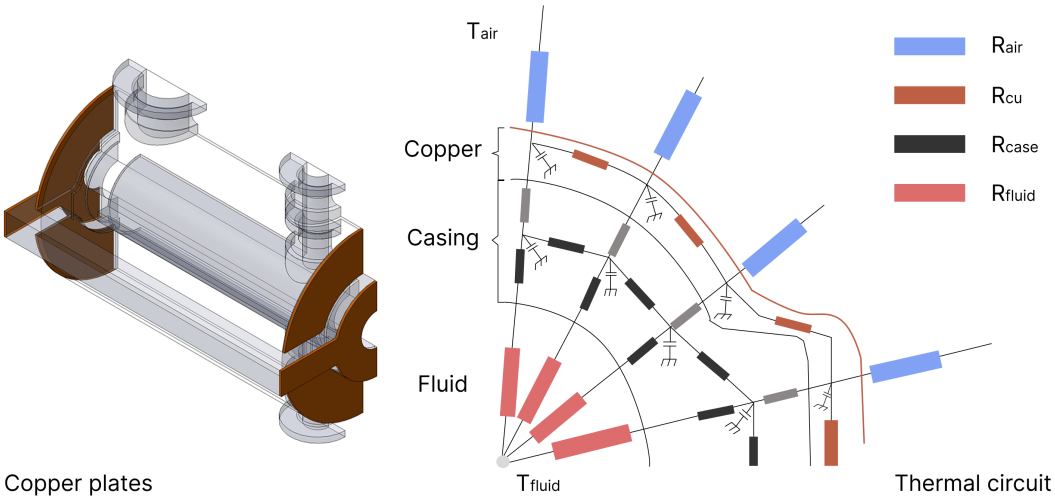


Figure 5.13: Thermal resistance network for the passive copper bridge methodology, with an electrical circuit analogy showing the reduced effective resistance of the steel-copper composite at end plate regions, where copper reduces the thermal gradient relative to steel alone.

This thesis explored the potential role of thermal bridges, such as copper, in mitigating the thermal gradient observed in sections of the casing. As shown

in Figure 5.13, the regions of focus are the endplates where the active thermal optimisation required complementarity. For these regions, the hypothesis was to place thermal bridging copper to aid in the distribution of temperature fields and guarantee a reduced thermal gradient. The premise is that, as with the circuit equivalent of the thermal field shown in Figure 5.13, the thermal resistance from the copper is smaller than that of steel and effectively reduces the thermal gradient in all directions of the steel due to the resolution of complex resistances by reduction of equivalent circuits [112, 113].

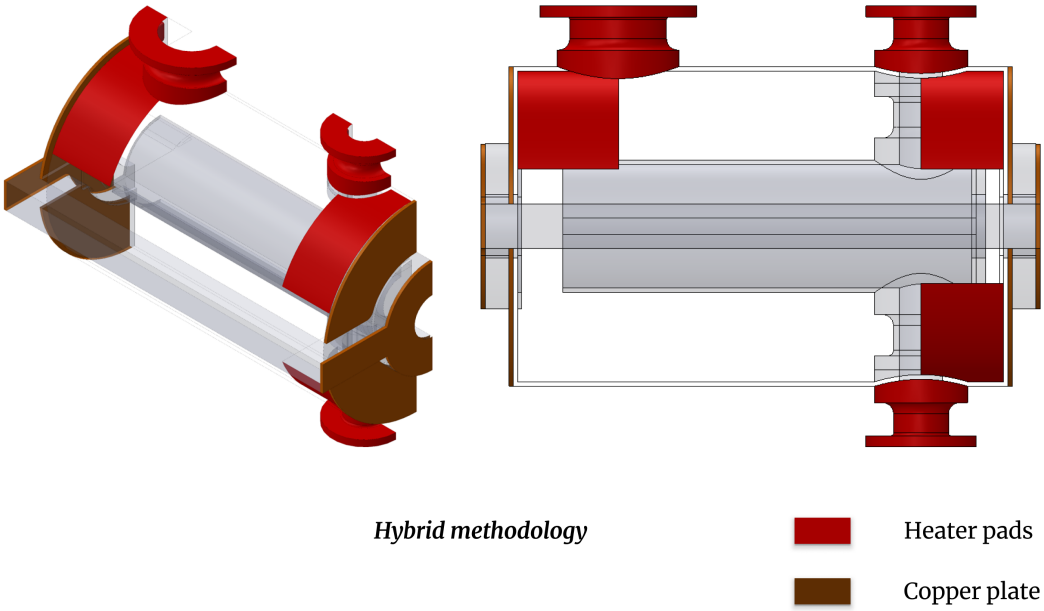


Figure 5.14: Hybrid active–passive control configuration showing the heater pad zones (red patches) and the copper thermal bridge placement (brown regions) on the end plate regions of the OTCR casing. Copper bridges are added exclusively at the end plate locations shown, and no copper is applied elsewhere on the casing. 8 mm copper shell thickness is used, determined from the passive optimisation.

The passive control method is superimposed on the active methodology to achieve robust results in thermal gradient reduction. Copper is simulated on the steel casing to form a steel-copper interface, thereby reducing the thermal barrier to heat flow. Enabling more efficient thermal flow and a more uniform temperature distribution, due to the reduced effective thermal gradient of the equivalent circuit, is critical to reducing thermal gradients. Figure 5.14 illustrates the hybrid active–passive system.

Increasing the thickness of the copper thermal bridge initially reduces $|\nabla T|$ but eventually yields diminishing returns beyond an optimal thickness [114]. Two competing effects define the total thermal resistance. The copper bridge reduces the effective steel resistance by providing a parallel conduction path, whilst simultaneously increasing its own resistance as $R_c = t_c/(k_{\text{copper}}A)$. The theoretical minimum gradient therefore corresponds to the thickness at which the combined steel–copper resistance is minimised, and is strictly greater than zero since $R_c > 0$ for any finite copper thickness.

Copper thickness optimisation is performed using the PyFluent environment on a CHT case of the OTCR. The copper shell thickness is parametrised across the design space $t_c \in [0, 8]$ mm and optimised using the Bayesian optimisation library to determine the thickness that minimises $|\nabla T|$. All end plate zones yielded an optimum copper thickness of 8 mm. The copper is modelled as a shell layer on the steel casing with material properties including, thermal conductivity $k = 401\ \mathrm{W\,m^{-1}\,K^{-1}}$, thermal diffusivity $\alpha = 111 \times 10^{-6}\ \mathrm{m^2\,s^{-1}}$, specific heat capacity $c_p = 385\ \mathrm{J\,kg^{-1}\,K^{-1}}$, and density $\rho = 8960\ \mathrm{kg\,m^{-3}}$ [66].

The optimisation model varies the copper thickness in discrete increments of 1mm and solves for the thermal gradient to determine the best thickness functions as in Equation 5.8.

$$\min_{t_c} \quad J = |\nabla T| \tag{5.8}$$

$$\text{where:} \quad |\nabla T| = \text{PyFluent}(t_c,\, BC,\, IC) \tag{5.9}$$

$$\text{subject to:} \quad t_c \in [0, 8]\ \text{mm} \tag{5.10}$$

$$t_{c,i} = \text{copper thickness for zone } i$$

Figure 5.15 illustrates the change in thermal gradient with increasing thickness of copper shell attached to the casing. The diminishing marginal reduction in the thermal gradient is described with increasing copper thickness. The thermal gradient decreases more rapidly with an increase in initial copper thickness. Using the PyFluent solver and Python, the process of setting copper shell properties and

thickness parametrisation, as well as optimisation, is performed. The optimisation on the hybrid case is done only for the steady-state condition, using the active optimised steady-state case.

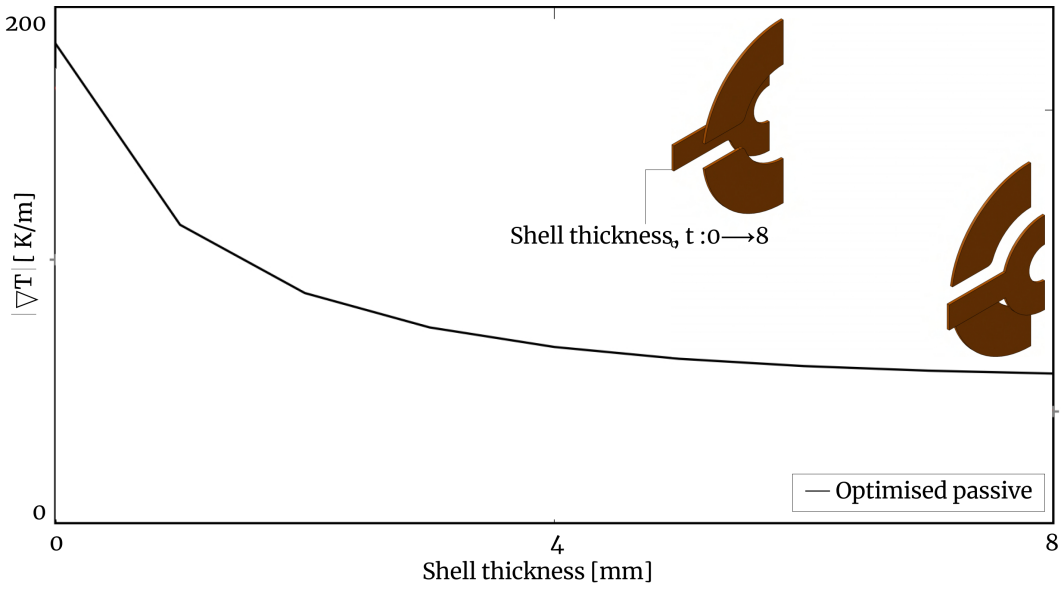


Figure 5.15: Thermal gradient magnitude $|\nabla T|$ of the OTCR end-plates as a function of copper shell thickness t_c, showing diminishing returns with increasing thickness.

5.1.8 Hybrid Optimisation Results

The hybrid optimisation temperature field is shown in Figure 5.16. Compared to the active case, the addition of copper to the end plates conducts heat away from the hot inlet and outlet regions, producing a different temperature distribution by reducing the effective thermal resistance across the end plates. This reduction of gradient in the end plate regions allows the active heater pads in adjacent zones to operate at similar heat flux levels whilst achieving superior overall gradient reduction. Figure 5.17 depicts the resulting thermal gradient from the hybrid optimisation. It compares the thermal gradient output from the unoptimised, active optimisation, and the hybrid methods. The hybrid optimisation result shows an improved thermal gradient profile with reduced thermal gradients in most regions, including the end plates. This solution addresses the optimisation challenge in the active control scenario.

Figure 5.18 shows the zones where active optimisation induced increased thermal gradients. For all these zones, the hybrid methodology has significantly reduced the thermal gradient by as much as 80%. Zones 1 and 3 of the endplate, as well as zones 21 and 23 of the inlet region, experience the highest decline in thermal gradient. Zones 1 and 3 initially faced the challenge of the thick wall split flanges, as well as the cold shaft, where energy exchanges cause high thermal gradients. They are also complicated due to the complex fluid flow patterns, including turbulent and recirculating flows, that occur before they exit the turbine. In zones 21 and 23, the phenomenon is unique. The casing end plate is slightly colder due to the reduced energy exchange between fluid and solid, while the inlet is significantly hotter. By applying optimum copper thermal bridges, we can equalise the temperature field between hot and cold regions more effectively.

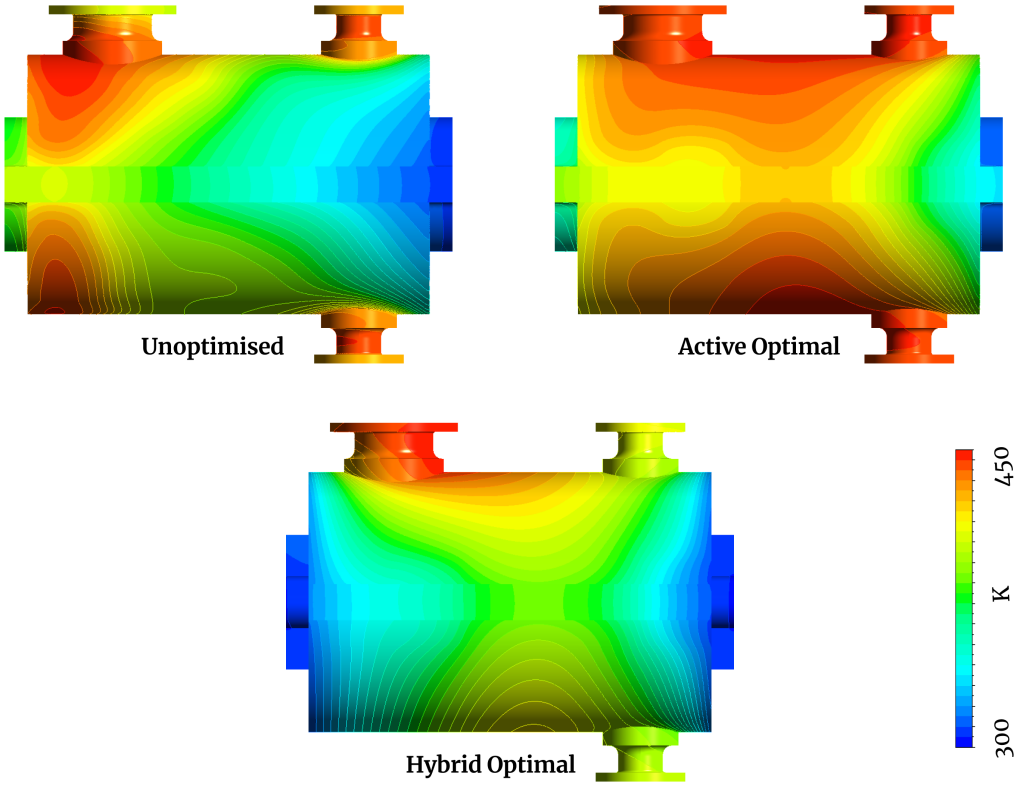


Figure 5.16: Optimal temperature field resulting from hybrid active and passive control methodologies

The hybrid control methodology demonstrates effectiveness in addressing conduction and convective dominance-induced thermal gradients in turbines. Reducing the thermal gradient on the entire casing is a significant step towards reducing thermal stresses. It is instructive to note the multi-objective role of the casing, acting not only as a static structural member but also as an active control member with sub-units that play vital physics roles from heating to thermal redistribution.

5.1.9 Operationalising Optimisation and Control Strategies

Turbines should be operated dynamically to leverage the functionalities of these novel hybrid thermal gradient optimisation and control systems. Because the real-time operations of turbines are complex, with changing fields as load changes and varying fluid flow conditions, real-time monitoring and control are essential. The control and optimisation strategies discussed can be implemented rapidly with fast computer processors, making it feasible for turbines to be optimised in real time by enabling critical components, as explained in Section 4.3.1. When pre-computed optimised solutions are determined, they form the operational target condition for turbines. During operations, live feedback could then be tuned based on reconstructed data and changing operating conditions.

Figure 5.19 shows a modified plant control framework for flexible operations. Live plant measurements, high-fidelity solutions, active and passive control, boundary conditions, stress and clearance analysis, and visualisation are critical to ensuring the systems operate within the limits of engineering design. This thesis has made contributions to these tools, enabling the use of live plant measurement to develop and validate numerical analysis data, while ensuring the accuracy of novel solvers.

Data field reconstruction is another critical aspect required to complete the operating framework. When a physical plant, such as the OTCR, is operating, measured data can be reconstructed as the inputs to novel thermal gradient solvers used for thermal gradient and stress optimisation and control to maintain plant integrity. To explore the feasibility of the operational model, a data field reconstruction was implemented using the steady-state optimisation data of the

OTCR. Fifty-one sensor locations are mapped into the full high-fidelity domain of the thermal field through the latent space, as shown in Figure 5.20. Figure 5.21 shows the reconstructed field representing the numerically derived high-fidelity field. The autoencoder method uncovers a compressed latent space to reconstruct high-resolution fields [15].

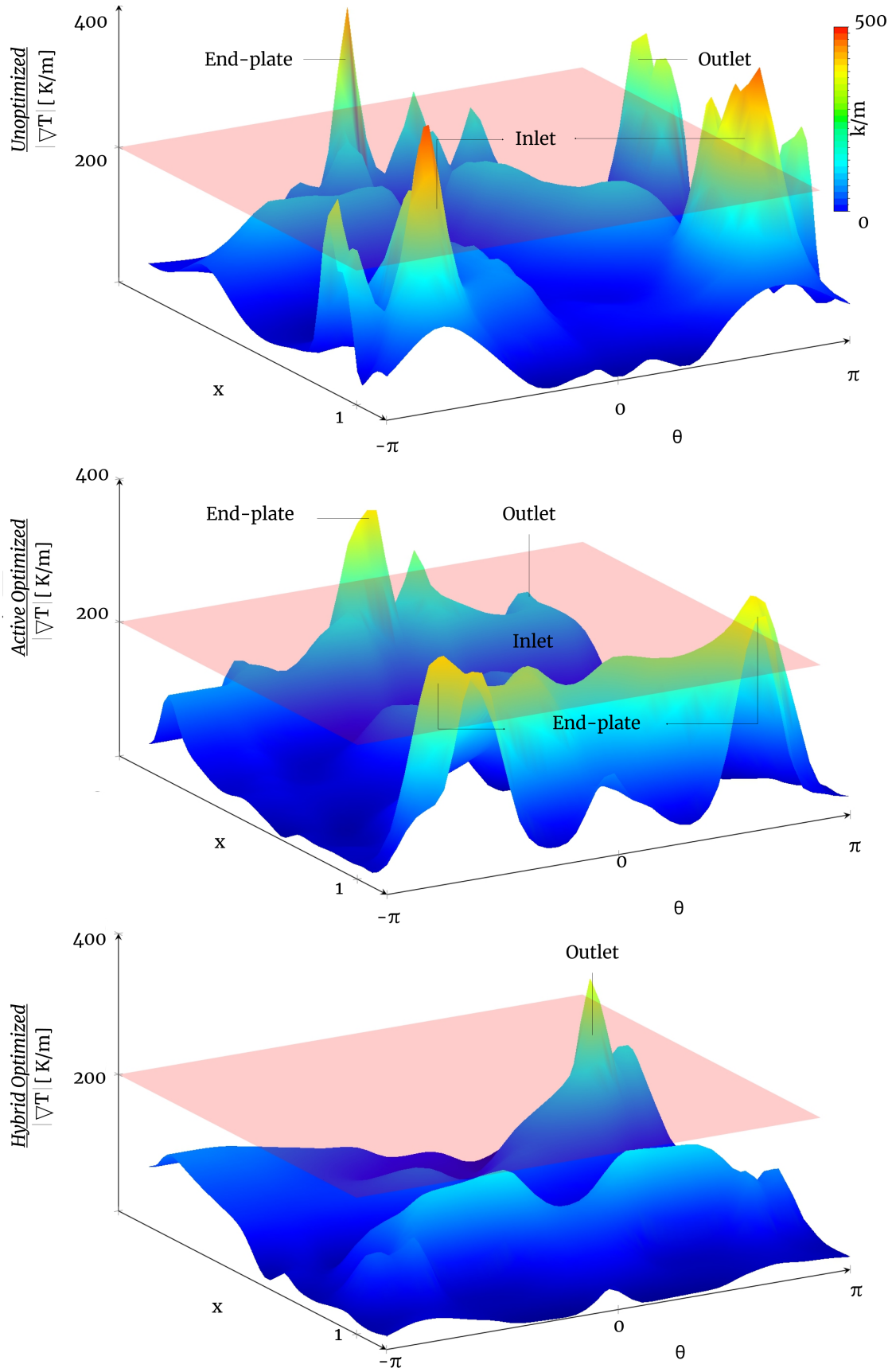


Figure 5.17: Optimal thermal gradient resulting from hybrid active and passive control methodologies reflecting a reduction in thermal gradient in most casing regions for the hybrid control method.

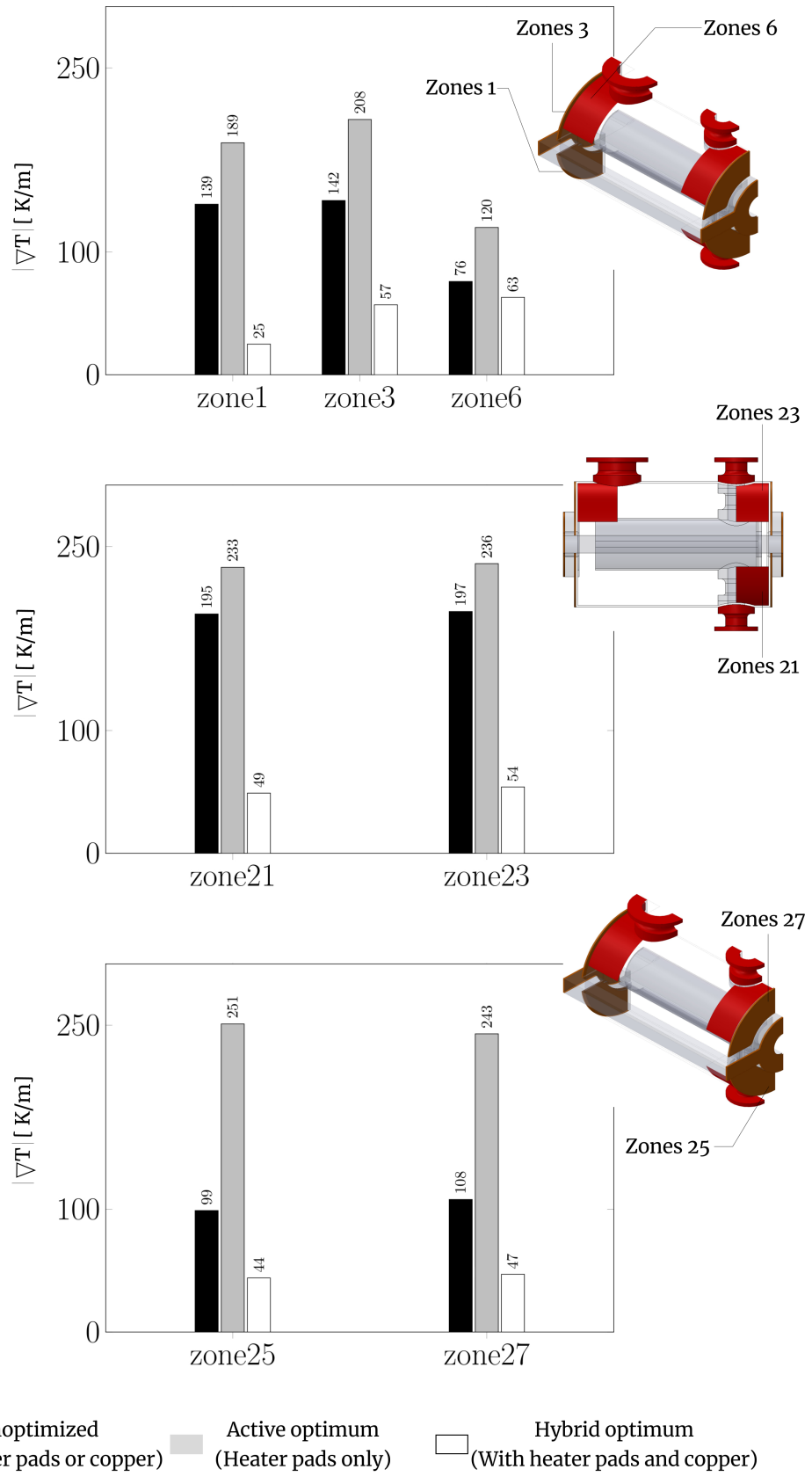


Figure 5.18: Zone-wise thermal gradient reduction achieved by the hybrid active-passive optimisation relative to the unoptimised baseline and active-only case. Hybrid optimisation achieves an overall reduction of up to 80%.

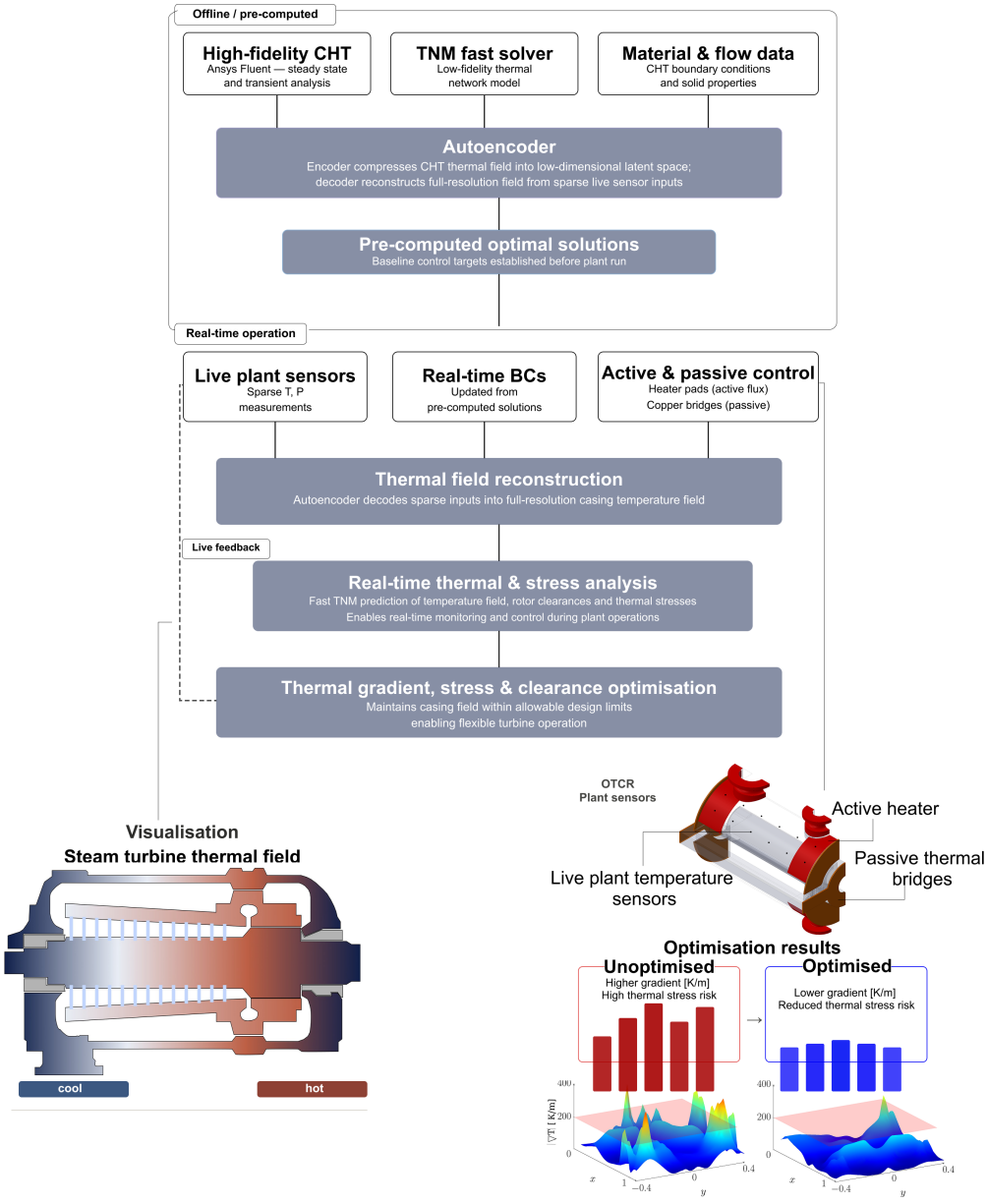


Figure 5.19: The proposed real-time plant thermal optimisation and control framework, integrating pre-computed high-fidelity CHT solutions, live sensor measurements, TNM fast solver, field reconstruction via autoencoder, and active/passive control outputs for thermal gradient and stress management.

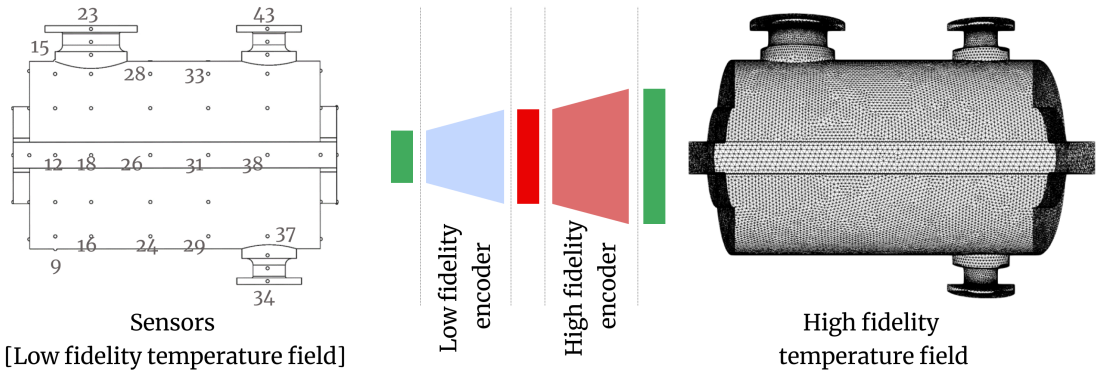


Figure 5.20: Sensor placement strategy for thermal field reconstruction from 51 thermocouple locations on the OTCR outer casing mapped into the latent space of the autoencoder for full-field temperature reconstruction and real-time input to the turbine field optimisation and control.

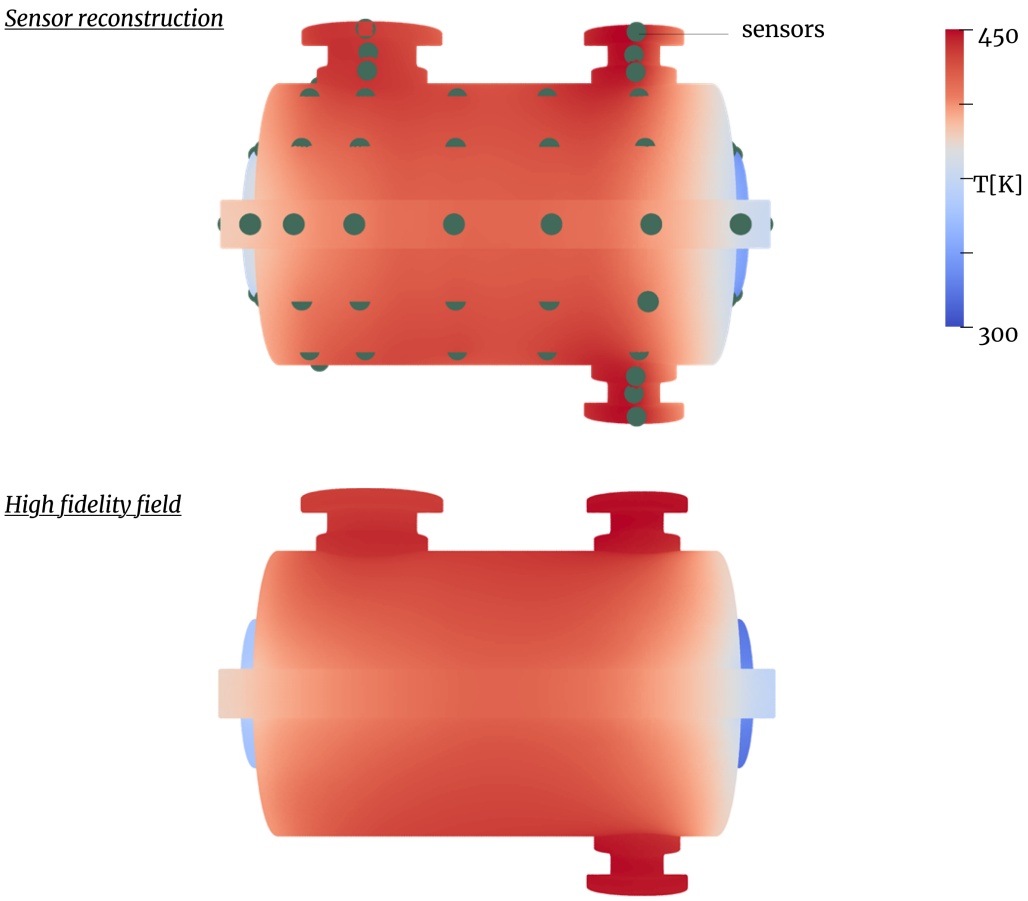


Figure 5.21: A comparison of the autoencoder-reconstructed temperature field from 51 thermocouple sensor inputs and the high-fidelity CHT reference field, demonstrating the applicability of the data-driven field reconstruction method for real-time control applications.

5.2 Summary

This chapter presents thermal gradient optimisation methodologies to minimise thermal gradients on the casings of power-generating turbines. It starts by identifying the thermal gradient critical positions on the casing and develops intelligent frameworks to optimise the thermal gradients, achieving overall thermal gradient reduction.

Active control methods are proposed that employ external heat flux to control the thermal boundary conditions on the casing. The optimisation framework utilises the PyFluent environment due to its ability to automate complex problems and leverage highly developed optimisation libraries for such complex multi-objective cases. 70% thermal gradient reduction is achieved in most regions. In some regions, such as the end plates, a sharp temperature change creates a thermal gradient.

To address the challenges, a hybrid active and passive methodology is introduced. The passive methodology utilises highly conductive copper as a thermal bridge to reduce the effective resistance to heat flow and control temperature distributions. The hybrid optimiser further enhances the optimisation results, yielding a near 80% reduction in overall thermal gradient.

Physical measurements experiments are conducted to validate the active numerical analysis. Heater pads are designed and used to replicate heat flux boundary conditions. Automated controls are designed to regulate power and flux inputs according to the boundary conditions. The physical measurement results correspond to the expected trend from the numerical analysis.

Lastly, this chapter introduces how to operationalise these methodologies. It proposes a new framework that incorporates live plant measurements and a pre-computed high-fidelity simulations. High-fidelity optimisation methods are executed before the plant run. During plant operations, these pre-computed solutions serve as a baseline around which the plant optimiser can be tuned to achieve the best results.

6
Conclusion and Outlook

This thesis presents a new design and operational philosophy to enable the flexible operation of power-generating turbines. It further presents methodologies to operationalise the novel design philosophy. It demonstrates active and passive thermal gradient control strategies to minimise thermal stresses on power turbines, a requirement for flexible power generation systems.

The flexible operation of power-generating systems is crucial for the world's evolving energy mix. To mitigate the impacts of climate change, the renewable share of the global electricity mix is projected to reach 97% by 2050. This significant share of clean energy is then impacted by the intermittency of clean energy sources, which presents the challenge of grid instability that must be compensated for by flexible operations of conventional power systems. However, the current design of power-generating turbines with static functioning casing [up to 150 mm thick], operating at high temperatures [over 600 K] and pressures implies that they are best suited for baseload operations with minimal cyclic operation. Repurposing these plants for the flexible operations required for modern energy systems results in operational penalties and expensive damages from high thermal stresses, casing deformations, clearance limitations, and the cat's back effect.

While significant effort has been made to address the challenges of operational flexibility, including the development of fast solvers to enable the optimisation and

control of thermal fields, these efforts are either localised or lack physical validation. They also suffer from unvalidated black-box fluid physics. The fluid properties of turbines are highly complex due to the intricate fluid flow physics, which occur during operations and in shutdown mode, resulting in high computational costs and uncertainties in determining thermal fields. Even when turbines are modelled, the limitations of validation tests make it impossible for the solutions to gain the trust of the industry for adoption. This reality hinders the advance of turbine technologies and restricts operational flexibility. This limitation could be very costly for the world in the form of impeded penetration of clean energy, resulting in unchecked warming and substantial economic costs, or high energy insecurity if intermittent clean energy continues to grow unabated and conventional plants are not redesigned to meet new requirements.

The evolving requirements for power turbines make the substance of this thesis vital. It presents models and methods to transform the operating philosophy of turbine components from mere structural features to multi-functional active optimisation systems to control turbine thermal properties. It presents a novel facility to enable physical experiment designs for validating new solvers, technologies, and numerical analysis methods. The OTCR facility comprises the solid domain, outer and inner casings, and shaft, as well as the fluid domain, which includes hot and cold air that replicate working fluids and energy exchanges in turbines. The facility is uniquely equipped with high-resolution instrumentation in both the solid and fluid domains, featuring 84 thermocouples and 4 traverses that can take over 100 unique fluid measurements. It can characterise unique casing thermal and flow fields and is retrofittable for future advanced tests, such as gland steam tests, during complex shutdown regimes. The facility's characteristics are replicable on real turbines due to the matching dimensionless Grashof and Richardson numbers based on MHI-provided data.

Hybrid numerical analysis and physical measurements are conducted to calibrate and cross-validate the facility. Steady-state full-load and transient shutdown conditions are simulated, and the corresponding experiments are designed to measure

complex turbine fields and properties. High- and hybrid-fidelity CHT and TNM methods are demonstrated for the numerical analysis. The facility provides accurate measurement and validation results across solid and fluid domains. Normalised steady-state and shutdown measurements result with a $\leq 5\%$ deviation compared to numerical analysis. Accurate traverse fluid domain measurements in multiple planes have a $\leq 2\%$ deviation from the numerical analysis. The confidence from physical measurement leads to the exploration of the results for hybrid solvers. Thermal network models are implemented for steady-state and fast-transient shutdown problems. Automated data transfer across solver fidelities, hybrid-fidelity meshes, field reconstruction, and timestepping enabled a rapid and reliable solution of complex thermal problems. The ability to solve thermal shutdown fields in real time is identified as a crucial condition for the real-time optimisation and control of turbine fields. Hybrid fidelity models, enabled by accurate validation from the OTCR, make such real-time tests a possibility.

This thesis further demonstrates novel control methodologies to minimise thermal gradients and stresses on turbine casings. Because the high thermal gradients on the resolved field could pose thermal stresses and lead to engineering failure, novel methods are explored to mitigate them. First, an active control method is implemented by applying an external heat flux to the turbine casing, actively modulating the temperature fields and controlling thermal gradients. By dynamically discretising the casing into 27 sub-components and utilising new optimisation methods that rely on high-accuracy numerical analysis, steady-state and transient thermal gradient reductions of up to 75% were achieved. Physical tests are implemented to validate these methods on the OTCR. New experiment regimes are designed to replicate the optimisation methods, validating the numerical analysis results.

Hybrid optimisation, which superimposes passive methods using highly conductive copper materials as thermal bridges, is implemented to reduce thermal resistance to heat flux effectively. The combined results of active and passive control measures yield an 80% reduction in thermal gradient compared to the baseline,

unoptimised cases. For power-generating systems where turbine thermal stresses limit operational flexibility and threaten energy security, a dynamic approach to turbine design is crucial for addressing these challenges. Active and passive control methodologies are enabled by reimagining the design function of system components. By utilising the turbine casing as a control system, rather than merely a structural unit, and splitting it into discrete blocks, the system can be intelligently enhanced with novel physics and optimisation methods, thereby significantly reducing thermal degradation. Hence, the operational flexibility of turbines is enabled by flexible and dynamic designs, paving the way for the future of energy systems.

6.1 Outlook

The results demonstrated in this thesis could lead to the unbounding of multiple research areas in turbine power generation. Having demonstrated the reduction in thermal gradients, detailed thermal stress analysis could be carried out both numerically and through physical measurements. Further stress analysis provides confidence for the industrial application of these novel optimisation methods on real turbines. The OTCR provides this capability through the retrofitting of displacement and laser probes that can measure thermal expansion and stresses at elevated temperatures and under cyclic operations. The facility could replicate fast start-ups and shutdowns, including cold and warm starts with sporadic ramps to measure the thermal impacts.

With an improved understanding of turbine casing thermal stresses and a validated framework to optimise thermal fields, further advances in plant operational flexibility should be pursued. Active control methods with heater pads rated for steam-turbine operating temperatures should be adopted for industrial applications to control thermal gradients and stresses within material design limits, ensuring safe transient operations. Thermal bridge materials beyond copper could also be explored. A trade-off between thermal conductivity, availability, and cost is needed to identify the most effective passive control solution. Installations similar to those demonstrated on Siemens industrial turbines [61] could be implemented

using the optimisation methods developed here and improved heater-zone control. It is useful to assess whether composite casing materials with tailored through-thickness conductivity could be designed to passively homogenise thermal fields without retrofitting.

However, even with the new methods developed, the fast thermal analysis of much larger turbine systems remains a limiting factor. Rapid and accurate numerical analysis methods must be developed and advanced. Fast data transfer and field reconstruction, coupled with novel optimisation methods, unlock the possibility for real-time optimisation of the thermal field on the OTCR and any real turbine facility. Improved fluid domain analysis could be integrated with the OTCR facility as a calibration tool to ensure future fast solver accuracy. Sensor optimisation can enhance data fidelity and efficiency. Digital twinning systems with fast solvers can reconstruct measured data, which can then be optimised in real time by new optimisation solvers to control stresses and clearances, thereby eliminating the black boxes that hinder turbine technology advances. The tools required for flexible operations can now be better developed and tested. Numerous opportunities exist for rapid technological evolution to create an energy-secure and sustainable world while mitigating the challenges of energy intermittency posed by clean energy sources.

Beyond the casing, further research is required. From the gland steam process, to monitoring the rotor bladed path to assess and control clearances, which is another limitation to flexible operations. The transverse deformations and unequal expansions between rotating and static components are a critical concern that should be modelled and validated. The OTCR enables future implementation of gland seals and a bladed path to advance this research. With such retrofits, more experimental campaigns such as shutdown vacuuming can be conducted to further validate complex fluid flow regimes and their impacts on thermal fields and optimisation methods. Further research on the OTCR platform can be conducted to measure and predict clearances between the bladed path and stationary components, such as the casing, using contact measurement or non-contact laser sensors. Reliable prediction of clearance is crucial for flexible turbines, where rapid start-stop cycles are inevitable,

and clearance gaps change intermittently, with high clearance reducing efficiency through leakage losses and blade-tip contact causing component wear and failure. The retrofittable gland steam fitting of the OTCR could integrate gland steam flow and simulate the mixed-convection shutdown regimes described in Chapter 1, enabling simultaneous monitoring and active control of the thermal and flow fields during vacuum conditioning, which is not currently available on the OTCR.

In summary, power turbine and grid designs should be studied from the perspective of the overall system and functional efficiency, rather than narrowly focusing on turbine efficiency. For instance, with the abundance of clean energy sources, the sun generates a tremendous 44 PW (10^{16}) W [115]. The 3 TW electricity consumption is a mere 0.006–0.007% of the solar potential. Even the total energy consumption of 186,000 TWh only amounts to 0.05% of solar energy potential [116]. Considering other clean energy sources, such as wind, further highlights the abundance of energy available on Earth. The path to utilisation is therefore critical. To this end, the efficiency target of power generation could change from the efficiency of converting limited fuels to the efficiency of converting abundant, clean energy that would otherwise be wasted. Rather than designing plants with the aim of high fuel conversion, high energy utilisation might be a more suitable objective. Such plants could flexibly switch between high-energy-dense fuels and intermittent clean energy, changing the energy margins and reducing long-term variable costs due to the low cost of clean energy. Aside from the already itemised flexibility requirements, such plants and power systems should leverage machine learning for generation and load prediction for plant scheduling and energy dispatch. The ability to monitor demand and supply in real time and to plan the overall system's generation mix enables the potential to achieve significant results with power systems. If the system prediction for intermittent renewables and load is accurate, prior optimisation planning of the flexible system should be developed to limit the possibility of thermal stresses that impact plant operations, maintaining energy security. This new approach to addressing energy challenges could be crucial to meeting the global need for decarbonisation. The prospects warrant further investigation.

6.2 Publications

- **Accepted/published papers**

  1. Nwangele, Chukwuemeka G., Mark Baker, Koichi Tanimoto, Ryo Egami, and Budimir Rosic. “Enabling Operational Flexibility of Power Generation Systems: Novel Experimental Facility for Characterisation of Turbine Casing Thermal Field.” Journal of Engineering for Gas Turbines and Power, ASME, doi:10.1115/1.4069607.

  2. Nwangele, Chukwuemeka Godwin, Mark Baker, Koichi Tanimoto, Ryo Egami, and Budimir Rosic. "Enabling Operational Flexibility of Power Generation Systems: Novel Experimental Facility for Characterisation of Turbine Casing Thermal Field." Turbo Expo. Vol. 88834. American Society of Mechanical Engineers, 2025.

  3. Nwangele, Godwin Chukwuemeka, Mark Baker, Koichi Tanimoto, Ryo Egami, and Budimir Rosic. “Enabling Flexible Power Generation Systems: Experimental Facility and Novel Numerical Tools for Thermal Field Optimisation.” Proceedings of Global Power and Propulsion Society (GPPS Shanghai25), 4–6 Sept. 2025, Global Power and Propulsion Society, Paper GPPS-TC-2025-0237.

  4. Enabling Operational Flexibility of Power Generation Systems: Novel Active and Passive Thermal Field and Gradient Optimisation - This paper offers the active and passive methodology for the discretised optimisation of thermal fields to reduce thermal gradients and stresses of power-generating turbines to enable operational flexibility.

     Accepted for ASME Journal of Engineering for Gas Turbines and Power, 2026

- **Planned publications**

1. Enabling Operational Flexibility of Power Generation Systems: Future Power Plant Design Based on Novel Design and Operational Philosophy- This paper will offer a new power turbine design philosophy, highlighting the need for a design shift from static components to active control systems. It will use the OTCR and its consolidated results as a case study on how to operate plants flexibly.

   Proposed Journal -Applied Thermal Engineering

References

[1] Hannah Ritchie and Pablo Rosado. "Electricity Mix". In: *Our World in Data* (2020). https://ourworldindata.org/electricity-mix.

[2] IEA. *Global Energy Review 2025*. Licence: CC BY 4.0. Paris, 2025. URL: https://www.iea.org/reports/global-energy-review-2025.

[3] International Energy Agency. *Energy and AI*. Licence: CC BY 4.0. Paris, 2025. URL: https://www.iea.org/reports/energy-and-ai.

[4] Valérie Masson-Delmotte, Panmao Zhai, and Hans-Otto Pörtner. Pörtner. *Global Warming of 1.5° C. An IPCC Special Report on the impacts of global warming of 1.5° C above pre-industrial levels and related global greenhouse gas emission pathways, in the context of strengthening the global response to the threat of climate change, sustainable development, and efforts to eradicate poverty*. ipcc Geneva, 2018. URL: https://www.ipcc.ch/sr15/download/#full.

[5] bp. *Energy Outlook: 2024 edition*. Accessed: 2025-06-02. 2024. URL: https://www.bp.com/en/global/corporate/energy-economics/energy-outlook.html.

[6] Siavash Asiaban, Nezmin Kayedpour, Arash E Samani, Dimitar Bozalakov, Jeroen DM De Kooning, Guillaume Crevecoeur, and Lieven Vandevelde. "Wind and solar intermittency and the associated integration challenges: A comprehensive review including the status in the Belgian power system". In: *Energies* 14.9 (2021), p. 2630.

[7] IEA. *Renewable Energy Market Update - June 2023*. Tech. rep. Licence: CC BY 4.0. Paris: IEA, 2023. URL: https://www.iea.org/reports/renewable-energy-market-update-june-2023.

[8] Aqsa Naeem and Naveed Ul Hassan. "Renewable Energy Intermittency Mitigation in Microgrids: State-of-the-Art and Future Prospects". In: *2020 4th International Conference on Green Energy and Applications (ICGEA)*. 2020, pp. 158–164.

[9] Zac Cesaro, Matthew Ives, Richard Nayak-Luke, Mike Mason, and Ren© Ba±ares-Alc°ntara. "Ammonia to power: Forecasting the levelized cost of electricity from green ammonia in large-scale power plants". In: *Applied Energy* 282 (2021), p. 116009. URL: https://www.sciencedirect.com/science/article/pii/S0306261920314549.

[10] Shafiqur Rehman, Luai M Al-Hadhrami, and Md Mahbub Alam. "Pumped hydro energy storage system: A technological review". In: *Renewable and Sustainable Energy Reviews* 44 (2015), pp. 586–598.

[11] Dominik Born, Peter Stein, Gabriel Marinescu, Stefan Koch, and Daniel Schumacher. "Thermal modeling of an intermediate pressure steam turbine by means of conjugate heat transfer—simulation and validation". In: *Journal of Engineering for Gas Turbines and Power* 139.3 (2017), p. 031903.

[12] Heinz P. Bloch. *A Practical Guide to Steam Turbine Technology*. Upper Saddle River, NJ: Prentice Hall, 1996.

[13] Mark Baker and Budimir Rosic. *TURBINES FOR FLEXIBLE POWER PLANT OPERATION*. Tech. rep. 2022.

[14] Chaudhary Awais Salman, Hailong Li, Peng Li, and Jinyue Yan. "Improve the flexibility provided by combined heat and power plants (CHPs)–a review of potential technologies". In: *e-Prime-Advances in Electrical Engineering, Electronics and Energy* 1 (2021), p. 100023.

[15] Mark Baker and Budimir Rosic. "The Hybrid Pathway to Flexible Power Turbines, Part I: Novel Autoencoder Methods for the Automated Optimization of Thermal Probes and Fast Sparse Data Reconstruction, Enabling Real-Time Thermal Analysis". In: *Journal of Engineering for Gas Turbines and Power* 146.3 (2024), p. 031020.

[16] S. Can Gülen. *Gas Turbines for Electric Power Generation*. Cambridge: Cambridge University Press, 2019.

[17] Oguzhan Murat, Budimir Rosic, Koichi Tanimoto, and Ryo Egami. "Experimental and Numerical Study for Improved Understanding of Mixed-Convection Type of Flows in Turbine Casing Cavities During Shut-Down Regimes". In: *Journal of Engineering for Gas Turbines and Power* 143.12 (Oct. 2021), p. 121009. eprint: https://asmedigitalcollection.asme.org/gasturbinespower/article-pdf/143/12/121009/6766078/gtp_143_12_121009.pdf. URL: https://doi.org/10.1115/1.4052026.

[18] Stanley A Armbruster. "Steam Turbine Generators". In: *Power Plant Engineering*. Springer, 1996, pp. 218–249.

[19] Mariusz Banaszkiewicz. "Steam turbines start-ups". In: *Transactions of the institute of fluid-flow machinery* (2014).

[20] David L. Chandler. "Shining Brightly". In: *MIT News* (Oct. 2011). URL: https://news.mit.edu/2011/energy-scale-part3-1026.

[21] David R Clarke, Matthias Oechsner, and Nitin P Padture. "Thermal-barrier coatings for more efficient gas-turbine engines". In: *MRS bulletin* 37.10 (2012), pp. 891–898.

[22] Yongjian Sun and Bo Xu. "On real-time creep damage prediction for steam turbine". In: *Transactions of the Institute of Measurement and Control* 44.13 (2022), pp. 2603–2610.

[23] Peter Jansohn. "Modern gas turbine systems: High efficiency, low emission, fuel flexible power generation". In: (2013).

[24] Mark Baker and Budimir Rosic. "The Hybrid Pathway to Flexible Power Turbines: Part IV, Automated Construction of Mesh Derived Thermal Network Models for Fast Full-Machine Thermal Analysis". In: *Journal of Engineering for Gas Turbines and Power* 147.10 (Mar. 2025), p. 101006. eprint: https://asmedigitalcollection.asme.org/gasturbinespower/article-pdf/147/10/101006/7447898/gtp_147_10_101006.pdf. URL: https://doi.org/10.1115/1.4067992.

[25] Ramaswamy Viswanathan. *Damage mechanisms and life assessment of high temperature components*. ASM international, 1989.

[26] Andrew Pilkington, Budimir Rosic, and Shigenari Horie. "Methods for Controlling Gas Turbine Casing Flows During Engine Shutdown". In: *International Journal of Turbomachinery, Propulsion and Power* 3.2 (2018). URL: https://www.mdpi.com/2504-186X/3/2/17.

[27] Boris Bangert, Edwin Gobrecht, Norbert Henkel, and Uwe Zander. "Turbine casing". Patent US20010022933A1. 2001. URL: https://patents.google.com/patent/US20010022933A1/en.

[28] Dominik Born, Kurt Heiniger, Giorgio Zanazzi, Thomas Mokulys, Patrick Grossmann, Luca Ripamonti, and Michael Sell. "Validation of conjugate heat transfer predictions on labyrinth seals and novel designs for improved component lifetime". In: *Turbo Expo: Power for Land, Sea, and Air*. Vol. 54679. 2011, pp. 2275–2287.

[29] M Fadl, P Stein, and L He. "Full conjugate heat transfer modelling for steam turbines in transient operations". In: *International Journal of Thermal Sciences* 124 (2018), pp. 240–250.

[30] Andrew Pilkington, Budimir Rosic, Koichi Tanimoto, and Shigenari Horie. "Prediction of natural convection heat transfer in gas turbines". In: *International Journal of Heat and Mass Transfer* 141 (2019), pp. 233–244. URL: https://www.sciencedirect.com/science/article/pii/S0017931019311068.

[31] Gabriel Marinescu, Wolfgang F Mohr, Andreas Ehrsam, Paolo Ruffino, and Michael Sell. "Experimental Investigation Into Thermal Behavior of Steam Turbine Components—Temperature Measurements With Optical Probes and Natural Cooling Analysis". In: *Journal of engineering for gas turbines and power* 136.2 (2014), p. 021602.

[32] Weiliang Wang, Hai Zhang, Pei Liu, Zheng Li, Weidou Ni, Hideyuki Uechi, and Takumi Matsumura. "A finite element method approach to the temperature distribution in the inner casing of a steam turbine in a combined cycle power plant". In: *Applied Thermal Engineering* 105 (2016), pp. 18–27.

[33] Wenhao Huo, Jun Li, and Xin Yan. "Effects of coolant flow rates on cooling performance of the intermediate pressure stages for an ultra-supercritical steam turbine". In: *Applied thermal engineering* 62.2 (2014), pp. 723–731.

[34] Włodzimierz Wróblewski. "Numerical evaluation of the blade cooling for the supercritical steam turbine". In: *Applied Thermal Engineering* 51.1-2 (2013), pp. 953–962.

[35] Chunhua Sheng and Qingluan Xue. "Aerothermal analysis of turbine blades using an unstructured flow solver-U2NCLE". In: *38th AIAA Thermophysics Conference*. 2005, p. 4683.

[36] Jose M Chaquet, Roque Corral, Guillermo Pastor, Jesus Pueblas, and DD Coren. "Validation of a coupled fluid/solid heat transfer method". In: *Turbo Expo: Power for Land, Sea, and Air*. Vol. 54655. 2011, pp. 893–903.

[37] L. He and M. L. G. Oldfield. "Unsteady Conjugate Heat Transfer Modeling". In: *Journal of Turbomachinery* 133.3 (Nov. 2010), p. 031022. eprint: https://asmedigitalcollection.asme.org/turbomachinery/article-pdf/133/3/031022/5612585/031022_1.pdf. URL: https://doi.org/10.1115/1.4001245.

[38] Zhen-Xue Han, Brian H Dennis, and George S Dulikravich. "Simultaneous prediction of external flow-field and temperature in internally cooled 3-D turbine blade material". In: *Turbo Expo: Power for Land, Sea, and Air*. Vol. 78569. American Society of Mechanical Engineers. 2000, V003T01A059.

[39] Vijay K Garg. "Heat transfer research on gas turbine airfoils at NASA GRC". In: *International Journal of Heat and Fluid Flow* 23.2 (2002), pp. 109–136.

[40] William D York and James H Leylek. "Three-dimensional conjugate heat transfer simulation of an internally-cooled gas turbine vane". In: *Turbo Expo: Power for Land, Sea, and Air*. Vol. 36886. 2003, pp. 351–360.

[41] T. Verstraete, Z. Alsalihi, and R. A. Van den Braembussche. "Numerical Study of the Heat Transfer in Micro Gas Turbines". In: *Journal of Turbomachinery* 129.4 (2006), pp. 835–841.

[42] Oguzhan Murat and Budimir Rosic. "A New RANS Based Reynolds Stress and Turbulent Heat Flux Treatment and Challenges in Predictions of Mixed Convection Type of Flows". In: *Turbo Expo: Power for Land, Sea, and Air*. Vol. 87011. American Society of Mechanical Engineers. 2023, V07BT14A016.

[43] Hermann Schlichting and Klaus Gersten. *Boundary-layer theory*. springer, 2016.

[44] Christopher L Rumsey, Thomas B Gatski, and Joseph H Morrison. "Turbulence model predictions of strongly curved flow in a U-duct". In: *AIAA journal* 38.8 (2000), pp. 1394–1402.

[45] Kemal Hanjalić and Brian Launder. *Modelling turbulence in engineering and the environment: second-moment routes to closure*. Cambridge university press, 2011.

[46] Henk Kaarle Versteeg. *An introduction to computational fluid dynamics the finite volume method, 2/E*. Pearson Education India, 2007.

[47] Zixiang Sun, John W. Chew, Nicholas J. Hills, Konstantin N. Volkov, and Christopher J. Barnes. "Efficient Finite Element Analysis/Computational Fluid Dynamics Thermal Coupling for Engineering Applications". In: *Journal of Turbomachinery* 132.3 (2010), p. 031016.

[48] Zhi Wang, Roque Corral, Jose M Chaquet, and Guillermo Pastor. "Analysis and improvement of a loosely coupled fluid-solid heat transfer method". In: *Turbo Expo: Power for Land, Sea, and Air*. Vol. 55157. American Society of Mechanical Engineers. 2013, V03BT11A006.

[49] Jia Ma and Feng Xu. "Transient flows around a fin at different positions". In: *Procedia Engineering* 126 (2015), pp. 393–398.

[50] L He and M Fadl. "Multi-scale time integration for transient conjugate heat transfer". In: *International Journal for Numerical Methods in Fluids* 83.12 (2017), pp. 887–904.

[51] Mark Baker and Budimir Rosic. "The Hybrid Pathway to Flexible Power Turbines, Part II: Fast Data Transfer Methods Between Varying Fidelity Simulations, to Enable Efficient Conjugate Thermal Field Prediction". In: *Journal of Engineering for Gas Turbines and Power* 146.3 (Dec. 2023), p. 031021. eprint: https://asmedigitalcollection.asme.org/gasturbinespower/article-pdf/146/3/031021/7066381/gtp_146_03_031021.pdf. URL: https://doi.org/10.1115/1.4063588.

[52] Magnus Fast and T Palme. "Application of artificial neural networks to the condition monitoring and diagnosis of a combined heat and power plant". In: *Energy* 35.2 (2010), pp. 1114–1120.

[53] Krzysztof Dominiczak, Romuald Rzadkowski, and Wojciech Radulski. "Temperature and stress steam turbine rotor control based on neural network". In: *J. Vib. Eng. Technol.* 4.4 (2016), pp. 319–326.

[54] Jan Greis, Edwin Gobrecht, and Steffen Wendt. "Flexible and economical operation of power plants: 25 years of expertise". In: *Turbo Expo: Power for Land, Sea, and Air*. Vol. 44724. American Society of Mechanical Engineers. 2012, pp. 497–504.

[55] Jing Xin, Rong Yu, Ding Liu, and Youmin Zhang. "Thermal stress deformation prediction for rotary air-preheater rotor using deep learning approach". In: *International Journal of Modelling, Identification and Control* 31.4 (2019), pp. 293–302.

[56] Jianxi Yu, Pei Liu, and Zheng Li. "Hybrid modelling and digital twin development of a steam turbine control stage for online performance monitoring". In: *Renewable and Sustainable Energy Reviews* 133 (2020), p. 110077.

[57] Leonid Moroz, Maksym Burlaka, and Valentyn Barannik. "Application of digital twin for gas turbine off-design performance and operation analyses". In: *AIAA Propulsion and Energy 2019 Forum*. 2019, p. 3913.

[58] Ding Guo, Tianyuan Liu, Di Zhang, and Yonghui Xie. "Fast reconstruction method of the stress field for the steam turbine rotor based on deep fully convolutional network". In: *Journal of Engineering for Gas Turbines and Power* 144.2 (2022), p. 021023.

[59] Rong Xie, Muyan Chen, Weihuang Liu, Hongfei Jian, and Yanjun Shi. "Digital twin technologies for turbomachinery in a life cycle perspective: A review". In: *Sustainability* 13.5 (2021), p. 2495.

[60] Rainer Quinkertz, Thomas Thiemann, and Kai Gierse. "Validation of advanced steam turbine technology: a case study of an ultra super critical steam turbine power plant". In: *Turbo Expo: Power for Land, Sea, and Air*. Vol. 54679. 2011, pp. 2381–2391.

[61] Yevgen Kostenko and David Veltmann. “Development of Hot Standby Mode for Flexible Steam Turbine Operation”. In: *Proceedings of the GPPS Forum 18, Global Power and Propulsion Society*. Zurich, Switzerland. 2018, pp. 1–8.

[62] EIJI Saito, NARIYUKI Matsuno, KEIZO Tanaka, SHIN Nishimoto, RYUICHI Yamamoto, and SHINYA Imano. “Latest technologies and future prospects for a new steam turbine”. In: *Mitsubishi Heavy Industries Technical Review* 52.2 (2015), pp. 39–46.

[63] DR Cornell. “Steam turbine monitoring technology, validation, and verification tests for power plants”. In: *Advances in Steam Turbines for Modern Power Plants*. Elsevier, 2017, pp. 241–260.

[64] K Laxminarayan, HS Jayanth, and M Venkatarama Reddy. “Design and analysis of high-pressure casing of a steam turbine”. In: *Procedia Materials Science* 5 (2014), pp. 1745–1754.

[65] Chelamalasetti Pavan Satyanarayana and YV Hanumantha Rao. “Design and analysis of high-pressure casing of a steam turbine”. In: *International Journal of Mechanical Engineering and Technology* 8.7 (2017), p. 11.

[66] Theodore L Bergman, Adrienne S Lavine, Frank P Incropera, and David P DeWitt. *Introduction to heat transfer*. John Wiley & Sons, 2011.

[67] Farnam Custom Products. *Flow Torch^{TM} 400 Air Heater Brochure*. Revised 8/10/2015, Accessed 30 June 2025. Aug. 2015. URL: https://www.farnam-custom.com.

[68] Ali Chaibakhsh and Ali Ghaffari. “Steam turbine model”. In: *Simulation Modelling Practice and Theory* 16.9 (2008), pp. 1145–1162.

[69] AV Klimenko, OO Milman, and BA Shifrin. “A high-temperature gas-and-steam turbine plant operating on combined fuel”. In: *Thermal Engineering* 62 (2015), pp. 807–816.

[70] Glanville. *ASSESSMENT FOR PROPOSED RIG Osney Lab*. 2018. URL: www.glanvillegroup.com.

[71] Thermosense Ltd. *TW Welded Tip Fast Response Thermocouple Sensor Datasheet*. https://www.thermosense.co.uk. Accessed: 2025-06-30. 2022.

[72] National Instruments Corporation. *NI cDAQ-9188 Specifications*. Document Revision Date: 2023-01-19. Jan. 2023. URL: https://www.ni.com.

[73] Sylvain Brohez, Christian Delvosalle, and Guy Marlair. “A two-thermocouples probe for radiation corrections of measured temperatures in compartment fires”. In: *Fire safety journal* 39.5 (2004), pp. 399–411.

[74] Texas Instruments. *DRV8825 Stepper Motor Controller IC Datasheet*. Revised January 2023, Document Number: SLVSA73F. Texas Instruments Incorporated. Jan. 2023. URL: https://www.ti.com/product/DRV8825.

[75] Maker Store. *CNC Shield Guide v1.1*. Version 1.1. Maker Group Global LLC. Dec. 2022. URL: https://www.makerstore.com.au/product/elec-cnc-shield-v4-pk/.

[76] International Organization for Standardization. *Measurement of Fluid Flow by Means of Pressure Differential Devices Inserted in Circular Cross-Section Conduits Running Full — Part 2: Orifice Plates*. Tech. rep. ISO 5167-2:2003. Geneva, Switzerland: International Organization for Standardization, 2003.

[77] Shi Liu, Hong Yin, Yan Xiong, and Xiaoqing Xiao. "A Comparative Analysis of Single Nozzle and Multiple Nozzles Arrangements for Syngas Combustion in Heavy Duty Gas Turbine". In: *Journal of Energy Resources Technology* 139.2 (Aug. 2016), p. 022004. eprint: https://asmedigitalcollection.asme.org/energyresources/article-pdf/139/2/022004/6149620/jert_139_02_022004.pdf. URL: https://doi.org/10.1115/1.4034232.

[78] Gabriel Marinescu and Andreas Ehrsam. "Experimental investigation into thermal behavior of steam turbine components: part 2—natural cooling of steam turbines and the impact on LCF life". In: *Turbo expo: power for land, sea, and air*. Vol. 44700. American Society of Mechanical Engineers. 2012, pp. 1111–1120.

[79] Yuncheng Xu and Xiaofeng Liu. "An immersed boundary method with y^+ adaptive wall function for smooth wall shear". In: *International Journal for Numerical Methods in Fluids* 93.6 (2021), pp. 1929–1946.

[80] Salim M. Salim and Siew Cheong Cheah. "Wall y^+ strategy for dealing with wall-bounded turbulent flows". In: *Proceedings of the International MultiConference of Engineers and Computer Scientists (IMECS)*. Vol. 2. Newswood Limited. Hong Kong, Mar. 2009, pp. 2165–2170.

[81] M. Fadl, P. Stein, and L. He. "Full conjugate heat transfer modelling for steam turbines in transient operations". In: *International Journal of Thermal Sciences* 124 (2018), pp. 240–250. URL: https://www.sciencedirect.com/science/article/pii/S1290072917315260.

[82] Monika Topel. "Steam Turbine Thermal Modeling for Improved Transient Operation". Licentiate Thesis. Stockholm, Sweden: KTH Royal Institute of Technology, 2014.

[83] Chukwuemeka Godwin Nwangele. *Supplementary Data for ASME Turbo Expo 2025 Paper GT2025-152287*. Accessed: 25 February 2025. 2025. URL: https://github.com/EmekaNwangele/152287_ASME.

[84] Chukwuemeka G. Nwangele, Mark Baker, Koichi Tanimoto, Ryo Egami, and Budimir Rosic. "Enabling Operational Flexibility of Power Generation Systems: Novel Experimental Facility for Characterization of Turbine Casing Thermal Field". In: *Journal of Engineering for Gas Turbines and Power* 148.3 (Oct. 2025), p. 031005. eprint: https://asmedigitalcollection.asme.org/gasturbinespower/article-pdf/148/3/031005/7554049/gtp-25-1380.pdf. URL: https://doi.org/10.1115/1.4069607.

[85] FP Incropera, DP DeWitt, TL Bergman, and AS Lavine. *Fundamentals of Heat and Mass Transfer 6th Edition, Fundamentals of Heat and Mass Transfer*. 2007.

[86] Márta Rencz and Lorenzo Codecasa. *Thermal and Electro-thermal System Simulation*. MDPI, 2019.

[87] Godwin Chukwuemeka Nwangele, Mark Baker, Koichi Tanimoto, Ryo Egami, and Budimir Rosic. "Enabling Flexible Power Generation Systems: Experimental Facility and Novel Numerical Tools for Thermal Field Optimisation". In: *Proceedings of the Global Power and Propulsion Society*. GPPS Shanghai25, September 4–6, 2025. Sept. 2025. URL: https://www.gpps.global.

[88] Mark Baker and Budimir Rosic. "The Hybrid Pathway to Flexible Power Turbines: Part IV, Automated Construction of Mesh Derived Thermal Network Models for Fast Full-Machine Thermal Analysis". In: *Journal of Engineering for Gas Turbines and Power* 147.10 (2025), p. 101006.

[89] Hugo FM Milan and Kifle G Gebremedhin. "Tetrahedral node for Transmission-Line Modeling (TLM) applied to bio-heat transfer". In: *Computers in biology and medicine* 79 (2016), pp. 243–249.

[90] Nico Schlömer. *meshio: Tools for mesh files*. 2019. URL: https://github.com/nschloe/meshio.

[91] E Poursaeidi, Morteza Taheri, and A Farhangi. "Non-uniform temperature distribution of turbine casing and its effect on turbine casing distortion". In: *Applied thermal engineering* 71.1 (2014), pp. 433–444.

[92] Piotr Łuczyński, Dennis Toebben, Manfred Wirsum, Wolfgang FD Mohr, and Klaus Helbig. "Unsteady conjugate heat transfer investigation of a multistage steam turbine in warm-keeping operation with hot air". In: *Journal of Engineering for Gas Turbines and Power* 141.1 (2019), p. 011005.

[93] Dennis Toebben, Adrian Hellmig, Piotr Luczynski, Manfred Wirsum, Wolfgang FD Mohr, and Klaus Helbig. "Analytical Heat Transfer Correlation for a Multistage Steam Turbine in Warm-Keeping Operation With Air". In: *Journal of Engineering for Gas Turbines and Power* 141.1 (2019), p. 011013.

[94] Robert Bergholz. *Advanced Turbine Cooling and Thermal Management*. Tech. rep. NASA/CR-2008-215238. Contract report prepared by GE Aviation for NASA's Propulsion 21 program. NASA Glenn Research Center, June 2008. URL: https://ntrs.nasa.gov/citations/20080025993.

[95] H. S. Carslaw and J. C. Jaeger. *Conduction of Heat in Solids*. 2nd ed. Oxford University Press, 1959.

[96] ANSYS, Inc. *PyFluent Documentation (version 0.34.2)*. https://fluent.docs.pyansys.com/. Accessed: 2025-08-30. 2025.

[97] BayesianOptimization Contributors. *BayesianOptimization Documentation, version 3.1.0*. https://bayesian-optimization.github.io/BayesianOptimization/3.1.0/. Accessed: 2025-08-30. 2025.

[98] Peter I Frazier. "A tutorial on Bayesian optimization". In: *arXiv preprint arXiv:1807.02811* (2018).

[99] Andrzej Rusin, Grzegorz Nowak, Henryk Łukowicz, Wojciech Kosman, Tadeusz Chmielniak, and Maciej Kaczorowski. "Selecting optimal conditions for the turbine warm and hot start-up". In: *Energy* 214 (2021), p. 118836.

[100] Hengliang Zhang, Danmei Xie, Yanzhi Yu, and Liangying Yu. "Online optimal control schemes of inlet steam temperature during startup of steam turbines considering low cycle fatigue". In: *Energy* 117 (2016), pp. 105–115.

[101] Ji Dong-mei, Sun Jia-qi, Sun Quan, Guo Heng-Chao, Ren Jian-Xing, and Zhu Quan-jun. "Optimization of start-up scheduling and life assessment for a steam turbine". In: *Energy* 160 (2018), pp. 19–32.

[102] Dong-Mei Ji, Jia-Qi Sun, Yue Dui, and Jian-Xing Ren. "The optimization of the start-up scheduling for a 320 MW steam turbine". In: *Energy* 125 (2017), pp. 345–355.

[103] Grzegorz Nowak, Andrzej Rusin, Henryk Łukowicz, and Martyna Tomala. "Improving the power unit operation flexibility by the turbine start-up optimization". In: *Energy* 198 (2020), p. 117303.

[104] Tadeusz Chmielniak, Grzegorz Nowak, Henryk Łukowicz, and Andrzej Rusin. "Analysis of thermal and stress states in transient operation of a turbine co-operating with twinboiler". In: *Heat Transfer Engineering* 39.13-14 (2018), pp. 1251–1259.

[105] T Perl, A Bräuer, Wolfgang Weyland, and Ulrich Braun. "Application of heat flux transducers to determine perioperative heat exchange". In: *Thermochimica Acta* 422.1-2 (2004), pp. 35–40.

[106] PRN Childs, JR Greenwood, and CA Long. "Heat flux measurement techniques". In: *Proceedings of the Institution of Mechanical Engineers, Part C: Journal of Mechanical Engineering Science* 213.7 (1999), pp. 655–677.

[107] Li-Wen Wu and Yue-Tzu Yang. "Application of the inverse method to the estimation of heat flux and temperature on the external surface in laminar pipe flow". In: *Applied thermal engineering* 26.14-15 (2006), pp. 1714–1724.

[108] Raza Gulfam, Wei Zhu, Li Xu, Izzat Iqbal Cheema, Peng Sheng, Guangyao Zhao, and Yuan Deng. "Design, fabrication and numerical analysis of compact thermal management system integrated with composite phase change material and thermal bridge". In: *Energy Conversion and Management* 156 (2018), pp. 25–33.

[109] Aref Mazloum, Jaroslav Kováčik, Štefan Emmer, and Igor Sevostianov. "Copper–graphite composites: thermal expansion, thermal and electrical conductivities, and cross-property connections". In: *Journal of Materials Science* 51.17 (2016), pp. 7977–7990.

[110] André Boden. "Copper graphite composite Materials: A novel way to engineer thermal conductivity and expansion". PhD thesis. 2015.

[111] Xiaoyu Fan, Ying Sun, Leyi Huang, Jiaqiu Xie, Xiaoliang Zeng, Chenhan Liu, Lifa Zhang, and Yunshan Zhao. "Improvement of interfacial thermal resistance between TIMs and copper for better thermal management". In: *Surfaces and Interfaces* 46 (2024), p. 103905.

[112] BL Theraja. *Fundamentals of Electrical Engineering and Electronics*. S. Chand Publishing, 2006.

[113] RE Collin. "Limitations of the Thevenin and Norton equivalent circuits for a receiving antenna". In: *IEEE Antennas and Propagation Magazine* 45.2 (2003), pp. 119–124.

[114] Shaimerden Kuanganov. “Future Flexible Operation of Power Generation Systems”. St Peter’s College, Trinity Term 2023. MEng Thesis. University of Oxford, Department of Engineering Science, 2023.

[115] NASA. *The Balance of Power in the Earth–Sun System: The Importance of Understanding Clouds*. Tech. rep. FS-2005-9-074-GSFC. “NASA Facts” trifold fact sheet. Washington, DC: National Aeronautics and Space Administration, 2005. URL: https://www.nasa.gov/wp-content/uploads/2015/03/135642main_balance_trifold21.pdf.

[116] Hannah Ritchie, Pablo Rosado, and Max Roser. “Energy Production and Consumption”. In: *Our World in Data* (2020). https://ourworldindata.org/energy-production-consumption.